

Review

The Sensitivity of Tau Tracers for the Discrimination of Alzheimer's Disease Patients and Healthy Controls by PET

Zohreh Mohammadi ^{1,2}, Hadi Alizadeh ¹, János Marton ³ and Paul Cumming ^{4,5,*}¹ Immunology Research Center, Tabriz University of Medical Sciences, Tabriz 5166/15731, Iran² Student Research Committee, Tabriz University of Medical Sciences, Tabriz 5166/15731, Iran³ ABX Advanced Biochemical Compounds Biomedizinische Forschungsreagenzien GmbH, Heinrich-Glaeser-Straße 10-14, D-01454 Radeberg, Germany⁴ Department of Nuclear Medicine, Bern University Hospital, Freiburgstraße 18, CH-3010 Bern, Switzerland⁵ School of Psychology and Counselling, Queensland University of Technology, Brisbane, QLD 4059, Australia

* Correspondence: paul.cumming@insel.ch; Tel.: +41-31-664-04-98

Abstract: Hyperphosphorylated tau aggregates, also known as neurofibrillary tangles, are a hallmark neuropathological feature of Alzheimer's disease (AD). Molecular imaging of tau by positron emission tomography (PET) began with the development of [¹⁸F]FDDNP, an amyloid β tracer with off-target binding to tau, which obtained regional specificity through the differing distributions of amyloid β and tau in AD brains. A concerted search for more selective and affine tau PET tracers yielded compounds belonging to at least eight structural categories; ¹⁸F-flortaucipir, known variously as [¹⁸F]-T807, AV-1451, and Tauvid[®], emerged as the first tau tracer approved by the American Food and Drug Administration. The various tau tracers differ concerning their selectivity over amyloid β , off-target binding at sites such as monoamine oxidase and neuromelanin, and degree of uptake in white matter. While there have been many reviews of molecular imaging of tau in AD and other conditions, there has been no systematic comparison of the fitness of the various tracers for discriminating between AD patient and healthy control (HC) groups. In this narrative review, we endeavored to compare the binding properties of the various tau tracers in vitro and the effect size (Cohen's d) for the contrast by PET between AD patients and age-matched HC groups. The available tracers all gave good discrimination, with Cohen's d generally in the range of two–three in culprit brain regions. Overall, Cohen's d was higher for AD patient groups with more severe illness. Second-generation tracers, while superior concerning off-target binding, do not have conspicuously higher sensitivity for the discrimination of AD and HC groups. We suppose that available pharmacophores may have converged on a maximal affinity for tau fibrils, which may limit the specific signal imparted in PET studies.

Keywords: Alzheimer's disease; tau neurofibrillary tangles (NFTs); positron emission tomography



Citation: Mohammadi, Z.; Alizadeh, H.; Marton, J.; Cumming, P. The Sensitivity of Tau Tracers for the Discrimination of Alzheimer's Disease Patients and Healthy Controls by PET. *Biomolecules* **2023**, *13*, 290. <https://doi.org/10.3390/biom13020290>

Academic Editors: Anne M. Landau, Francisco R. Lopez-Picon and Nadja Van Camp

Received: 10 November 2022

Revised: 12 January 2023

Accepted: 25 January 2023

Published: 3 February 2023



Copyright: © 2023 by the authors. Licensee MDPI, Basel, Switzerland. This article is an open access article distributed under the terms and conditions of the Creative Commons Attribution (CC BY) license (<https://creativecommons.org/licenses/by/4.0/>).

1. Introduction

By definition, tauopathy refers to a group of brain disorders in which intracellular deposition of misfolded hyperphosphorylated tau filaments is a predominant histopathological feature [1]. Tauopathies can arise in various contexts, including traumatic brain injury, and a number of spontaneous neurodegenerative disorders. The ratio of aggregated tau isoforms defines three main groups of tauopathies: 4R (including progressive supranuclear palsy (PSP), corticobasal degeneration (CBD), and argyrophilic grain disease), 3R (Pick's disease), and 3R+4R tauopathies (AD, Down's syndrome, chronic traumatic encephalopathy) [2–4]. In theory, isoform-selective tau ligands for molecular brain imaging by positron emission tomography (PET) might differentiate between these tauopathies. In practice, the regioselectivity of tau-PET findings serves to identify the presence of AD-typical tau deposition. In this narrative review, we focus on the application of tau-PET for identification of pathology in patients with Alzheimer's dementia (AD), with the particular

objective of summarizing the fitness and sensitivity of available tau tracers for the detection of AD pathology.

The accumulations of tau and A β in and around cortical neurons are key features of AD pathology [5]. Tau deposits in AD consist of NFTs, neuropil threads, and neurites in senile plaques, which accumulate in neuronal bodies, dendrites, and axons, respectively [6]. NFTs are ultrastructurally composed of paired helical filaments (PHFs) and lesser amounts of straight filaments (SFs) consisting of all six isoforms of tau protein [7–9]. Although the immunoreactivities of tau aggregates are similar in various tauopathies, the isoform types have histopathological and ultrastructural differences [10]. Progression of cortical tau pathology in AD brains occurs following Braak staging, traditionally assessed by post mortem examination [11]. In Braak stages I and II, tauopathy is confined to the transentorhinal area and hippocampus, extending in stages III and IV to involve the frontal, parietal, and temporal cortex, and in stages V and VI to the entire neocortex, including motor and sensory core fields. Aggregation of NFTs and consequent perturbation of axonal microtubule structure may precede the initiation of cognitive decline in AD patients [12,13]. Indeed, while early A β deposition can accompany normal senescence [14], NFT aggregation does not occur in cognitively healthy people. NFT deposition, which proceeds according to Braak staging, correlates clearly with the degree of neuropathy in AD patients [15–19], also in contrast to the case for A β [15], making tau a rational target for molecular brain imaging of AD.

A new era of PET began with the discovery that the amyloid- β (A β) ligand 2-(1-(6-[(2-[18 F]fluoroethyl) (methyl)amino]-2-naphthyl)ethylidene)malononitrile (18 F]FDDNP (Figure 1a)) presented off-target binding to tau aggregates in the brains of patients with AD [20]. The target selectivity of [18 F]FDDNP PET is imparted by the differing distributions of A β and the tau protein aggregates known as neurofibrillary tangles (NFTs) in AD and certain other tauopathies. Early results in AD with the breakthrough tracer [18 F]FDDNP (Figure 1a) inspired a very broad search for tracers with superior selectivity and sensitivity for diagnosis and monitoring of AD pathology. Subsequent years have seen the development of diverse tau-tracers belonging to various structural classes [21], and there are numerous reviews of the prospects for diagnostic tau PET imaging [22–24]. Indeed, [18 F]-flortaucipir, known variously as [18 F]-T807, AV-451, and TauvidTM, has obtained FDA approval for diagnostic use [25].

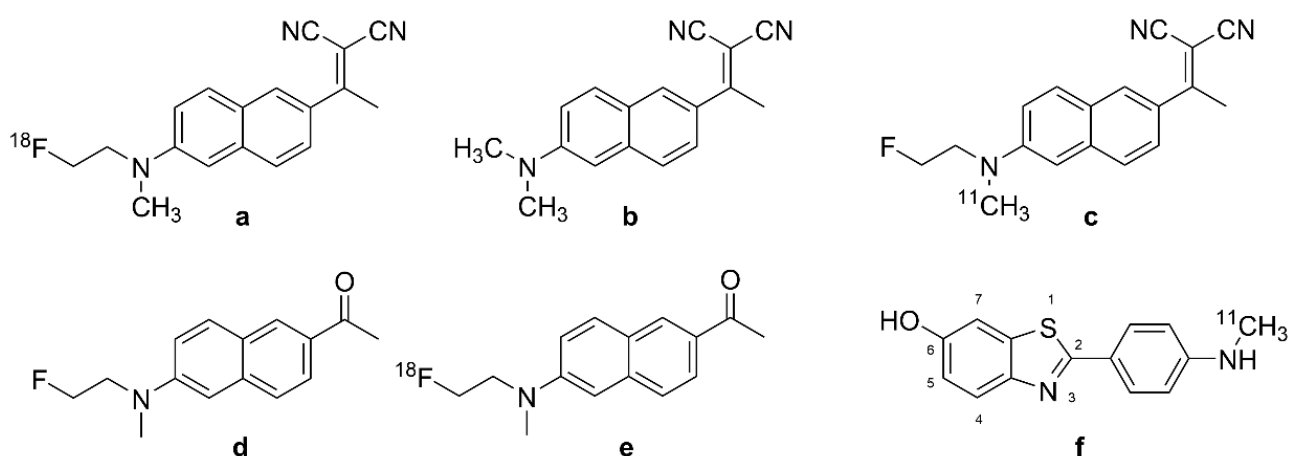


Figure 1. Chemical structure of DDNP analogues and [*N*-methyl- 11 C]-6-OH-BTA-1. (a): [18 F]FDDNP, (b): DDNP, (c): [11 C]FDDNP, (d): FENE, (e): [18 F]FENE, (f): [11 C]PIB.

Meanwhile, there has been a proliferation of tau PET tracers with roughly similar binding properties and sensitivity for the detection of tau pathologies, with little agreement as to the optimal agent for the specific task of AD diagnosis and progression monitoring. This circumstance resembles the surfeit of molecular imaging tracers for the neuroinflammation marker TSPO, many of which have similar binding properties [26].

Herein, we summarize the binding properties of the various tau PET ligands, proceeding from [¹⁸F]-FDDNP (Figure 1a) to the tracers of other structural classes that have been tested in AD patients. For this purpose, we compiled the available data about the affinity and specificity of the various ligands for tau aggregates in vitro, placing emphasis on the off-target binding of certain classes of tau tracers. As an objective measure of effect size in PET studies, we report Cohen's *d* for the contrast between tracer binding in groups of healthy controls (HCs) and AD patients. We intend thereby to establish a rational basis for selecting among the diverse structural classes of tau tracers available at the time of writing.

Molecular Description of Tau Aggregates

Tau is a naturally unfolded tubulin-binding phospho-protein that promotes the assembly of microtubules and their stabilization [27]. The preponderance of tau expression in the central nervous system (CNS) is in neuronal axons, glia, extracellular space [28,29], and dendrites [30]. Tau is encoded by the microtubule-associated protein tau (MAPT) gene located on human chromosome 17q21, which primarily contains 16 exons [31,32]. Six isoforms of human tau protein, ranging in length from 352 to 441 amino acids, arise through alternative mRNA splicing [33,34], resulting in forms with three or four tandem repeats, generally designated as 3R and 4R [33,35].

3R and 4R isoforms have approximately similar concentrations in the healthy human brain [36,37], but tauopathies can entail a disturbed balance of 3R and 4R tau expression, which may arise from the dysregulation of exon 10 splicing [38]. In vitro, tau binds to microtubules with an affinity (K_D) in the range of 75–450 nM [39]. However, the additional repeat domain of 4R tau imparts a considerably higher affinity for microtubules in comparison with 3R tau, such that the 4R form has a more prominent role in microtubule assembly [37,39].

A normal tau protein molecule is naturally unfolded and has a low degree of secondary structure [28,40]. Similar to A β aggregates, tau filaments contain cross β -sheet structures, with cores consisting of approximately 90 amino acids [41]. The formation of pathological aggregates of tau protein is linked to hyperphosphorylation; in this condition, tau loses its affinity for microtubules and instead forms aggregates known as NFTs [42,43]. Of some 85 Ser/Thr/Tyr residues in the longest CNS tau isoform, nearly half can be phosphorylated [44,45], such that tau NFTs cannot be considered as a singular molecular entity. This phenomenon has doubtlessly complicated the search for an optimal PET tracer for the detection of tau aggregates.

2. Development of Tau Tracers for PET

PET employs tracer molecules usually labelled with the short-lived radionuclides [¹¹C] ($t_{1/2}$ = 20.4 min) and [¹⁸F] ($t_{1/2}$ = 109.8 min). An ideal brain radiotracer for tau should fulfill various criteria [46,47]: 1. ability to cross the blood–brain barrier (BBB) and cell membranes; 2. high affinity and selectivity for the target molecule, with low off-target binding, i.e., in the present context >10-fold selectivity for tau over A β and low nonspecific binding; 3. lipophilicity within the narrow range of LogP 2.0–3.5; 4. lack of radiolabeled metabolites that can enter the brain; 5. suitable pharmacokinetics/dynamics for rapid PET imaging. We begin this account with a detailed description of the first tau tracer [¹⁸F]FDDNP (Figure 1a), which was originally described as an A β ligand; this history highlights the difficulty presented by the relatively non-selective interaction of ligands with β -sheets, which are present in various biomolecules.

2.1. [^{18}F]FDDNP, the Accidental First Tau PET Tracer

Development of the first tau tracer began with a fluorescent dye, 1,1-dicyano-2-[6-(dimethylamino)naphthalen-2-yl]propene (DDNP, Figure 1b), originally synthesized for use with fluorescence spectroscopy. DDNP (Figure 1b) possesses an electron donor part (pi-conjugation of a dialkylamino group) and an electron acceptor part (2-cyano acrylate unit) that together impart inherent fluorescence properties. DNNP (Figure 1b) can visualize plaques and tangles through confocal fluorescence microscopy, which encourages the preparation of its fluorinated version, [^{18}F]FDDNP (2-(1-(6-[(2- ^{18}F]fluoroethyl)(methyl)amino]-2-naphthyl)ethylidene)malononitrile, Figure 1a) [48]. FDDNP is more lipophilic than DNNP (Figure 1b), which might impart relatively higher nonspecific binding, i.e., in white matter [49,50]. The physical properties of DDNP (Figure 1b) led researchers to investigate its binding of fibrillar, insoluble protein aggregates with β -sheet conformations such as A β and tau. The binding of the 6-dialkylamino naphthalenyl-2-cyanoacrylate scaffold of DDNP (Figure 1b) to tau-derived binding sequences has been investigated using X-ray microcrystallography [51]. The partially apolar binding cavity in the VQIVYK sequence (a hexapeptide motif responsible for tau aggregation) of tau protein has a tube-like shape formed between a pair of β -sheets, which may favor the binding of DNNP (Figure 1b) and other uncharged molecules such as benzodiazepines and anesthetics.

2.1.1. In Vitro Studies

The first binding studies with DDNP/FDDNP were undertaken using confocal fluorescence microscopy of brain specimens in vitro [20,52]. Initial results suggested the presence of two kinetically distinguishable binding sites at A β fibrils in vitro, with K_{D} s of 0.12 nM and 1.86 nM for FDDNP, and somewhat lesser corresponding affinities for its analog, FENE (Figure 1d, 1-(6-[(2-fluoroethyl)(methyl)amino]naphthalen-2-yl)ethenone). In addition, FENE (Figure 1d) had a high-capacity, low-affinity binding site, which tended to obscure the high-affinity site. These results led to the selection of FDDNP for further research as an A β tracer. However, autoradiography with [^{18}F]FDDNP (Figure 1a) and [^{18}F]FENE (Figure 1e, 1-(6-[(2- ^{18}F]fluoroethyl)(methyl)amino]naphthalen-2-yl) ethanone) showed binding to tau in AD cortical specimens.

Due to epidemiological findings that non-steroidal anti-inflammatories (NSAIDs) may reduce the risk of AD, researchers [50] tested the interaction between NSAIDs and [^{18}F]FDDNP (Figure 1a) at A β fibrils from AD brain specimens. There was some displacement by NSAIDs, but not by Congo-red and thioflavin T, which raised a flag about the specificity of [^{18}F]FDDNP (Figure 1a) for NFT versus A β . [^{18}F]FDDNP (Figure 1a) showed binding to A β 42 ($K_{\text{D}} = 5.5$ nM and $B_{\text{max}} = 0.28$ pmol/nmol) and also to K18 Δ K280 tau fibrils ($K_{\text{D}} = 37$ nM and $B_{\text{max}} = 2.1$ pmol/nmol) [53]. With the $B_{\text{max}}/K_{\text{D}}$ ratios being roughly similar for the two targets, these findings in vitro might predict ambivalence of [^{18}F]FDDNP (Figure 1a) binding in living brains. Nonetheless, Harada et al. showed higher bind affinity of [^{18}F]FDDNP (Figure 1a) for A β fibrils than for tau fibrils, as likewise seen for [^3H]PiB [53]. In 2006, Smid et al. reported on FDDNP labeling in fixed, paraffin-embedded brain tissue sections from patients dying from AD and various other neurodegenerative diseases [54]. Their results indicated that FDDNP preferentially labels structures with A β -like histochemical properties. Since A β , tau, α -synuclein, and prion fibrils all contain similar β -sheet structures, FDDNP labeling potentially indicates a broad-spectrum of pathologies in vitro, but with preferential binding to tau in AD brains. Others have reported lower sensitivity of FDDNP for A β -containing structures when applied at the tracer concentrations typical of PET applications [55]. In 2009, Thompson et al. compared the binding of [^3H]FDDNP in brain sections from AD patients to that of the specific A β ligands [^3H]PiB and [^{14}C]SB13 [56]. There was only weak [^3H]FDDNP labeling in neocortical tissue sections that contained extensive amyloid plaques and cerebrovascular amyloid angiopathy, which were readily labeled with the A β ligands. The authors attributed this to the low affinity of [^3H]FDDNP for A β in AD brain sections. Another study [57] comparing

the binding of [^{18}F]FDDNP (Figure 1a) and [^3H]FDDNP to tau and A β in vitro suggested that the extreme metabolic instability of [^3H]FDDNP may have compromised the study by Thompson et al. [56].

Molecular simulations predicted an interaction between FDDNP and monoamine oxidase B (MAO-B). The moderate binding affinity of FDDNP to MAO-B in silico ($K_i = 99$ nM) closely matched that of safinamide (a known MAO-B inhibitor) to the same target ($K_i = 86$ nM) [58]. It remains unknown if MAO-B binding contributes to the [^{18}F]FDDNP (Figure 1a) PET signal in living brains, but, as shall be seen, it is certain that other tau tracers do present significant off-target binding to MAO-A or B.

2.1.2. In Vivo PET Studies of [^{18}F]FDDNP in AD

[^{18}F]FDDNP (Figure 1a) was the first PET tracer to detect tau pathology in the brain of living AD patients [52], showing increased cortical binding in the lateral and medial temporal lobes in AD patients [20]. Based on the preclinical findings described above, the researchers attributed the PET signal to the composite of NFTs and amyloid plaques. Their PET quantitation relative to the pons reference region (SUVR) showed the highest specific binding in the patients' hippocampus, amygdala, and entorhinal cortex, namely the regions with NFT deposition in AD [11]. The high binding regions matched with brain regions showing hypometabolism measured with [^{18}F]FDG-PET, and brain atrophy measured with MRI. A large-scale study tested the fitness of [^{18}F]FDDNP (Figure 1a) versus [^{18}F]FDG-PET for discriminating healthy elderly, MCA, and AD groups [59]. Results indicated superior group discrimination with [^{18}F]FDDNP (Figure 1a) PET compared with structural MRI or FDG-PET. Among three studies (Table 1), the highest Cohen's d (3.53) was calculated for lateral temporal cortex in the contrast between healthy controls and AD patients with advanced disease (mean MMSE score = 13), with lesser effect sizes in the studies with less severely afflicted patient groups.

Table 1. Comparison between discrimination abilities of tau PET tracers between AD cases and controls in up to three brain regions with highest Cohen’s d values, including as defined by Braak staging system. HC = cognitively healthy elderly controls; AD = Alzheimer’s disease patients; LOAD = late-onset AD; MCI = mild cognitive impairment; MAD = moderate AD; MMSE = mini-mental state examination; SUVr = standard uptake value scaled to the reference tissue; SUVP = standard uptake value scaling with peak alignment; EBM = event-based modeling of sequence of AD pathology.

Tracers	Author (Reference)	Reference Region	n	MMSE ± SD		SUVr of HC	SUVr of AD	Cohen’s d	SUVr of HC	SUVr of AD	Cohen’s d	SUVr of HC	SUVr of AD	Cohen’s d
				HC	AD									
¹⁸ F]FDDNP	Tauber et al., 2013 [60]	Cerebellum	HC = 8 AD = 7	29.0 ± 1.2	22.1 ± 2.5	Frontal cortex			Occipital cortex			Medial temporal cortex		
	Tolboom et al., 2009 [61]	Cerebellar gray matter	HC = 13 AD = 14	29 ± 1	23 ± 3	Frontal cortex			Temporal cortex			Parietal cortex		
	Shin et al., 2008 [62]	Cerebellum	HC = 10 AD = 10	28.4 ± 0.9	13 ± 5	Lateral temporal cortex			Neocortex			Posterior cingulate		
¹⁸ F]THK523	Villemagne et al., 2014 [47]	Cerebellar cortex	HC = 10 AD = 10	29.3 ± 1.1	16.7 ± 6.6	Neocortex			Inferior temporal cortex			Insula		
¹⁸ F]THK5105	Okamura et al., 2014 [63]	Cerebellar cortex	HC = 8 AD = 8	28.8 ± 1.5	17.3 ± 6.6	Inferior temporal cortex			Superior temporal cortex			Neocortex		
¹⁸ F]THK5117	Harada et al., 2015 [64]	Cerebellar cortex	HC = 5 AD = 5	28.7 ± 1.6	18.5 ± 4.6	Neocortex			Posterior cingulate			Inferior temporal cortex		
¹⁸ F]THK5317	Fu et al., 2020 [65]	Cerebellum	HC = 6 AD = 5	28.8 ± 0.7	17.2 ± 6.0	Occipital cortex			Lateral temporal cortex			Parietal cortex		
¹⁸ F]THK5351	Chanisa et al., 2021 [66]	Cerebellum	Age ≤ 60 HC = 13 AD = 6	N/A	N/A	Inferior temporal cortex			Occipital cortex			Posterior cingulate		
			Age > 60 HC = 11 AD = 9	N/A	N/A	Occipital cortex			Precuneus			Inferior temporal cortex		
	Ezura et al., 2021 [67]	Cerebellar cortex	HC = 9 AD = 10	28.8 ± 1.5	18.9 ± 4.6	Inferior temporal gyrus			Fusiform gyrus			Parahippocampus		
	Chen et al., 2018 [68]	SUVP	HC = 9 AD = 9	29	20	Temporal cortex			Occipital cortex			Parietal cortex		
Kang et al., 2017 [69]	Cerebellar gray matter	HC = 43 AD = 51	28.5 ± 1.6	13.8 ± 6.0	Frontal cortex			Medial temporal cortex			Hippocampus			

Table 1. Cont.

Tracers	Author (Reference)	Reference Region	n	MMSE ± SD		SUVr of HC	SUVr of AD	Cohen's d	SUVr of HC	SUVr of AD	Cohen's d	SUVr of HC	SUVr of AD	Cohen's d
				HC	AD									
¹⁸ F]Flortaucipir	Leuzy et al., 2021 [70]	Inferior cerebellar cortex	HC = 638 AD = 159	28.9 ± 1.2	20.4 ± 5.0	Entorhinal cortex		2.48	Early tau ROIs		Temporal meta-ROI			
						1.14 ± 0.12	1.74 ± 0.32		1.19 ± 0.11	1.88 ± 0.46	2.06	1.18 ± 0.11	1.88 ± 0.47	2.05
	Li et al., 2021 [71]	Cerebellar gray matter	HC = 10 AD = 4	29.2 ± 1.3	8.5 ± 6.6	Frontal regions		7.51	Lateral temporal region		Parietal region			
						1.32 ± 0.13	2.26 ± 0.12		1.35 ± 0.14	2.22 ± 0.29	3.82	1.38 ± 0.17	2.59 ± 0.43	3.70
	Wolters et al., 2020 [72]	Cerebellar gray matter	HC = 25 AD/MCI = 53	28 ± 1	23 ± 4	Entorhinal cortex		2.00	Limbic region		Neocortex			
						1.1 ± 0.2	1.5 ± 0.2		1.2 ± 0.1	1.5 ± 0.2	1.89	1.0 ± 0.1	1.4 ± 0.3	1.87
	Chen et al., 2018 [68]	SUVP	HC = 20 AD = 12	29	21	Temporal cortex		0.84	Occipital cortex		Frontal cortex			
					1.18 ± 0.16	1.41 ± 0.35	1.09 ± 0.09		1.17 ± 0.13	0.71	1.06 ± 0.07	1.18 ± 0.23	0.70	
Ossenkuppele et al., 2018 [73]	Cerebellar gray matter	HC = 254 AD = 179	23.6 ± 6.0	20.2 ± 5.5	Entorhinal cortex		2.10	Inferior temporal cortex		Temporoparietal cortex				
					1.73 ± 0.31	1.18 ± 0.2		2.09 ± 0.56	1.23 ± 0.21	2.03	1.89 ± 0.53	1.15 ± 0.18	1.86	
Pontecorvo et al., 2017 [74]	Cerebellar gray matter	Aβ + OC = 58 Aβ + AD = 48	29.5 ± 0.5	22.1 ± 3.7	Fusiform gyrus		2.28	Anterior parahippocampal gyrus		Temporal cortex				
					1.15 ± 0.10	1.66 ± 0.30		1.07 ± 0.13	1.49 ± 0.24	2.17	1.11 ± 0.09	1.64 ± 0.40	1.82	
Cho et al., 2016 [75]	Cerebellar cortex	HC = 20 AD = 20	27.5 ± 2.1	16.9 ± 6.6	Entorhinal cortex		2.26	Parahippocampal cortex		Inferior temporal cortex				
					1.22 ± 0.16	1.80 ± 0.33		1.20 ± 0.17	1.49 ± 0.25	1.99	1.71 ± 0.34	1.22 ± 0.19	1.79	
¹¹ C]PBB3	Kitamura et al., 2018 [76]	Cerebellar gray matter	HC = 9 AD = 17	29.4 ± 0.7	21.4 ± 6.5	Occipital cortex		2.70	Parietal cortex		Lateral temporal cortex			
						0.90 ± 0.03	1.10 ± 0.1		0.83 ± 0.05	1.03 ± 0.1	2.52	0.95 ± 0.04	1.12 ± 0.11	2.05
	Shimada et al., 2017 [77]	Cerebellar cortex	HC = 18 AD = 17	28.9 ± 1.2	16.1 ± 5.1	Mean cortical		2.91						
						0.91 ± 0.06	1.10 ± 0.07							
¹⁸ F]PM-PBB3	Hsu et al., 2020 [78]	Cerebellar gray matter	HC = 12 AD = 10	29.3 ± 0.9	12.5 ± 8.9	Parahippocampus		2.20	Temporal region		Posterior cingulate gyrus			
						0.97 ± 0.11	2.06 ± 0.69		0.99 ± 0.10	2.46 ± 0.95	2.17	1.02 ± 0.09	2.63 ± 1.09	2.08
	Lu et al., 2020 [79]	Cerebellar cortex	HC = 11 AD = 19	N/A	17.0 ± 7.6	Temporal lobe		2.06	Frontal lobe		Occipital lobe			
						0.91 ± 0.06	1.64 ± 0.50		0.85 ± 0.06	1.43 ± 0.42	1.92	0.95 ± 0.06	1.58 ± 0.47	1.91
¹⁸ F]MK6240	Therriault et al., 2022 [80]	Inferior cerebellar cortex	HC = 179 AD = 65	29.1 ± 1.4	19.7 ± 6.2	Temporal meta-ROIs		2.39						
						1.06 ± 0.15	2.82 ± 1.03							
	Ashton et al., 2021 [81]	Inferior cerebellar cortex	HC = 159 AD = 42	29.1 ± 1.1	18.5 ± 5.7	Braak I–II		2.25	Braak III–IV		Braak V–VI			
						0.97 ± 0.2	1.98 ± 0.6		0.95 ± 0.1	2.61 ± 1.1	2.12	0.97 ± 0.1	2.25 ± 2.1	0.86
Leuzy et al., 2021 [70]	Inferior cerebellar cortex	HC = 218 AD = 50	29.2 ± 1.0	18.4 ± 5.9	Early tau ROIs		4.19	Entorhinal cortex		Temporal meta-ROIs				
					0.87 ± 0.12	2.80 ± 0.64		0.93 ± 0.23	2.4 ± 0.56	3.48	0.86 ± 0.11	2.84 ± 0.66	3.42	
Therriault et al., 2021 [82]	Inferior cerebellar cortex	HC = 131 AD = 25	29.1 ± 1.2	20.1 ± 5.7	Braak III–IV		2.95	Braak V–VI		Braak I–II				
					1.04 ± 0.17	2.89 ± 0.87		1.09 ± 0.13	2.47 ± 0.96	2.01	0.99 ± 0.29	2.02 ± 0.86	1.60	

Table 1. Cont.

Tracers	Author (Reference)	Reference Region	n	MMSE ± SD		SUVr of HC	SUVr of AD	Cohen's d	SUVr of HC	SUVr of AD	Cohen's d	SUVr of HC	SUVr of AD	Cohen's d
				HC	AD									
	Therriault et al., 2021 [83]	Inferior cerebellar cortex	HC = 166 AD = 62	29.1 ± 1.0	19.2 ± 6.2	AD signature meta-ROI			Braak I–II					
						1.08 ± 0.24	3.3 ± 1.4	2.21	0.98 ± 0.22	2.04 ± 0.75	1.91			
	Tissot et al., 2021 [84]	Inferior cerebellar cortex	HC = 143 AD = 26	29.0 ± 1.2	19.3 ± 7.1	Braak III–IV			Braak I–II		Braak V–VI			
						1.07 ± 0.12	2.51 ± 0.91	2.21	0.97 ± 0.18	1.63 ± 0.40	2.12	1.10 ± 0.14	2.24 ± 0.87	1.82
	Pascoal et al., 2020 [85]	Inferior cerebellum	HC = 101 LOAD = 21	29.1 ± 1.1	21.2 ± 5.3	Braak II		Braak I			Braak III			
						1.14 ± 0.15	2.6 ± 0.97	2.10	1.13 ± 0.17	3.05 ± 1.32	2.04	1.17 ± 0.1	2.6 ± 1.18	1.93
[¹⁸ F]GTP1	Barthelemy et al., 2022 [86]	Cerebellar gray matter	Aβ + HC = 5 MAD = 10	29.0 ± 0.7	17.6 ± 2.7	Temporal meta-ROIs			Braak III–IV			Braak I–II		
						1.26 ± 0.05	1.67 ± 0.32	1.79	1.2 ± 0.05	1.55 ± 0.35	1.4	1.27 ± 0.04	1.48 ± 0.26	1.12
[¹⁸ F]RO948	Leuzy et al., 2022 [87]	Inferior cerebellar cortex	Aβ – HC = 137 AD = 63	28.9 ± 1.2	19.7 ± 4.2	EBM stage I			EBM stage II		EBM stage III			
						0.97 ± 0.13	1.71 ± 0.36	2.80	1.27 ± 0.11	2.62 ± 0.94	2.01	1.26 ± 0.12	2.37 ± 0.91	1.71
	Leuzy et al., 2021 [70]	Inferior cerebellar cortex	HC = 208 AD = 142	28.7 ± 1.2	20.3 ± 4.1	Entorhinal cortex			Early tau ROIs		Temporal meta-ROIs			
						1.23 ± 0.22	2.00 ± 0.40	3.78	1.23 ± 0.18	2.15 ± 0.66	1.90	1.22 ± 0.18	2.13 ± 0.66	1.88
Leuzy et al., 2020 [88]	Inferior cerebellar cortex	HC = 257 AD = 100	29 ± 1.1	20 ± 4.3	Braak stage V–VI			Entorhinal cortex		Braak stage I–IV				
					1.06 ± 0.10	1.53 ± 0.21	2.85	1.16 ± 0.22	12.02 ± 0.40	2.66	1.17 ± 0.15	2.19 ± 0.58	2.40	
Wong et al., 2018 [89]	Cerebellar cortex	HC = 5 AD = 11	N/A	20.8 ± 2.8	Parahippocampus			Entorhinal area		Anterior temporal lobe				
					0.93 ± 0.2	1.95 ± 0.7	1.98	0.93 ± 0.2	1.91 ± 0.7	1.89	1.01 ± 0.1	1.71 ± 0.6	1.62	
[¹⁸ F]JNJ067	Schmidt et al., 2020 [90]	Ventral cerebellar cortex	HC = 5 AD = 5	28.4 ± 0.5	19.2 ± 5.9	Medial temporal cortex			Amygdala		Occipital cortex			
						1.18 ± 0.09	1.76 ± 0.47	1.71	0.96 ± 0.12	1.51 ± 0.46	1.63	1.14 ± 0.10	1.54 ± 0.40	1.37
[¹⁸ F]PI2620	Bun et al., 2022 [91]	Cerebellum	HC = 7 AD = 7	28.4 ± 1.5	18.7 ± 5.1	Right amygdala		Left amygdala		Left hippocampus				
						1.14 ± 0.08	1.98 ± 0.31	3.63	1.19 ± 0.14	2.07 ± 0.44	2.66	1.42 ± 0.14	1.81 ± 0.21	2.08
	Jantarato et al., 2021 [92]	Cerebellum	HC = 26 AD = 7	27.3	18.4	Occipital cortex			Precuneus		Caudate			
						1.1 ± 0.12	1.14 ± 0.21	0.93	1.02 ± 0.12	1.27 ± 0.45	0.75	0.80 ± 0.13	0.7 ± 0.14	0.74
Mueller et al., 2020 [93]	Cerebellum	HC = 10 AD = 12	29	20.5	Inferior temporal			Fusiform gyrus		Occipital				
					1.08 ± 0.08	1.70 ± 0.32	2.59	1.08 ± 0.09	1.57 ± 0.24	2.55	1.06 ± 0.07	1.39 ± 0.19	2.13	
[¹⁸ F]S16	Fu et al., 2022 [65,94]	Cerebellar gray matter	HC = 6 AD = 5	28.8 ± 0.7	17.2 ± 6.0	Occipital cortex			Lateral temporal cortex		Medial temporal cortex			
						1.10 ± 0.07	1.21 ± 0.08	1.46	1.22 ± 0.09	1.30 ± 0.10	0.84	1.11 ± 0.10	1.18 ± 0.12	0.63
Wang et al., 2021 [95]	Cerebellum	HC = 6 AD = 15	29.8 ± 0.3	18.6 ± 5.3	Parietal cortex			Posterior cingulate and precuneus		Occipital cortex				
					1.10 ± 0.05	1.35 ± 0.19	1.78	1.17 ± 0.04	1.35 ± 0.14	1.70	1.05 ± 0.03	1.19 ± 0.12	1.49	

Shin et al. directly compared the regional binding of the A β -ligand [^{11}C]PIB (Figure 1f) and [^{18}F]FDDNP (Figure 1a) in the same AD subjects [62]. They found sparse [^{11}C]PIB (Figure 1f) binding, but abundant [^{18}F]FDDNP (Figure 1a) binding, in the medial temporal cortex, whereas both tracers had high uptake in many neocortical areas, consistent with the overlapping distributions of the two markers in AD. Cognitively normal elderly subjects in that study also had significant [^{18}F]FDDNP (Figure 1a) binding in the medial temporal cortex, which correlated inversely with memory scores in the California Verbal Learning Test. Another dual tracer PET study [61] tested for correlations between [^{11}C]PIB (Figure 1f) and [^{18}F]FDDNP (Figure 1a) binding and CSF markers, finding that [^{18}F]FDDNP (Figure 1a) binding correlated directly with CSF levels of A β and tau, whereas global [^{11}C]PIB signal (Figure 1f) correlated inversely with the CSF A β level. Thus, [^{18}F]FDDNP (Figure 1a) PET had some degree of specificity toward intracerebral tau in AD. Others called for caution in the interpretation of [^{18}F]FDDNP (Figure 1a) results due to its low specific binding to tau [96]. With this caveat, Tolboom et al. reported higher [^{18}F]FDDNP (Figure 1a) uptake in AD patients than in HCs, but no difference in their MCI group ($n = 11$); global cortical [^{18}F]FDDNP (Figure 1a) uptake in AD patients had considerable overlap with the range of HC values, which they attributed to the high off-target binding. In human subjects without dementia, impaired cognition, old age, and APOE-4 carriage were associated with higher binding of [^{18}F]FDDNP (Figure 1a) in medial and lateral temporal lobes and frontal cortex regions [97]. The partial selectivity of [^{18}F]FDDNP (Figure 1a) for NFTs rather than A β plaques in AD brains was further suggested in a dual tracer [^{18}F]FDDNP (Figure 1a) and [^{11}C]PIB (Figure 1f) PET study comparing frontotemporal dementia and AD patients [98], which suggested that [^{18}F]FDDNP (Figure 1a) retention was more indicative of tauopathy in AD patients. Due to its imperfect target selectivity, [^{18}F]FDDNP (Figure 1a) has largely given way to new PET tracers.

2.2. Arylquinoline and Arylquinoxaline Derivatives

In 2005, arylquinoline derivative tracers 2-[(4- ^{11}C)-methylamino]phenyl]quinoline ([^{11}C]BF-158, *N*-[^{11}C]methyl-4-(quinolin-2-yl)aniline, Figure 2e) and 2-(4-aminophenyl)quinoline (BF-170 (Figure 2b)) were discovered by Okamura et al. [99] through the screening of a chemical compound library of small molecular weight β -sheet binding compounds. Although Okamura et al. did not confirm their fitness for human PET studies, their compounds had excellent brain uptake and rapid clearance in living mice. BF-158 (Figure 2a, *N*-methyl-4-(quinolin-2-yl)aniline) and BF-170 (Figure 2b, 2-(4-aminophenyl)quinoline) had somewhat lower EC₅₀ values for tau fibrils (399 and 221 nM) compared with A β (659 and 786 nM). Hence, BF-158 (Figure 2a) and BF-170 (Figure 2b) displayed higher binding affinity to tau filaments and lower binding affinity to A β fibrils than BF-168 (a styrylbenzoxazole derivative, Figure 2c, (*E*)-4-(2-(6-(2-fluoroethoxy)benzo[d]oxazol-2-yl)vinyloxy)-*N*-methylaniline). The ligands readily visualized NFTs, neuropil threads, and PHF-type neuritis in brain sections, and [^{11}C]BF-158 (Figure 2e) autoradiographically labeled NFTs in AD brain sections. However, in a fluorescence assay, these ligands also labeled A β fibrils, thus indicating incomplete specificity toward tau pathology. Furthermore, the ligands did not bind significantly to PHFs in non-AD pathologies, suggesting that they might serve for the differentiation of AD from non-AD tauopathies by PET.

2.2.1. [^{18}F]THK-523 (BF-242)

Based on preceding results, Fodero-Tavoletti et al. [100] developed [^{18}F]THK-523 (Figure 2f, 2-(4-aminophenyl)-6-(2-[^{18}F]fluoroethoxy)quinoline; [^{18}F]BF-242), the first [^{18}F]-labeled arylquinoline tau tracer, from a structural modification of BF170 (Figure 2b). The addition of the alkyl ether group to position C6 of the arylquinoline rendered the structure more selective to tau aggregates and enabled the incorporation of [^{18}F]. [^{18}F]THK-523 (Figure 2f) along with its congeners [^{18}F]THK-5105 (Figure 3b, 1-((2-(4-dimethylamino)phenyl)quinolin-6-yl)oxy)-3-[^{18}F]fluoropropan-2-ol) and [^{18}F]THK-5117 (Figure 3d, 1-[^{18}F]fluoro-3-[2-[4-(methylamino)phenyl]quinolin-6-yl]oxypropan-2-ol) were chosen to proceed into

clinical studies. [^{18}F]THK-523 (Figure 2f) is of low molecular weight (282.3 g/mol) and has a favorable logP value (2.9 ± 0.1 nM), consistent with high brain uptake.

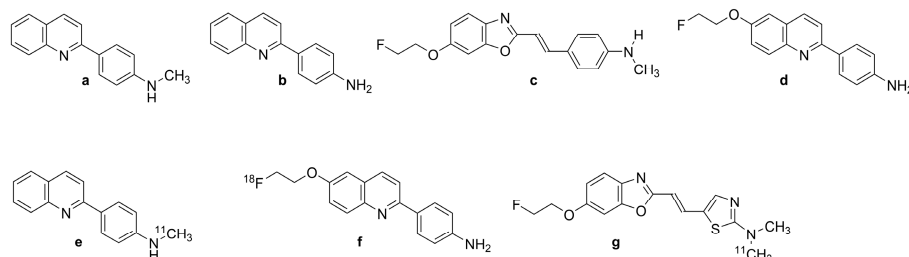


Figure 2. Chemical structure of tau ligands and their labeled derivatives with quinoline and benzoxazole scaffolds. (a): BF-158, (b): BF-170, (c): BF-168, (d): BF-242 or THK-523, (e): [^{11}C]BF-158, (f): [^{18}F]BF-242 or [^{18}F]THK-523, (g): [^{11}C]BF-227.

Initial *in vitro* saturation studies exhibited two classes of binding sites on synthetic heparin-induced tau polymers (HITP) and one class on $\text{A}\beta_{1-42}$ fibrils. [^{18}F]THK-523 (Figure 2f) bound biphasically to synthetic HITP with affinities of 1.7 and 22 nM, but to a single site for $\text{A}\beta_{1-42}$ with 21 nM affinity. Autoradiographic analysis of human hippocampal serial sections of AD brains demonstrated overlap between [^{18}F]THK-523 (Figure 2f) binding and tau immunostaining pattern.

Harada et al. [53] confirmed the higher affinity of [^{18}F]THK-523 (Figure 2f) for tau fibrils than for $\text{A}\beta$ fibrils. *In vitro* autoradiography of brain sections from AD patients exhibited a band-like distribution of [^{18}F]THK-523 (Figure 2f) in the inner layer of the temporal cortex, also matching the distribution of tau, but not $\text{A}\beta$ -immunostaining or [^{11}C]PiB (Figure 1f) autoradiography. The frontal gray matter with abundant $\text{A}\beta$ plaques had considerably lower [^{18}F]THK-523 (Figure 2f) binding compared with [^{11}C]PiB (Figure 1f) and [^{11}C]BF-227 (Figure 2g, (E)-5-(2-(6-(2-fluoroethoxy)benzo[d]oxazol-2-yl)vinyl)-N-methyl-N-[^{11}C]methyl-thiazol-2-amine), whereas the converse was true for the NFT-rich hippocampal CA1 area in the AD brain [101]. [^{18}F]THK-523 (Figure 2f) binding in the entorhinal cortex corresponded better to Gallyas silver staining than to tau immunostaining, indicating better labeling of extracellular tau (ghost tangles) [47]. The abundant binding of [^{18}F]THK-523 (Figure 2f) to the CA1 area of the AD hippocampus was also confirmed by Tago et al., who reported a pattern matching the numerous tau immune-positive NFTs [102]. In another study, [^3H]THK-523 bound to AD brain homogenates with an apparent K_D of 3.5 nM [103]. Molecular docking studies indicated a lower affinity of THK-523 (Figure 2d) to MAO-B compared with other quinoline derivatives [104].

Another *in vitro* competition assay revealed low affinity of [^{18}F]THK-523 (Figure 2f) to recombinant tau fibrils ($K_i = 59$ nM) and PHF ($K_i = 87$ nM) in AD brain homogenates. This led the researchers to consider [^{18}F]THK-523 (Figure 2f) as a nonselective tau tracer and to note that synthetic tau filaments are an imperfect binding model of native tau filaments *in vivo* [105]. Immunohistochemical and THK-523 (Figure 2d) fluorescence studies of AD brain sections by Fodero-Tavoletti et al. showed selective binding to argyrophilic tau filaments (PHF-tau) in the hippocampus and frontal regions, but little binding for non-AD tauopathies [106]. This might reflect the differing types of ultrastructure in tau fibrils [36]. Another study showed faint labeling of $\text{A}\beta$ plaques by [^{18}F]THK-523 (Figure 2f) in AD brain sections, but no labeling of α -synuclein deposits in Lewy bodies of substantia nigra post mortem samples from patients with Parkinson's disease [106]. Although incomplete specificity might limit the clinical utility of [^{18}F]THK-523 (Figure 2f) PET, its selectivity for one ultrastructural form of tau (PHFs forming NFTs) might allow useful differentiation between disease entities.

2.2.2. PET Studies with [¹⁸F]THK-523

MicroPET analysis demonstrated a significant correlation between the cerebral retention of [¹⁸F]-THK-523 (Figure 2f) in rTg4510 tau transgenic mice relative to wildtype and A β (APP/PS1) transgenic mice and the subsequent tau immunostaining [100,106]. A mouse PET study by Villemagne et al. [47] demonstrated high brain uptake and rapid clearance, along with the absence of lipophilic metabolites. The first-in-man PET study [47] showed greater white matter retention of [¹⁸F]THK-523 (Figure 2f) compared with gray matter in HC participants, but elevated gray matter binding in widespread neocortical regions and hippocampus of AD patients. The binding pattern in patients correlated with PHF-tau distribution in the post mortem brain, being higher in temporal and parietal lobes than in frontal regions. The retention of [¹⁸F]THK-523 (Figure 2f) in the hippocampus and insula of HCs without dementia with high A β accumulation to [¹¹C]PiB (Figure 1f) PET resembled that of AD patients, but cortical retention of [¹⁸F]THK-523 (Figure 2f) was otherwise higher in AD patients. In the whole neocortex, which represents the spatial distribution of tau in Braak V/VI, the tracer had a Cohen's d of 3.42 for discriminating AD patients and HCs (Table 1). Hippocampal retention correlated inversely with hippocampal atrophy and several cognitive parameters. However, white matter retention of [¹⁸F]THK-523 (Figure 2f) interfered significantly with the detection of cortical tau in AD patients, which might indicate native tau or PHF deposits in the white matter of AD subjects [107]. The resultant need for partial volume correction of tau PET images was discouraging for further clinical use of the tracer [47].

2.2.3. [¹⁸F]THK-951

A search for compounds with lesser hydrophobicity yielded [¹¹C]-THK-951 (Figure 3a, 2-(4-([¹¹C]methyl)-amino)phenyl)quinoline-7-ol) through hydroxylation of BF-158 (Figure 2a) [102], which was sufficiently lipophilic to penetrate the BBB (logP 1.28) and showed high affinity for displacing [¹⁸F]THK-523 (Figure 2f) from AD brain homogenates ($K_i = 21$ nM). Fluorescence binding assays with THK-951 (Figure 3a) showed binding to recombinant K18 Δ 280K-tau fibrils. AD hippocampus sections showed distinct THK-951 (Figure 3a) fluorescence staining of NFTs and neuropil threads. In an ex vivo biodistribution study in normal mice, [¹¹C]THK-951 (Figure 3a) showed very rapid washout from the brain, greatly exceeding that for [¹⁸F]THK-523 (Figure 2f) (1.9) and [¹⁸F]THK-5117 (Figure 3d) [23]. Labeling of THK-523 (Figure 2d) with ¹¹C instead of ¹⁸F slightly decreased the binding affinity to tau aggregates, which was compensated by improved brain kinetics, i.e., faster washout. Autoradiography analysis of AD hippocampal sections with [¹¹C]THK-951 (Figure 3a) showed high binding in the CA1 region of the hippocampus, in a pattern matching with [¹⁸F]THK-523 (Figure 2f) binding and tau immunohistochemistry (IHC), but distinct from that of A β . [¹¹C]THK-951 (Figure 3a) gave a good tradeoff between high binding affinity for tau and appropriate BBB permeability. No further studies have evaluated [¹¹C]THK-951 (Figure 3a) and its derivatives due to its relatively low affinity to tau compared with [¹⁸F]THK-523 (Figure 2f), [¹⁸F]THK-5105 (Figure 3b), and [¹⁸F]THK-5117 (Figure 3d).

2.2.4. [¹⁸F]THK-5105 and [¹⁸F]THK-5117

Due to the inadequacies of [¹⁸F]THK-523 (Figure 2f) and [¹⁸F]THK-951, researchers developed three new 2-arylquinoline derivatives through several optimization processes, namely, [¹⁸F]THK-5105 (6-[(3-¹⁸F-fluoro-2-hydroxy)propoxy]-2-(4-dimethyl aminophenyl) quinoline, Figure 3b), [¹⁸F]THK-5116 (6-[(3-¹⁸F-fluoro-2-hydroxy)propoxy]-2-(4-aminophenyl)quinoline, Figure 3c), and [¹⁸F]THK-5117 (6-[(3-¹⁸F-fluoro-2-hydroxy)propoxy]-2-(4-methylaminophenyl)quinoline, Figure 3d) [105]. These compounds were derived from BF170 through the addition of a secondary alcohol to the fluoroethoxy chain along with N-dimethylation to yield [¹⁸F]THK-5105 (Figure 3b) and N-monomethylation for [¹⁸F]THK-5117 (Figure 3d). These modifications improved the pharmacokinetic profiles of the tracers. However, [¹⁸F]THK-

5116 (Figure 3c) was not further studied due to its brain kinetics and lower specific signal in AD brain sections [63].

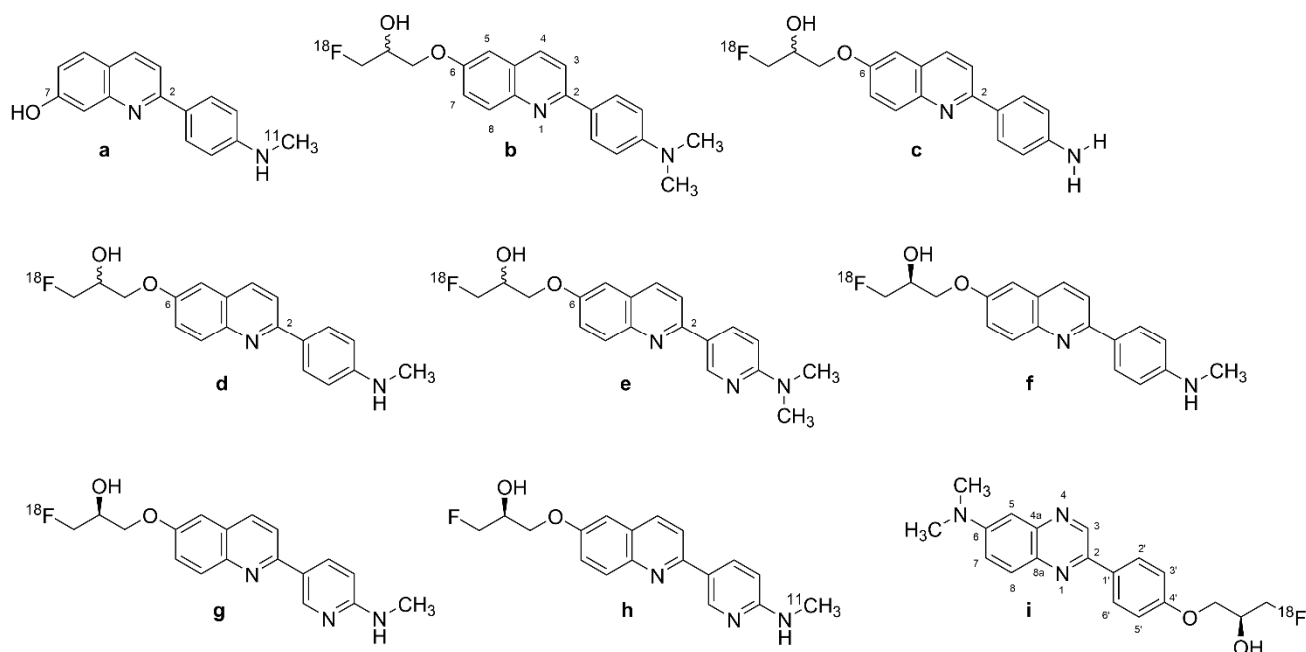


Figure 3. Structure of Tohoku-compounds (labeled 2-arylquinolines, [^{18}F]-2-AQ and [^{11}C]-2-AQ derivatives). (a): [^{11}C]THK-951, (b): [^{18}F]THK-5105, (c): [^{18}F]THK-5116, (d): [^{18}F]THK-5117, (e): [^{18}F]THK-5129, (f): [^{18}F]THK-5317, (g): [^{18}F]THK-5351 or [^{18}F]GE-216, (h): [^{11}C]THK-5351, (i): [^{18}F]-S-16.

The logP values were 3.0 for [^{18}F]THK-5105 (Figure 3b) and 2.3 for [^{18}F]THK-5117 (Figure 3d) [108]. The greater lipophilicity of [^{18}F]THK-5105 (Figure 3b) imparted higher nonspecific binding to white matter, brainstem, and thalamus [109,110]. [^{18}F]THK-5105 (Figure 3b) showed two classes of binding sites on K18 Δ 280 K-tau fibrils ($K_{D1} = 1.5$ nM, $K_{D2} = 7.4$ nM, $B_{\text{max}1} = 6.9$ pmol/nmol fibrils, and $B_{\text{max}2} = 20$ pmol/nmol fibrils) and one [^{18}F]THK-5105 (Figure 3b) binding site for A β_{1-42} ($K_{D1} = 36$ nM) [105]. Medial temporal AD brain homogenates containing a high density of tau and a moderate density of A β showed higher affinity of [^{18}F]THK-5105 (Figure 3b) ($K_D = 2.6$ nM) and [^{18}F]THK-5117 (Figure 3d) ($K_D = 5$ nM) than for [^{18}F]THK-523 (Figure 2f) ($K_D = 87$ nM). In vitro autoradiography of AD brain sections with [^{18}F]THK-5105 (Figure 3b) and [^{18}F]THK-5117 (Figure 3d) at tracer concentrations was also consistent with the tau staining pattern (Gallyas–Braak staining). IHC results matched the [^{18}F]THK-5105 (Figure 3b) and [^{18}F]THK-5117 (Figure 3d) binding in the deep layers of gray matter in the medial temporal cortex and CA1 area of the hippocampus, but there was a mismatch with the [^{11}C]PiB (Figure 1f) binding pattern and A β IHC staining. [^{18}F]THK-5105 (Figure 3b) and [^{18}F]THK-5117 (Figure 3d) did not label the hippocampus of healthy control subjects. [^{18}F]THK-5116 (Figure 3c) was not pursued as a tau PET tracer due to its inadequate affinity and high nonspecific binding in AD brain sections. Biodistribution studies of mice suggested that [^{18}F]THK-5105 (Figure 3b) and [^{18}F]THK-5117 (Figure 3d) had better brain uptake and washout when compared with [^{18}F]THK-523 (Figure 2f).

[^3H]THK-5117 did not bind to MAO-B in vitro in post mortem brain samples from AD patients [110]. However, high nonspecific white matter accumulation was observed for [^{18}F]THK-5117 (Figure 3d), likely due to binding to β -sheet structures in myelin [64]. Due to the higher selectivity and specificity of the *S* enantiomer compared with the *R* enantiomer of [^{18}F]THK-5117 (Figure 3d) to tau aggregates in AD brains, a new tracer called [^{18}F]THK-5317 (Figure 3f, 6-((3-[^{18}F]fluoro-2-hydroxy)propoxy)-2-(4-methylaminophenyl) quinoline) was developed, which proved to have superior pharmacokinetics in rodents. However,

both enantiomers had a similar distribution in autoradiography studies of post mortem AD brains [108,109].

Human PET Studies of [¹⁸F]THK-5105 and [¹⁸F]THK-5117

A PET study showed greater gray matter retention and lower white matter retention for [¹⁸F]THK-5105 (Figure 3b) when compared with [¹⁸F]THK-523 (Figure 2f) [63]. [¹⁸F]THK-5105 (Figure 3b) possessed higher peak brain uptake than [¹⁸F]THK523 (Figure 2f), [¹⁸F]T807 (see Section 2.4), [¹⁸F]T808 (see Section 2.4), 2-[4-(2-[¹⁸F]fluoroethyl)-1-piperidiny]pyrimido [1,2-a]benzimidazole, and [¹¹C]PBB3 (see Section 2.5.1), 2-[(1E,3E)-4-[6-[¹¹C]methylamino)pyridin-3-yl]buta-1,3-dienyl]-1,3-benzothiazol-6-ol, obtaining an SUC of 4.5 in the cerebellum. The tracer showed high non-specific accumulation in subcortical white matter, thalamus, and brainstem. However, tracer retention in subcortical white matter was lower than that of [¹⁸F]THK523 [12]. In addition, [¹⁸F]THK-5105 (Figure 3b) had high gray matter background signals resulting from its slow kinetics and high lipophilicity.

The first [¹⁸F]THK-5105 (Figure 3b) PET study showed differentiation of AD patients from HCs, and mismatch with the binding pattern of [¹¹C]PiB (Figure 1f) [63], despite fairly high nonspecific binding of the tau tracer in white matter, brainstem, and thalamus [111]. [¹⁸F]THK-5105 (Figure 3b) was not investigated further as a tau PET tracer in humans. Being more hydrophilic, [¹⁸F]THK-5117 (Figure 3d) had faster brain kinetics in mice than did [¹⁸F]THK-5105 (Figure 3b) [112]. The first [¹⁸F]THK-5117 (Figure 3d) PET study in AD patients showed higher retention in the temporal lobe, correlating to an extent with the individual degree of cognitive impairment, and not overlapping with [¹¹C]PiB (Figure 1f) binding [64]. A longitudinal [¹⁸F]THK-5117 (Figure 3d) PET study revealed annual increases in tracer retention in the middle and inferior temporal gyri and fusiform gyri of AD patients, which correlated with their declining cognitive function [113]. Compartmental analysis of [¹⁸F]THK-5317 (Figure 3f) uptake relative to a metabolite-corrected input function indicated reversible binding kinetics in MCI and AD patients [114].

Cross-sectional [¹⁸F]THK-5317 (Figure 3f) PET studies successfully differentiated MCI and AD patients from HCs, showing a pattern of tracer uptake in accord with post mortem tau studies [115]. Test–retest variability was low (<4%) and white matter uptake was lower than for [¹⁸F]THK-5117 (Figure 3d). However, off-target binding in the basal ganglia was evident. The high white matter binding of [¹⁸F]THK-5117 (Figure 3d) and [¹⁸F]THK-5317 (Figure 3f), probably reflecting β -sheet structures in myelin basic protein, reduces the clinical utility of these tracers [114,116]. The estimated Cohen's *d* between AD and HC groups was 3.58 in the inferior temporal cortex for [¹⁸F]THK-5105 (Figure 3b) [63] (Table 1). Cohen's *d* for the contrast between AD and HC groups for [¹⁸F]THK-5117 (Figure 3d) was as high as 2.74 in the inferior temporal lobe (Table 1) [64].

2.2.5. [¹⁸F]THK-5351

The high white matter binding of [¹⁸F]THK-5117 (Figure 3d) and [¹⁸F]THK-5317 (Figure 3f) (*S* enantiomer of [¹⁸F]THK-5117 (Figure 3d)) motivated the development of [¹⁸F]THK-5351 (Figure 3g, GE-216, (2*R*)-1-[¹⁸F]fluoro-3-[2-[6-(methylamino)pyridin-3-yl]quinolin-6-yl]oxypropan-2-ol), the 4-methyl-aminopyridyl-analog of THK-5117 [116]. Lesser lipophilicity of the new tracer ($\log P = 2.3$) results from the substitution of pyridine at 2-aryl group for benzene, imparts lower nonspecific binding to white matter along with a higher affinity for AD tau compared with [¹⁸F]THK-5117 (Figure 3d), and higher selectivity for tau over $A\beta$. [¹⁸F]THK-5351 (Figure 3g) displayed higher binding affinity ($K_D = 2.9$ nM) to hippocampal homogenates of AD brains than did [¹⁸F]THK-5117 (Figure 3d), and autoradiography indicated a greater gray vs. white matter binding ratio compared with previous quinoline derivatives. Autoradiography in midbrain sections from the cognitively normal individuals showed saturable binding of [¹⁸F]THK-5351 (Figure 3g) in the substantia nigra, and a saturation binding assay in melanin-containing cells showed high capacity low-affinity binding sites for the tracer on B16F10 cells ($K_D = 440$ nM) [117]. [¹⁸F]THK-5351 (Figure 3g) had a binding ratio of 2.5 in the substantia nigra, and competitive binding

assays of THK-5351 for [^{18}F]THK-5351 (Figure 3g) binding to B16F10 melanin-producing cells revealed moderate affinity ($K_i = 0.22 \mu\text{M}$).

Human PET Studies of [^{18}F]THK-5351

PET studies have shown a higher gray-to-white ratio and faster kinetics for [^{18}F]THK-5351 (Figure 3g) compared with other quinoline derivatives [118]. [^{18}F]THK-5351 (Figure 3g) PET in AD patients indicated lower white matter binding and higher binding in the temporal lobe and other regions susceptible to AD neuropathology compared with [^{18}F]THK-5117 (Figure 3d) and [^{18}F]THK-5317 (Figure 3f) [119–121]. Cortical uptake in AD patients did not match the expected NFT pathology pattern. Comparative PET revealed better agreement of the [^{11}C]THK-5351 (Figure 3h) distribution in AD patients with known NFT neuropathology compared with [^{11}C]PBB3 (Figure 6a) [122].

A 2020 PET study showed off-target binding of [^{18}F]THK-5351 (Figure 3g) in the basal ganglia and, to a lesser extent, in the cerebral cortex of healthy volunteers, which was attributed to MAO-B, apparently accounting for the imperfect match with tau pathology [123]. Another study comparing [^{18}F]THK-5351 (Figure 3g) with [^{18}F]AV-1451 (Figure 5a, 7-(6-[^{18}F]fluoro-pyridin-3-yl)-5H-pyrido[4,3-b]indole) found more prominent cortical uptake of [^{18}F]THK-5351 (Figure 3g) in FTD patients, and higher [^{18}F]AV-1451 (Figure 5a) uptake in AD [124]. [^{18}F]THK-5351 (Figure 3g) proved less sensitive and specific than [^{18}F]AV-1451 (Figure 5a) to tau pathology in AD but also served for the detection of non-AD tauopathies. There was a strong correlation between [^{18}F]THK-5351 (Figure 3g) and [^{18}F]THK-5317 (Figure 3f) binding patterns in the same individuals [121].

[^{18}F]THK-5351 (Figure 3g) did not exhibit significant off-target binding in venous sinuses, basal ganglia, or choroid plexus in some studies [119–121], but others reported off-target binding in the basal ganglia, midbrain, and thalamus, and higher affinity to MAO-B compared with [^{18}F]THK-5117 (Figure 3d). Its binding correlated with levels of the astrocyte marker GFAP, confirming an association with MAO-B [112]. This off-target binding of [^{18}F]THK-5351 (Figure 3g) exceeded that of [^{18}F]THK-5317 (Figure 3f) [125]. Indeed, the in vivo distribution of [^{18}F]THK-5351 (Figure 3g) correlated with the post mortem distribution of MAO-B. The off-target binding of [^{18}F]THK-5351 (Figure 3g) in basal ganglia, white matter, midbrain, and thalamus also exceeded that of [^{18}F]AV-1451 (Figure 5a) [124]. Administration of an MAO-B inhibitor reduced the off-target binding of [^{18}F]THK-5351 (Figure 3g) by about 50% [126] according to SUV. However, the SUVr index indicated no statistically significant reduction in [^{18}F]THK-5351 (Figure 3g) off-target binding [127]. Similar binding patterns between [^{18}F]THK-5351 (Figure 3g) and other quinoline derivatives imply a more general interaction of these tracers with MAO-B [125]. A post mortem study of an AD patient who had undergone ante mortem [^{18}F]THK-5351 (Figure 3g) PET demonstrated [^3H]THK-5351 binding to MAO-B, which was compatible with previous PET findings [128], thus arguably disqualifying [^{18}F]THK-5351 (Figure 3g) as a selective tau biomarker in AD diagnosis. However, Cohen's *d* values for the contrast between AD patients and HCs were as high as 2.44 in the frontal lobe, indicating that the tracer could serve operationally for the detection of AD pathology (Table 1) [129]. Another study [67] reported a Cohen's *d* of 3.00 in inferior temporal gyrus for the contrast of AD and HC groups (Table 1).

2.2.6. 2-Phenylquinoxaline Derivatives

[^{18}F]-S16 ((*S*)-1-(4-(6-(dimethylamino)quinoxalin-2-yl)phenoxy)-3-[^{18}F]fluoro propan-2-ol, [^{18}F]-S16, Figure 3i) is a novel 2-phenylquinoxaline tau tracer [65,95]. Initial thinking was that the 2-phenylquinoxaline scaffold detected β -sheet structures in $\text{A}\beta$, but later in vitro investigations showed binding to NFTs [130]. The optimization of THK tracers by adding a fluoropropanol side chain gave rise to [^{18}F]THK-5117 (Figure 3d) and [^{18}F]THK-5351 (Figure 3g) [64,116]. The introduction of a chiral 2-fluoromethyl-1,2-ethylenediol side chain to the position-4' and a $-\text{N}(\text{CH}_3)_2$ group in position-6 of the 2-phenylquinoxaline scaffold resulted in higher selectivity to tau over $\text{A}\beta$ and improved brain kinetics of [^{18}F]-

S16 (Figure 3i). The 4'-O-[(S)-1-[¹⁸F]fluoropropan-2-ol] substituent of [¹⁸F]-S16 (Figure 3i) increased the hydrophilicity (logD = 2.61, clogP = 3.01) [130]. Radiosynthesis of [¹⁸F]-S16 (Figure 3i) was achieved in a high-yield, fully automated process [95].

The hydrophilic characteristics of the tracer resulted in the increased selectivity for tau over A β (35-fold; K_i = 356 nM in competition with [³H]PiB) [95]. [³H]-S16 had K_i = 10 nM in quantitative binding assays of AD brain homogenates in competition with [³H]THK-523 binding [130]. However, the tracer only weakly displaced [³H]T807, with K_i = 611 nM. The IC₅₀ of the tracer for MAO-B was >10 μ M, as compared with 0.5 μ M for THK-5351. Autoradiography of entorhinal cortex from human AD brain sections showed high binding of [¹⁸F]-S16 (Figure 3i), which was associated with tau fluorescent staining and was displaceable by THK-5371.

MicroPET studies with [¹⁸F]-S16 (Figure 3i) in rTg4510 mice showed two-fold higher BBB penetration than for [¹⁸F]THK-5351 (Figure 3g), with notably higher initial brain uptake (11% ID/g) and rapid washout [130]. The tracer did not show *in vivo* defluorination. Initial human PET studies of [¹⁸F]-S16 (Figure 3i) in AD showed rapid brain uptake, with slower clearance compared with [¹⁸F]THK5317 [65,94]. There was substantial hepatobiliary excretion and an absence of defluorination *in vivo* [95,130]. The parietal lobe, posterior cingulate, and precuneus showed the highest SUVs in AD patients. Another PET study [94] showed elevated uptake in AD patients compared with HCs, particularly in the bilateral occipital cortex, posterior cingulate cortex/precuneus, and lateral frontal cortex. Although there were no statistically significant differences in SUVr values between AD patients and HCs in the medial temporal lobe [95], there was an overall inverse correlation between [¹⁸F]-S16 (Figure 3i) binding and brain metabolism to [¹⁸F]FDG PET. Furthermore, [¹⁸F]-S16 (Figure 3i) PET differentiated AD and HC groups with Cohen's d values ranging from 0.63 to 1.78 (Table 1), and an inverse relationship between cortical [¹⁸F]-S16 (Figure 3i) uptake with MMSE scores [94,95]. The tracer had little binding in white matter, choroid plexus, and the sagittal sinus [94,95]. However, there was some off-target binding of [¹⁸F]-S16 (Figure 3i) in the lentiform nucleus and thalamus [95]. There was [¹⁸F]-S16 (Figure 3i) retention in the brainstem, substantia nigra, and basal ganglia of both healthy controls and AD patients, again consistent with off-target binding.

2.3. Derivatives of Lansoprazole and Astemizole

Lansoprazole (Figure 4a, (2-[[3-methyl-4-(2,2,2-trifluoroethoxy)pyridin-2-yl]methylsulfanyl]-1H-benzimidazole) and astemizole (Figure 4b, 1-[(4-fluorophenyl)methyl]-N-[1-[2-(4-methoxyphenyl)ethyl]piperidin-4-yl]benzimidazol-2-amine) are benzimidazole-derivative proton pump inhibitors. They proved to have high affinity for NFTs; the K_is for heparin-induced tau filaments were 2.5 nM for lansoprazole (Figure 4a) and 1.9 nM for astemizole (Figure 4b), and corresponding K_is to PHF-tau were 2.1 nM and 830 nM, respectively [131]. Other *in vitro* autoradiography studies of human AD brain sections with N-methyl lansoprazole (Figure 4c, NML) labeled with [¹¹C] (Figure 4d, [¹¹C]NML) and [¹⁸F] (Figure 4e, [¹⁸F]NML) revealed a high affinity for tau aggregates in AD, with 12-fold selectivity for tau over A β (K_D amyloid/K_D tau) [132]. [¹⁸F]NML (Figure 4e) had a K_D of 0.7 nM toward HITF [133,134], whereas autoradiography studies of AD brain homogenates demonstrated binding to 3R and 4R tau with a K_D of 8.2 nM [132].

Preclinical *in vivo* studies of [¹⁸F]NML (Figure 4e) and [¹¹C]NML (Figure 4d) revealed adequate BBB clearance in rhesus macaques, but no entry into the brains of mice unless pretreated with cyclosporine, a P-glycoprotein 1 transporter inhibitor [132,135–137]. However, astemizole derivatives were impermeable to the mouse BBB despite cyclosporine treatment [133,136]. An [¹⁸F]NML (Figure 4e) PET study in healthy humans showed rapid entry and washout in the brain, with a maximum SUV of 3–4 in the gray matter of the cerebellum and cortex [133,134]. There was low tracer retention in the brains of AD, MCI, and PSP patients, such that [¹⁸F]NML (Figure 4e) was abandoned, despite promising *in vitro* binding properties [134]. The structure of astemizole-based radiotracers is depicted in Figure 4f.

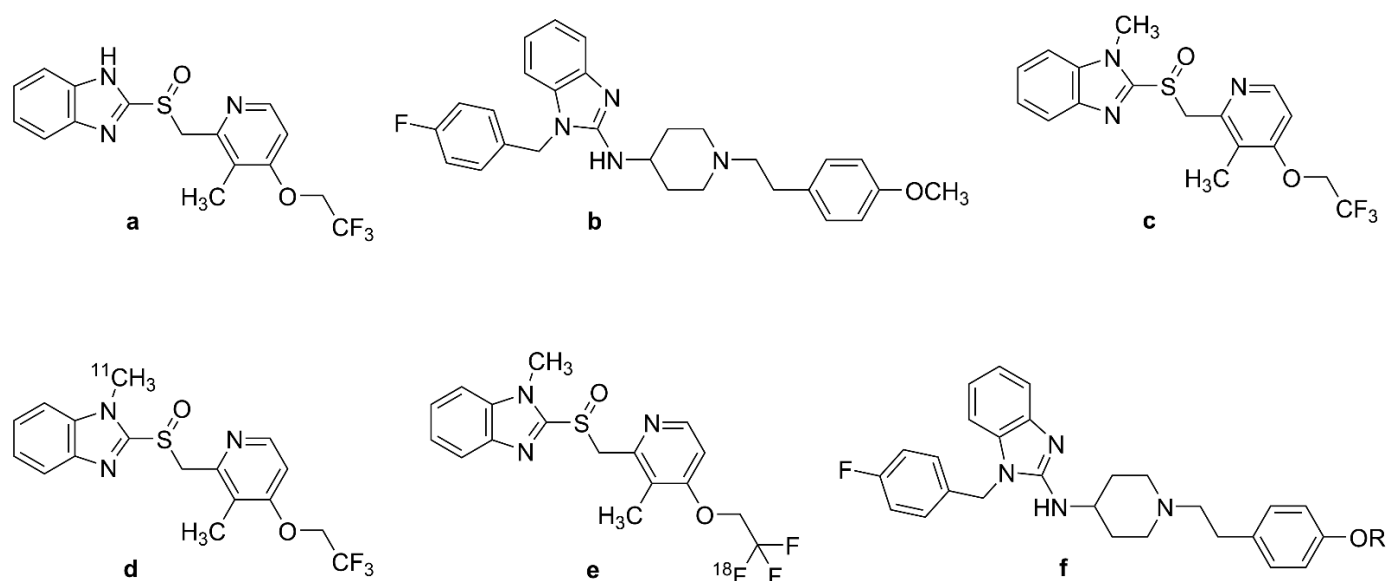


Figure 4. Chemical structures of lansoprazole, astemizole, and their labeled derivatives. (a): lansoprazole, (b): astemizole, (c): *N*-methyl-lansoprazole (NML), (d): [¹¹C]-*N*-methyl-lansoprazole ([¹¹C]NML), (e): [¹⁸F]-*N*-methyl-lansoprazole ([¹⁸F]NML), (f): astemizole-based radiotracers, R = ¹¹CH₃, ¹⁸FCH₂CH₂.

2.4. Benzimidazopyridine and Benzimidazopyrimidine Derivatives: Flortaucipir and T808

[¹⁸F]T807 (Figure 5a, 7-(6-[¹⁸F]fluoro-pyridin-3-yl)-5*H*-pyrido[4,3-*b*]indole), also known as [¹⁸F]flortaucipir and [¹⁸F]AV-1451 (Figure 5a), is the first FDA-approved tau tracer, marketed since 2020 under the name of TAUVID™ [25]. It is the most widely studied and used tau tracer, having attracted the attention of many researchers since its first discovery in 2013. [¹⁸F]flortaucipir (Figure 5a) and its congener [¹⁸F]T808 (Figure 5b), 2-(4-(2-[¹⁸F]fluoroethyl)piperidin-1-yl)benzo[4,5]imidazo[1,2-*a*]pyrimidine were discovered through the process of optimization of two other tau ligands, T726 and T557, aiming to increase their selectivity for PHF-tau over Aβ₁₋₄₂ and to improve their pharmacokinetic characteristics [137–139].

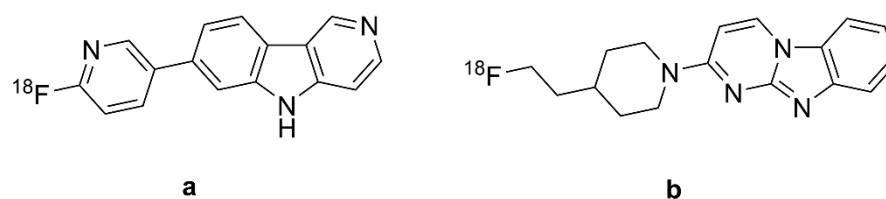


Figure 5. Chemical structures of [¹⁸F]flortaucipir and [¹⁸F]T808. (a): [¹⁸F]flortaucipir or [¹⁸F]T807 or AV-1451, (b): [¹⁸F]T808 or AV-680.

2.4.1. In Vitro Studies with [¹⁸F]Flortaucipir and [¹⁸F]T808

In vitro saturation binding assays of immunopurified PHF-tau from AD brain homogenates indicated a K_D of 0.7 nM and B_{max} of 310 pmol/mg [25], whereas autoradiographic studies of the frontal lobe from post mortem AD patients indicated a K_D of 15 nM [140] and 14.6 nM [138] for PHF-tau. Combined immunohistochemistry and in vitro autoradiography studies of human AD brain sections revealed that [¹⁸F]T807 (Figure 5a) and [¹⁸F]T808 (Figure 5b) both had higher binding to PHF-tau aggregates than to Aβ [138]; [¹⁸F]Flortaucipir (Figure 5a) had a logP of 1.7, predicting adequate brain penetration and fast washout. Screening studies indicated limited off-target binding to more than 72 CNS targets. In vitro autoradiography revealed colocalization of [¹⁸F]flortaucipir (Figure 5a) with tau aggregates and no colocalization of the tracer with Aβ, TDP43, and α-synuclein [138,141].

Nonetheless, some studies demonstrated off-target binding of [^{18}F]flortaucipir (Figure 5a) to MAO-A and MAO-B [132,142], although this was not reported in other studies [141,143,144]. On the other hand, [^3H]flortaucipir had a K_D of 1.6 nM for human recombinant MAO-A protein [25], as might be expected from the β -carboline motif. Another study reported saturable binding of [^{18}F]flortaucipir (Figure 5a) to melanoma cells with $K_D = 670$ nM. The post mortem [^{18}F]flortaucipir (Figure 5a) binding pattern in AD brains correlated well with NFT Braak staging [141]. However, specific binding was not identifiable in the hippocampus due to spillover of off-target binding from the nearby choroid plexus [143]. CSF-tau levels correlated with [^{18}F]flortaucipir (Figure 5a) retention in brain at early stages of AD, and also in presymptomatic patients, especially in the neocortex and parahippocampal gyrus [142,145,146]. There was off-target binding in the leptomenigeal melanin, substantia nigra, choroid plexus, and cerebral vessels of AD patients [141,143]. [^{18}F]flortaucipir (Figure 5a) retention in these regions did not correlate with NFT Braak staging. In vitro binding studies with AD brains also demonstrated off-target binding of the tracer to MAO-A and MAO-B [125,147], although [^{18}F]flortaucipir (Figure 5a) exhibited ten-fold lower affinity to MAO-B than did [^3H]THK-5351. Another PET study in PD patients did not indicate any effect of ongoing treatment with an MAO-B inhibitor [148].

2.4.2. PET Studies with [^{18}F]Flortaucipir and [^{18}F]T808

BBB penetration of the [^{18}F]flortaucipir was confirmed in mouse PET studies showing rapid brain penetration and moderate washout [138]; kidney clearance was the main route of systemic elimination. [^{18}F]Flortaucipir (Figure 5a) exhibited minor defluorination in mice, but analysis of brain homogenates did not detect labeled metabolites. Initial PET studies of AD patients with [^{18}F]flortaucipir (Figure 5a) [145] and [^{18}F]T808 (Figure 5b) [149] revealed their preferential retention in brain areas containing PHF-tau filaments. Besides, both tracers had low white matter binding, thus yielding good contrast between white and gray matter. However, [^{18}F]T808 (Figure 5b) PET was not pursued due to its in vivo defluorination in rodents, resulting in cranial labeling [139,140]. [^{18}F]Flortaucipir (Figure 5a) retention in AD patients correlated with disease severity, although the tracer uptake showed considerable variability in HCs, especially those younger than 40 years [140]. Another study showed correlations between tracer retention and clinical stage in AD, MCI, and $\text{A}\beta$ + cognitively normal adults [74]. [^{18}F]Flortaucipir (Figure 5a) PET differentiated AD patients from MCIs and healthy controls [140,150–153]. In the contrast between AD and healthy control groups, Cohen's d ranged from one–two in studies of patients with moderate disease (MMSE circa 20), but was greater than three in a study of advanced disease (Table 1). The tracer retention and distribution pattern in [^{18}F]flortaucipir (Figure 5a) PET of AD brains correlated with Braak staging of NFT pathology [154], and the area coverage of [^{18}F]AV-1451 (Figure 5a) retention correlated with disease severity [155]. [^{18}F]flortaucipir (Figure 5a) PET in conjunction with post mortem pathology reliably detected Braak VI tau pathology, but the tracer was not sensitive to Braak I–IV tau pathology in AD patients compared with young tau-negative HCs [156].

[^{18}F]Flortaucipir (Figure 5a) retention occurred mostly in posterior parietal and inferior temporal cortices of AD patients, and there was some correlation between [^{18}F]flortaucipir (Figure 5a) retention and impaired cognition, even in seemingly healthy older subjects [145,153]. Early onset AD patients had increased tracer uptake across the neocortex compared with HCs, and late-onset AD patients exhibited significantly elevated tracer uptake mostly in the temporal lobe [157]. [^{18}F]Flortaucipir (Figure 5a) PET showed higher retention in $\text{A}\beta$ + patients without dementia, but not in $\text{A}\beta$ – cases [74]. Another study revealed higher tracer uptake in early onset AD cases compared with late-onset ones in the premotor and prefrontal cortex and inferior parietal cortex [157].

2.5. Pyridinyl-Butadienyl-Benzothiazole (PBB) Derivatives

2.5.1. [¹¹C]PBB3

[¹¹C]PBB3 (Figure 6a) (2-((1*E*,3*E*)-4-(6-((methyl-¹¹C)amino)pyridin-3-yl)buta-1,3-dien-1-yl) benzo[d]thiazol-6-ol) is a first generation tau tracer developed by Higuchi et al. [158] by screening a number of fluorescent compounds binding to β -sheet structures. PBB3 and [¹¹C]PBB3 (Figure 6a) showed appropriate brain kinetics and rapid peripheral metabolism in plasma and brain specimens and were selected for further investigation [159]. PBB3 has high selectivity for tau aggregates ($K_D = 2.6$ nM), with a 50-fold higher affinity for tau than for A β [159,160]. Initial autoradiography studies showed binding in the CA1 and subiculum regions of the hippocampus of AD patients, and revealed tau pathology in non-AD tauopathies, suggesting a preferred interaction with 4R tau [159,161]. Comparison of [¹¹C]PBB3 (Figure 6a) and [¹⁸F]flortaucipir (Figure 5a) binding in AD brain homogenates revealed distinct selectivity of the former tracer towards various forms of tau fibrils, especially dystrophic neurites and NFTs [162]. There was no off-target binding of [¹¹C]PBB3 (Figure 6a) to MAO [160], and the ligand had low affinity for A β [163] and α -synuclein aggregates [164]. Nonetheless, [¹¹C]PBB3 (Figure 6a) binding seemed to have a greater association with A β than was seen with [¹⁸F]THK5351 (Figure 3g) [122]. Indeed, the distribution pattern of [¹¹C]PBB3 (Figure 6a) seemed relatively less indicative of AD tau pathology.

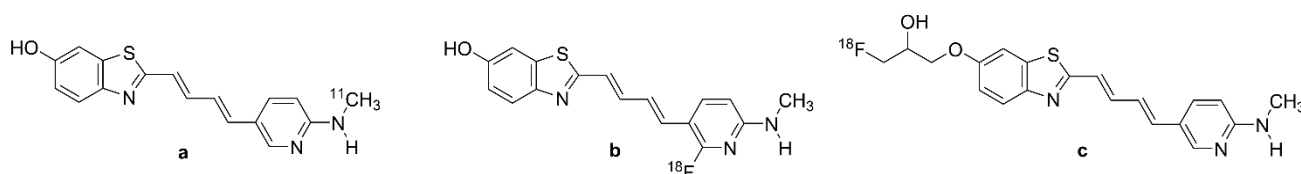


Figure 6. Chemical structure of labeled pyridinyl-butadienyl-benzothiazole derivatives. (a): [¹¹C]PBB3, (b): [¹⁸F]PBB3, (c): [¹⁸F]PM-PBB3 or [¹⁸F]APN-1607.

[¹¹C]PBB3 (Figure 6a) PET studies in PS19 mice expressing 4R tau isoform mutations revealed rapid brain uptake and tracer binding to NFTs [165]. However, the tracer yielded a lipophilic metabolite in mice, which likely crossed the BBB and contributed to the background signal in vivo [165]. The first [¹¹C]PBB3 (Figure 6a) PET study in AD patients demonstrated labeling of medial and lateral temporal cortices and frontal cortex, and good discrimination of AD and HC groups, as well as mismatches with [¹¹C]PIB (Figure 1f) binding in the same subjects [159], as was confirmed in another [¹¹C]PBB3 (Figure 6a) PET study [166]. The binding of [¹¹C]PBB3 (Figure 6a) correlated with cognitive decline and gray matter atrophy in AD patients [77]. [¹¹C]PBB3 (Figure 6a) PET gave a Cohen's *d* for discrimination of AD patients and HCs in the range of two–three (Table 1).

Off-target binding in the choroid plexus, longitudinal sinus, and basal ganglia, and metabolic instability have limited the human application of [¹¹C]PBB3 (Figure 6a) [4]. Furthermore, the brief half-life of carbon-11 disfavors its routine use. [¹¹C]PBB3 (Figure 6a) undergoes photoisomerization under fluorescent light, which results in a rapid decrease in purity [167]. In addition, rapid metabolism of [¹¹C]PBB3 (Figure 6a) in vivo hinders its brain uptake, while lipophilic radiometabolites may confound the brain signal. Hence, [¹⁸F]PM-PBB3 (Figure 6c) was developed to overcome these shortcomings.

2.5.2. [¹⁸F]PM-PBB3

[¹⁸F]PM-PBB3 (Figure 6c, APN-1607, 1-[¹⁸F]fluoro-3-((2-((1*E*,3*E*)-4-(6-(methylamino)pyridin-3-yl)buta-1,3-dien-1-yl)benzo[d]thiazol-6-yl)oxy)propan-2-ol), also known as [¹⁸F]florzolotau, is a propylated analogue of [¹¹C]PBB3 (Figure 6a) [166,168]. It was proposed to circumvent the off-target binding of [¹¹C]PBB3 (Figure 6a), metabolic instability, and the brief half-life of ¹¹C compared with ¹⁸F [165,167]. Indeed, [¹⁸F]PM-PBB3 (Figure 6c) has greater metabolic stability, higher PET scan throughput, and broader availability than

[¹¹C]PBB3 (Figure 6a) [169]. Autoradiography studies of frontal AD brain homogenates showed that [¹⁸F]PM-PBB3 (Figure 6c) has a K_D of 7.6 nM [170], comparable to that of [¹¹C]PBB3 (Figure 6a). The B_{max} of 5.7 nmol/g in AD brain homogenates thus predicted a high binding potential ($B_{max}/K_D = 750$), and the ligand was without binding to A β or MAO enzymes in vitro [170].

PET Studies PM-PBB3

A PET investigation of [¹⁸F]PM-PBB3 (Figure 6c) PET in tauopathy model mice demonstrated significantly increased retention in cortical areas, hippocampus, and striatum [168,170]. There was rapid initial uptake of [¹⁸F]PM-PBB3 (Figure 6c) in brain of the rTg4510 mice, [¹⁸F]PBB3 (Figure 6b) with a peak radioactivity 1.4 fold higher than for [¹⁸F]PBB3 (Figure 6b, 2-((1*E*,3*E*)-4-(2-[¹⁸F]fluoro)-6-(methylamino)pyridin-3-yl)buta-1,3-dien-1-yl)benzo[d]thiazol-6-ol); the new tracer also had greater metabolic stability compared with its predecessor [170]. Initial conference reports of [¹⁸F]PM-PBB3 (Figure 6c) PET in humans showed a greater signal-to-background ratio in parametric images compared with [¹¹C]PBB3 (Figure 6a) [171]. As opposed to [¹¹C]PBB3 (Figure 6a), there was no sign of off-target binding in basal ganglia and thalamus; while there was no sign of binding to MAO, [¹⁸F]PM-PBB3 (Figure 6c) had more distinct binding in the choroid plexus. On the other hand, [¹⁸F]PM-PBB3 (Figure 6c) showed high cortical retention in AD patients, matching the regions with hypometabolism to [¹⁸F]FDG-PET, and a significant positive correlation between cognitive dysfunction (MMSE score) and tracer retention and in all cortical regions except for occipital lobe [79]. Several studies concur in showing that [¹⁸F]PM-PBB3 (Figure 6c) PET differentiates AD cases from healthy controls with Cohen's *d* in the range of two–three in various culprit brain regions (Table 1).

2.6. Pyrrolo-Pyridineisoquinolineamines

2.6.1. [¹⁸F]MK-6240

A screening process yielded 6-[¹⁸F]fluoro-3-(1*H*-pyrrolo[2,3-*c*]pyridin-1-yl) isoquinolin-5-amine (Figure 7a, [¹⁸F]MK-6240) [172]. The tracer showed low binding to MAO-B in molecular docking studies [58,70]. Integrated molecular modeling studies showed that MK6240, similar to T807, has specific binding to site 1 of the tau fibrils, with a preference for core sites over surface sites. [³H]MK-6240 showed high-affinity binding ($K_D = 0.4$ nM) to NFT aggregates, with little sign of off-target binding [172]. The B_{max}/K_D ratio was twice that of [³H]AV-1451, predicting more sensitive detection of NFTs. AD brain sections showed [³H]MK6240 binding in gray matter regions comparable with the NFT staining pattern, which was displaceable by T808. [³H]MK-6240 had no specific binding to subcortical regions of human AD brain slices and did not bind to the entorhinal cortex and hippocampus of the non-AD brain [173]. Saturation binding assays with [³H]MK-6240 showed a K_D of 0.32 nM and B_{max} of 59 pmol/g in the temporal cortex from AD patients, versus a K_D of 0.15 nM and B_{max} of 155 pmol/g in the parietal cortex [174]. Autoradiography of entorhinal and temporal brain sections of AD patients showed strong off-target binding of [¹⁸F]MK-6240 (Figure 7a) to melanin and neuromelanin-containing cells [175].

[¹⁸F]MK-6240 (Figure 7a) PET in rhesus monkeys showed favorable brain kinetics and rapid attainment of a homogeneous brain distribution without labeling of the white matter [172,173]. Microdoses of the tracer proved to be safe in human PET studies [176]. Initial [¹⁸F]MK-6240 (Figure 7a) PET studies showed DVR values > 4 in the AD cortex, which indicates a high affinity to NFTs in vivo accompanied by a low non-displaceable signal [177]. DVR and SUV_r values were stable at 90 min after injection, and without off-target binding to the basal ganglia, non-target cortical regions, and choroid plexus. However, the tracer showed off-target binding in the substantia nigra, meninges, ethmoid sinus, and clivus bone, all relative to the pons and inferior cerebellum reference regions. The binding pattern of [¹⁸F]MK-6240 (Figure 7a) in target areas of A β + patients without dementia and AD patients correlated with Braak staging of NFT accumulation [85,177]. The peak SUV of [¹⁸F]MK-6240 (Figure 7a) was three–five, indicating high uptake, and the

SUVr was about one throughout HC brains versus two–four in NFT-rich regions of AD patients at 60–90 min after tracer injection [178]. Across all subjects, the tracer had adequate test–retest variabilities for various endpoints in NFT-rich brain areas [179].

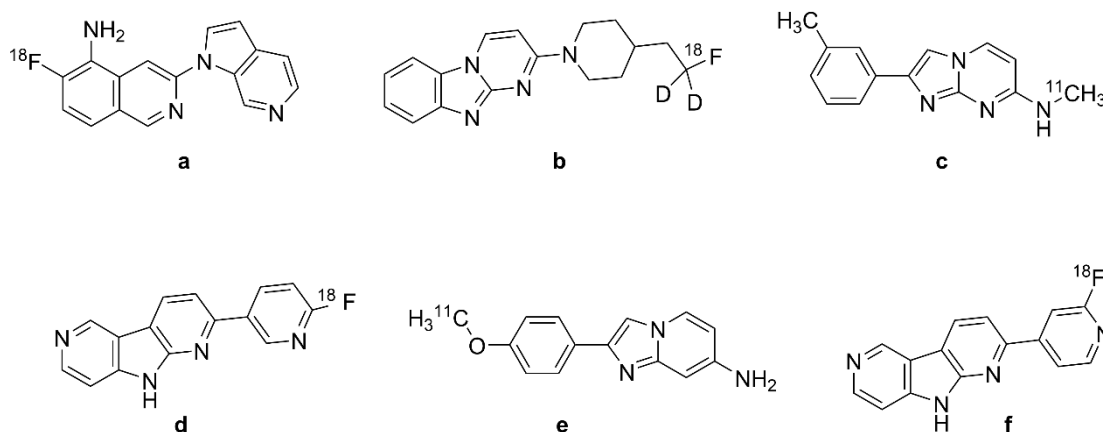


Figure 7. Chemical structures of selected second-generation tau PET radiotracers. (a): [^{18}F]MK-6240, (b): [^{18}F]GTP1, (c): [^{11}C]RO-643 or [^{11}C]RO-6931643, (d): [^{18}F]RO-948 or [^{18}F]RO-6958948, (e): [^{11}C]RO-963 or [^{11}C]RO-6924963, (f): [^{18}F]PI-2620.

A comparison with [^{18}F]flortaucipir PET (Figure 5a) showed that [^{18}F]MK-6240 (Figure 7a) had a two-fold higher dynamic range of SUVr values ($\text{SUVr}_{\text{max}} - \text{SUVr}_{\text{min}}$) in AD patients across Braak stages, a property that predicts greater sensitivity for early detection and distinguishing small changes in the rate of AD progression [180]. In that study, [^{18}F]MK-6240 (Figure 7a) SUVr values also correlated well with MR-based Braak staging. Cohen’s *d* values for discrimination of AD and HC groups are in the range of two–four across several studies (Table 1).

2.6.2. [^{18}F]GTP1

Although [^{18}F]T808 (Figure 5b) had comparable pharmacokinetics to [^{18}F]AV-1451 (Figure 5a), the latter tracer was selected for further evaluation due to the substantial *in vivo* defluorination of [^{18}F]T808 (Figure 5b) and accumulation of [^{18}F]fluoride in the bones of mice [163]. Isotopic substitution of hydrogen by deuterium on the carbon carrying [^{18}F] yielded [^{18}F]GTP1 (Figure 7b, Genentech Tau Probe 1), an analogue of [^{18}F]T808 (Figure 5b) with reduced defluorination in mice, rhesus monkeys, and humans [181,182]. *In vitro* studies have shown high selectivity and affinity of [^{18}F]GTP1 (Figure 7b) for tau aggregates ($K_D = 11$ nM and $B_{\text{max}}/K_D = 12 - 100$), while competitive binding assays with GTP1 against [^{18}F]AV-1451 (Figure 5a) in tau-positive tissues indicated a K_i of 22 nM [181]. Initial conference reports indicated no binding of [^{18}F]GTP1 (Figure 7b) to $A\beta$ and MAO-B [181,182].

Cross-sectional [^{18}F]GTP1 (Figure 7b) PET studies in AD patients showed elevated cortical binding in the suspect areas of tau pathology [181,183]. [^{18}F]GTP1 (Figure 7b) binding in the temporal lobe correlated with memory deficits and AD severity [183], and the tracer could successfully differentiate AD and HC groups [181,184], with Cohen’s *d* values in the range of one–two (Table 1).

2.6.3. [^{11}C]RO6931643, [^{18}F]RO6958948, and [^{11}C]RO6924963

In the optimization process of T807 and T808, researchers screened 550 derivatives, among which three compounds could displace [^3H]T808 binding in human AD brain sections with high affinity: RO6958948 (RO-948; IC_{50} 19 nM), RO6924963 (RO-963; IC_{50} 6 nM), and RO6931643 (RO-643; IC_{50} 10 nM) [185] (Table 1, Figure 7). The tritium-labeled tracers did not bind in AD brain sections lacking tau pathology, and the unlabeled compounds failed to displace [^3H]florbetapir binding to $A\beta$ in AD tissue sections. RO948 showed tau-to- $A\beta$ selectivity exceeding 500. These three tracers did not exhibit specific binding in

brain sections from non-AD tauopathy patients. The compounds were amenable to labeling with [^{11}C] and [^{18}F]. The three tracers showed no affinity for MAO-A or MAO-B, or other off-target binding sites [185,186].

Initial PET studies of all three tracers conducted in baboons demonstrated appropriate tracer kinetics with peak SUV = 1.2–2.0 within minutes after tracer administration and SUV = 0.5 at 60 min after injection, indicating slow washout, especially for RO963 [185]. The first human PET study of A β + AD patients showed peak SUV values of 3.0, 1.5, and 3.5 in the temporal lobe for [^{11}C]RO-963 (Figure 7e, 2-(4-[^{11}C]methoxy)phenyl)imidazo[1,2-a]pyridine-7-amine), [^{11}C]RO-643 (Figure 7c, *N*-[^{11}C]methyl-2-(*m*-tolyl)imidazo[1,2-a]pyrimidin-7-amine), and [^{18}F]RO-948 (Figure 7d, 2-(6-([^{18}F]fluoro-)pyridine-3-yl)-9*H*-pyrrolo [2,3-*b*:4,5-*c'*]dipyridine), respectively [89]. As well as having the greatest uptake, [^{18}F]RO-948 (Figure 7d) had the fastest washout from the brain. [^{11}C]RO-963 (Figure 7e) was not pursued due to its slow washout, indicative of higher nonspecific binding. Overall, [^{18}F]RO-948 (Figure 7d) showed better binding characteristics than [^{11}C]RO-643 (Figure 7c), with better uptake between regions expected to have higher tau accumulation. Indeed, [^{18}F]RO-948 (Figure 7d) was highly discriminative between AD patients and HCs, and did not exhibit *in vivo* defluorination. Another [^{18}F]RO-948 (Figure 7d) PET study conducted on A β + and A β – AD patients demonstrated the absence of off-target binding in the basal ganglia, choroid plexus, thalamus, and white matter, but some retention in the substantia nigra, meninges and retina [186]. The calculated test–retest variability of SUV_r in AD patients was 4.6%, indicating good reproducibility. [^{18}F]RO-948 (Figure 7d) uptake during three hours of PET recordings conformed well to a reversible binding model. Cohen’s *d* for differentiation of AD from HC groups was in the range of two–three (Table 1).

2.7. Naphthyridine Derivatives or Janssen Series (JNJ)

2.7.1. [^{18}F]JNJ-311

The ground scaffolds of the Janssen tau series are presented in Figure 8a,b. [^{18}F]JNJ-64349311 (Figure 8c, [^{18}F]JNJ-311, 6-[^{18}F]fluoro-*N*-(2-methyl-4-pyridinyl)-1,5-naphthyridin-2-amine) is a 1,5-naphthyridine derivative discovered through the mini-HTS analysis of more than 4000 candidate molecules [187]. The basis of this selection was derived from shape similarity to known selective ligands for tau aggregates, which led to the identification of *N*-(6-methylpyridin-2-yl)quinolin-2-amine. Radiofluorination yielded a ligand with high affinity and selectivity for tau (tau K_i = 8 nM, versus A β K_i > 4400) and no binding to MAO (Table 1).

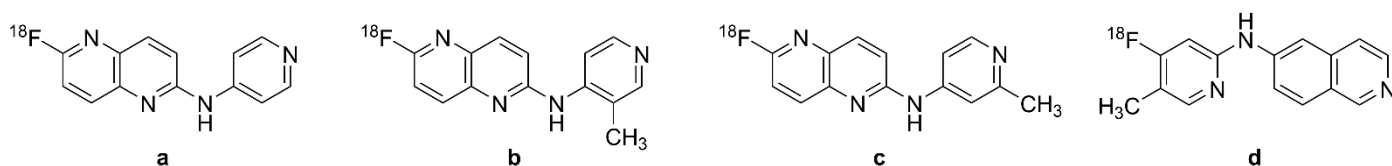


Figure 8. Chemical structures of selected tau PET radiotracers of the Janssen (JNJ) family. (a,b): 6-[^{18}F]fluoro-1,5-naphthyridine derivatives, (c): [^{18}F]JNJ-311 or [^{18}F]JNJ-64349311, (d): [^{18}F]JNJ-067 or [^{18}F]JNJ-64326067.

[^{18}F]JNJ-311 (Figure 8c) has suitable brain uptake and washout in mice, and its polar radiometabolites were present only in the plasma compartment [188]. *In vitro* competition assays of AD brain samples showed displaceable binding to tau aggregates. PET studies in monkeys indicated good penetrance and fast washout, and were without signs of defluorination during a 120 min scan. At the time of writing, there are not tests of this ligand in humans.

2.7.2. JNJ-067

[^{18}F]JNJ-64326067 ([^{18}F]JNJ-067, *N*-(4-[^{18}F]fluoro-5-methylpyridin-2-yl)isoquinoline-6-amine, Figure 8d) is a derivative of [^{18}F]JNJ-311 (Figure 8c) with high binding affinity

to tau ($K_i = 2.4$ nM) and low off-target binding to $A\beta$ ($K_i = 3.2$ μ M), MAO enzymes, and other targets assessed in a standard binding profile [189]. An evaluation of [3 H]JNJ-067 in an AD brain section showed $K_D = 0.9$ nM and $B_{max} = 7.5$ nmol/g, which was comparable to findings with [3 H]T808 ($K_D = 4.9$ nM and $B_{max} = 6.3$ nmol/g).

Rat and monkey PET studies with [18 F]JNJ-067 (Figure 8d) showed high initial brain uptake and rapid washout from non-target regions, and no evidence of defluorination at 120 min post-injection [189]. Clinical studies of [18 F]JNJ-067 (Figure 8d) showed tracer retention in areas of suspected pathology in [11 C]PIB (Figure 1f) positive AD and MCI patients, but no such retention in HCs [190]. Cohen's *d* for differentiation of AD and HC groups was in the range of one–two. There was some off-target binding of [18 F]JNJ-067 (Figure 8d) in the basal ganglia and white matter. The SUV/DVR ratios ranged from 1.2 to 2.18 in the frontal cortex and 1.21 to 3.09 in the temporal cortex of AD patients, which exceeded the range in healthy controls [90]. However, one AD patient in that study showed no specific tracer signal.

2.8. [18 F]PI-2620

Due to its high affinity for tau deposits and lesser affinity for MAO-A compared with pyrido[4,3-*b*]indole-derived tracers (AV-1451 (Figure 5a), Figure 7), the pyrrolo[2,3-*b*:4,5-*c'*]dipyridine core structures of RO-948 served as the scaffold for some fluoropyridine regioisomers, among which PI-2620 was selected for further studies [191]. A molecular docking study [104] reported a weak interaction between [18 F]PI-2620 (Figure 7f, 2-(2-([18 F]fluoro-4-pyridinyl)-9*H*-pyrrolo(2,3-*b*:4,5-*c'*)dipyridine) and MAO-B *in vitro*. [18 F]PI-2620 (Figure 7f) bound to 3R, 4R, PHF, and K18 fibrils with IC_{50} values ranging from 3 to 20 nM. This encouraged clinical evaluation of [18 F]PI-2620 (Figure 7f) [191]. Autoradiography studies of AD brain homogenates revealed $IC_{50} = 1.8$ nM for [18 F]PI-2620 (Figure 7f) [192].

[18 F]PI-2620 (Figure 7f) PET showed good kinetics in the human brain, with low test–retest variability of the DVR and SUV endpoints [193]. Cohen's *d* for the discrimination between AD patient and HC groups was in the range of two–three in two of three PET studies (Table 1). Early conference reports of human [18 F]PI-2620 (Figure 7f) PET claimed no off-target binding in areas labeled with [18 F]AV-1451 (Figure 5a), e.g., choroid plexus and basal ganglia [194–197]. There was high binding of [18 F]PI-2620 (Figure 7f) in the substantia nigra and globus pallidus in PSP patients compared with HCs, implying binding to 4R tau filaments, but the binding was higher still in the cortex of AD patients; highest tracer retention in $A\beta+$ AD patients was in the posterior cingulate gyrus and temporoparietal areas.

The initial human studies of [18 F]PI-2620 (Figure 7f) showed robust brain uptake and fast washout from non-target areas such as basal ganglia and choroid plexus [93,197,198]. A [18 F]PI-2620 (Figure 7f) PET study in AD patients determined an appropriate scanning interval of 30–75 min for AD patients [199]. Enhanced tracer retention in AD subjects mostly occurred asymmetrically at the posterior cingulate gyrus, precuneus, parietal, and temporal lobes, with significantly higher DVR and SUVr when compared with HCs [93]. There was a significant correlation between cognitive impairment scores and neocortical tracer uptake. However, [18 F]PI-2620 (Figure 7f) retention was higher in older HCs [200].

A recent human [18 F]PI-2620 (Figure 7f) PET study of AD showed no off-target binding in the basal ganglia (i.e., MAO-B binding) in contrast to [18 F]THK-5351 (Figure 3g) and other first-generation tau tracers [123]. Increased binding in the frontotemporoparietal cortex was noted in $A\beta+$ MCI and AD patients, whereas $A\beta-$ patients showed no significant increase in [18 F]PI-2620 (Figure 7f) binding in the cortex, as opposed to the increases in [18 F]THK5351 (Figure 3g) binding in the same areas. However, one patient with $A\beta+$ AD showing major atrophy in the bilateral temporal cortex had no cortical increase in [18 F]PI-2620 (Figure 7f) binding despite elevated [18 F]THK-5351 (Figure 3g) binding. There was evidence for relatively high [18 F]PI-2620 (Figure 7f) uptake in vermis, which might also be a general property of second-generation tau PET tracers. Overall, clinical PET studies with

[^{18}F]PI-2620 (Figure 7f) showed relatively moderate sensitivity for the discrimination of AD and HC groups, with Cohen's d values around two (Table 1).

2.9. Radioiodinated Benzoimidazopyridine (BIP) Derivatives

Benzoimidazopyridine (BIP) derivatives are emerging tau tracers for PET and SPECT, notably [^{125}I]BIP-NMe₂ (Figure 9a, 7-[^{125}I]iodo-*N,N*-dimethylbenzo[4,5]imidazo[1,2-*a*]pyridin-3-amine), which is radioiodinated at the 7-position. Modifications of the 3-position in the BIP scaffold yielded [^{18}F]IBIPF1 (Figure 9b, *N*-(2-[^{18}F]fluoroethyl)-7-iodo-*N*-methylbenzo[4,5]imidazo[1,2-*a*]pyridin-3-amine) and [^{18}F]IBIPF2 (Figure 9c, *N*-(2-[^{18}F]fluoroethyl)-7-iodobenzo[4,5]imidazo[1,2-*a*]pyridin-3-amine) [201]. Since several PET radioligands such as [^{18}F]AV-1451 (Figure 5a) and [^{18}F]GTP1 (Figure 7b) also contain the 6,5,6-tricyclic scaffold found in [^{125}I]BIP-NMe₂ (Figure 9a), there is considerable basis for further radioiodinated modifications [202].

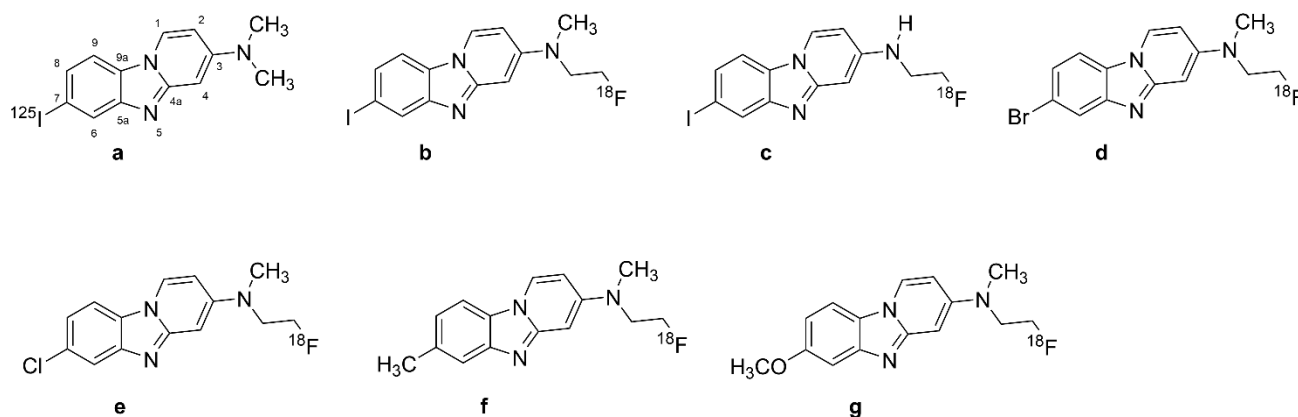


Figure 9. Chemical structures of benzimidazopyridine (BIP) tau radiotracers. (a): [^{125}I]BIP-NMe₂, (b): [^{18}F]IBIPF1, (c): [^{18}F]IBIPF2, (d): [^{18}F]Br-BIPF, (e): [^{18}F]Cl-BIPF, (f): [^{18}F]Me-BIPF, (g): [^{18}F]OMe-BIPF.

Introducing halogens, methoxy, or methyl groups to the 7-position of BIP scaffold resulted in various compounds, including [^{18}F]Br-BIPF (Figure 9d, 7-bromo-*N*-(2-[^{18}F]fluoroethyl)-*N*-methylbenzo[4,5]imidazo[1,2-*a*]pyridin-3-amine), [^{18}F]Cl-BIPF (Figure 9e, 7-chloro-*N*-(2-[^{18}F]fluoroethyl)-*N*-methylbenzo[4,5]imidazo[1,2-*a*]pyridin-3-amine), [^{18}F]Me-BIPF (Figure 9f, *N*-(2-[^{18}F]fluoroethyl)-*N*,7-dimethylbenzo[4,5]imidazo[1,2-*a*]pyridin-3-amine), and [^{18}F]OMe-BIPF (Figure 9g, *N*-(2-[^{18}F]fluoroethyl)-7-methoxy-*N*-methylbenzo[4,5]imidazo[1,2-*a*]pyridin-3-amine) [203].

Autoradiography studies have indicated the higher effect of modifications in the 3-position of the BIP scaffold on affinity to tau aggregates than modifications of the 7-position [202]. However, [^{18}F]Br-BIPF (Figure 9d), [^{18}F]Cl-BIPF (Figure 9e), [^{18}F]Me-BIPF (Figure 9f), and [^{18}F]OMe-BIPF (Figure 9g) have also shown appropriate binding to tau aggregates in AD brain sections [201,202]. [^{125}I]BIP-NMe₂ (Figure 9a, [^{125}I]7-iodo-3-dimethylaminopyrido[1,2- α]benzimidazole) had higher selectivity than other BIP derivatives, with a Tau/A β ratio of 33 [82]. The binding ratio of [^{125}I]BIP-NMe₂ (Figure 9a) in the gray matter of the temporal lobe compared with the frontal lobe was 12.9, and autoradiographic studies in AD brains show selectivity of [^{18}F]IBIPF1 (Figure 9b) and [^{18}F]IBIPF2 (Figure 9c) tau for aggregates compared with A β [204]. [^{18}F]IBIPF1 (Figure 9b) binding was absent in normal human temporal lobe sections.

[^{125}I]BIP-NMe₂ (Figure 9a) has shown favorable brain kinetics in healthy mice [205]. [^{18}F]IBIPF1 (Figure 9b) showed high initial uptake in mouse brains (6.2% ID/g at two min post-injection) and fast brain washout [206]. Biodistribution studies of [^{125}I]21 and [^{125}I]22 in normal mice likewise showed favorable pharmacokinetics, potentially superior to that of ([^{125}I]BIP-NMe₂, Figure 9a) [203]. Overall, this study represented two new scaffolds for developing further novel tau tracers, which remain to be studied in AD.

3. Discussion and Conclusions

The first successful tau tracer [^{18}F]FDDNP (Figure 1a) was an “accidental tau tracer”, having been first intended for detecting A β [48]; [^{18}F]FDDNP (Figure 1a) has roughly similar affinity for the two molecular targets [52,53] and thus represents the composite of two neurochemical pathologies in AD, despite its possibly lower sensitivity for A β [56]. Such discrepancies could reflect factors such as the type of A β or tau preparations used. While [^{18}F]FDDNP (Figure 1a) is still used for research purposes [207], more selective molecules, notably TAUVID ([^{18}F]flortaucipir, Figure 5a), are in clinical use for the diagnosis of AD. As we described above, neither is TAUVID entirely selective for tau aggregates, having a considerable affinity for MAO [125,147]. However, recent studies called into question the contributions of MAO binding to the [^{18}F]flortaucipir (Figure 5a) signals from cortical regions [208]. Other tau tracers intended for human PET studies bind to additional targets such as neuromelanin in nigrostriatal dopamine cells, i.e., [^{18}F]THK-5351 (Figure 3g), [^{18}F]flortaucipir (Figure 5a), and [^{18}F]MK-6240 (Figure 7a) [117,141,143,175]. Finally, the degree of lipophilicity of different tracers may contribute to white matter binding and signal-to-noise ratio [63].

To compare the fitness of different tau tracers to discriminate AD and HC groups, we focus on clinical PET studies reporting SUV or SUVr results, with a mean and standard deviation of the endpoint across one or more brain regions, thereby enabling us to calculate Cohen’s *d*. This may enable an objective judgment of the fitness of the various tau ligands for the specific task of identifying AD at an early disease stage, irrespective of their absolute pharmacological specificity for tau aggregates. Thus, [^{18}F]FDDNP (Figure 1a) yielded a Cohen’s *d* of about 2.3 in the frontal cortex, with lesser values in other cortical regions in mild AD, but a Cohen’s *d* of around 3 in a more severely affected patient group (Table 1). These large effect sizes indicate considerable fitness for correctly discriminating between the AD and the HC brain. We suppose that its relatively high retention in the frontal cortex reflects the confluence of amyloid and taupathologies. While not imparting definite knowledge about its biochemical nature, the tracer still serves admirably for identifying “net AD pathology”.

Of the various classes of compounds discussed herein, only a few outperformed [^{18}F]FDDNP (Figure 1a) for discrimination between AD and HC groups. For example, [^{18}F]THK5105 (Figure 3b) had a Cohen’s *d* as high as 3.6 in the inferior temporal lobe [63], whereas [^{18}F]THK5117 (Figure 3d) had a Cohen’s *d* of 3 in the neocortex and Cohen’s *d* of 2.7 in the inferior temporal lobe [64]. In other words, these tracers can discriminate the two populations with almost perfect fidelity. However, the THK series has cross-reactivity with MAO [125–128]. Since astrocytes express MAO-B [209], and since AD and other neurodegenerative diseases are associated with astrocytosis [204], the THK signal may well depict the composite of tau and MAO, again raising the prospect of “net AD pathology”, in analogy to [^{18}F]FDDNP (Figure 1a) depicting the composite of tau and A β . After treatment of AD patients with MAO-B blockers, PET studies with [^{18}F]THK5351 (Figure 3g) showed 50% lower specific binding, which was later confirmed by tissue autoradiography [126,210]. This presents another instance of a fortuitous co-distribution of two targets, namely tau and MAO-B in AD patients, reflecting distinct aspects of AD pathology.

We conclude with some notes on the limitations of the present literature, and the implicit requirements for improved study design. Thus, the diagnosis of AD in most of the cited studies arose from clinical examination and questionnaires; unsurprisingly, there are very few reports with confirmation of PET results by post mortem histopathological examination, i.e., [128]. We note the generally low group size in most of the cited PET studies, which ranges from about 10 to 50; such group sizes may not capture disease heterogeneity or subtle disease progression, and may inadvertently have resulted in selection bias, with preferential recruitment of AD patients with more advanced disease. Finally, this is a narrative review, which by no means meets the criteria of a systematic review. Thus, we do not include all of the relevant literature, but rather a selection of the papers that enable comparison of Cohen’s *d* for discriminating AD and HC groups.

Author Contributions: Conceptualization, Z.M. and P.C.; methodology, P.C.; investigation, Z.M., H.A., J.M. and P.C.; writing—original draft preparation, Z.M., H.A., J.M. and P.C.; writing—review and editing, P.C. All authors have read and agreed to the published version of the manuscript.

Funding: This research received no external funding.

Institutional Review Board Statement: Not applicable.

Informed Consent Statement: Not applicable.

Data Availability Statement: Not applicable.

Acknowledgments: This project was supported by the Swiss National Science Foundation grant number 320030-204978 (P.C.).

Conflicts of Interest: The authors declare no conflict of interest.

Abbreviations

Compound, Term, Acronym	Figure	Names, Synonyms
Astemizole	Figure 4b	hismanal; histaminos; paralergin; loaridal; retolen; astemison; 1-[(4-fluorophenyl)methyl]-N-[1-[2-(4-methoxyphenyl)ethyl]piperidin-4-yl]benzimidazol-2-amine; CAS-RN: 68844-77-9
AV-1451		T807; 7-(6-fluoropyridin-3-yl)-5H-pyrido[4,3-b]indole; CAS RN: 1415379-56-4
[¹⁸ F]AV1451	Figure 5a	[¹⁸ F]flortaucipir; [¹⁸ F]T807; [¹⁸ F]LY 3191748; [¹⁸ F]AV-1451; 7-(6-[¹⁸ F]fluoro-pyridin-3-yl)-5H-pyrido[4,3-b]indole; CAS RN: 1522051-90-6
BBB		blood brain barrier
BF-158	Figure 2a	N-methyl-4-(quinolin-2-yl)aniline; CAS RN: 682763-67-3
[¹¹ C]BF-158	Figure 2e	N-[¹¹ C]methyl-4-(quinolin-2-yl)aniline
BF-168	Figure 2c	(E)-4-(2-(6-(2-fluoroethoxy)benzo[d]oxazol-2-yl)vinyl)-N-methylaniline; CAS RN: 634911-47-0
BF-170	Figure 2b	2-(4-aminophenyl)quinoline
[¹¹ C]BF-227	Figure 2g	(E)-5-(2-(6-(2-fluoroethoxy)benzo[d]oxazol-2-yl)vinyl)-N-methyl-N-[¹¹ C]methyl-thiazol-2-amine
BF-242	Figure 2d	THK-523; 4-[6-(2-fluoroethoxy)-2-quinoliny]aniline; CAS RN: 1573029-17-0
[¹⁸ F]BF-242	Figure 2f	[¹⁸ F]THK-523; 4-[6-(2-[¹⁸ F]fluoroethoxy)-2-quinoliny]aniline
BIP		benzimidazopyridine
[¹²⁵ I]BIP-NMe ₂	Figure 9a	7-[¹²⁵ I]iodo-N,N-dimethylbenzo[4,5]imidazo[1,2-a]pyridin-3-amine
[¹⁸ F]Br-BIPF	Figure 9d	7-bromo-N-(2-[¹⁸ F]fluoroethyl)-N-methylbenzo[4,5]imidazo[1,2-a]pyridin-3-amine
[¹⁸ F]Cl-BIPF	Figure 9e	7-chloro-N-(2-[¹⁸ F]fluoroethyl)-N-methylbenzo[4,5]imidazo[1,2-a]pyridin-3-amine
[¹⁸ F]IBIPF1	Figure 9b	N-(2-[¹⁸ F]fluoroethyl)-7-iodo-N-methylbenzo[4,5]imidazo[1,2-a]pyridin-3-amine
[¹⁸ F]IBIPF2	Figure 9c	N-(2-[¹⁸ F]fluoroethyl)-7-iodobenzo[4,5]imidazo[1,2-a]pyridin-3-amine
[¹⁸ F]Me-BIPF	Figure 9f	N-(2-[¹⁸ F]fluoroethyl)-N,7-dimethylbenzo[4,5]imidazo[1,2-a]pyridin-3-amine
[¹⁸ F]OMe-BIPF	Figure 9g	N-(2-[¹⁸ F]fluoroethyl)-7-methoxy-N-methylbenzo[4,5]imidazo[1,2-a]pyridin-3-amine
DDNP	Figure 1b	1,1-dicyano-2-[6-(dimethylamino)naphthalene-2-yl]propene; 2-[1-[1-(dimethylamino)naphthalen-2-yl]ethylidene]propanedinitrile; CAS RN: 178385-38-1
FDDNP		FDDNP; DMFEAN 2-[1-[6-[2-fluoroethyl(methyl)amino]naphthalen-2-yl]ethylidene]propanedinitrile CAS RN: 590365-47-2
[¹⁸ F]FDDNP	Figure 1a	Fddnp F-18; [¹⁸ F]JUNII-3]JP3286H 2-[1-[6-[2-[¹⁸ F]fluoroethyl(methyl)amino]naphthalen-2-yl]ethylidene]propanedinitrile; CAS RN: 259738-99-3
FENE	Figure 1d	1-(6-[(2-fluoroethyl)(methyl)amino]naphthalen-2-yl)ethanone CAS RN: 1260894-66-3

[¹⁸ F]FENE flortaucipir	Figure 1e	1-(6-[(2-[¹⁸ F]fluoroethyl)(methyl)amino]naphthalen-2-yl)ethanone T807; 7-(6-fluoropyridin-3-yl)-5H-pyrido[4,3- <i>b</i>]indole; CAS RN: 1415379-56-4 [¹⁸ F]T807; [¹⁸ F]LY 3191748; [¹⁸ F]AV-1451;
[¹⁸ F]flortaucipir	Figure 5a	7-(6-[¹⁸ F]fluoro-pyridin-3-yl)-5H-pyrido[4,3- <i>b</i>]indole; CAS RN: 1522051-90-6
[¹⁸ F]GTP1	Figure 7b	Genetech Tau Probe 1
[¹⁸ F]JNJ-64326067	Figure 8d	[¹⁸ F]JNJ067; <i>N</i> -(4-[¹⁸ F]Fluoro-5-methylpyridin-2-yl)isoquinolin-6-amine <i>N</i> -[4-[¹⁸ F]fluoro-5-methyl-2-pyridinyl]-6-isoquinolinamine, CAS RN: 2173357-42-9
[¹⁸ F]JNJ-64349311	Figure 8c	[¹⁸ F]JNJ311; [¹⁸ F]JNJ 311; 6-[¹⁸ F]fluoro- <i>N</i> -(2-methyl-4-pyridinyl)-1,5-naphthyridin-2-amine; CAS RN: 2121497-78-5
[¹⁸ F]JNJ (Co. No. 2)	Figure 8b	6-[¹⁸ F]fluoro- <i>N</i> -(3-methyl-4-pyridinyl)-1,5-naphthyridin-2-amine CAS RN: 2121497-79-6; Moechars, D.W.E. et al. <i>AU Pat.</i> 2017216212
[¹⁸ F]JNJ (Co. Nr. 3)	Figure 8a	6-[¹⁸ F]fluoro- <i>N</i> -4-pyridinyl-1,5-naphthyridin-2-amine CAS RN: 2121497-80-9, Moechars, D.W.E. et al. <i>AU Pat.</i> 2017216212 prevacid; bamalite; monolitus; ogastro; agopton;
Lansoprazole	Figure 4a	2-[[3-methyl-4-(2,2,2-trifluoroethoxy)pyridin-2-yl]methylsulfinyl]-1 <i>H</i> -benzimidazole CAS RN: 103577-45-3
MK-6240		6-fluoro-3-(1 <i>H</i> -pyrrolo[2,3- <i>c</i>]pyridin-1-yl)isoquinolin-5-amine CAS RN: 1841078-87-2
[¹⁸ F]MK-6240	Figure 7a	[¹⁸ F]MNI-946; 6-[¹⁸ F]fluoro-3-(1 <i>H</i> -pyrrolo[2,3- <i>c</i>]pyridin-1-yl)isoquinolin-5-amine
NML	Figure 4c	<i>N</i> -Methyl-lansoprazole; 1-methyl-2-[[3-methyl-4-(2,2,2-trifluoroethoxy)pyridin-2-yl]methylsulfinyl]benzimidazole
[¹¹ C]NML	Figure 4d	[¹¹ C]- <i>N</i> -Methyl-lansoprazole; 1-[¹¹ C]methyl-2-[[3-methyl-4-(2,2,2-trifluoroethoxy)pyridin-2-yl]methylsulfinyl]benzimidazole
[¹⁸ F]NML	Figure 4e	[¹⁸ F]- <i>N</i> -Methyl-lansoprazole; 2-(((4-(2,2-difluoro-2-[¹⁸ F]fluoro-ethoxy)-3-methylpyridin-2-yl)methyl)sulfinyl)-1-methyl-1 <i>H</i> -benzo[<i>d</i>]imidazole
PI-2620		2-(2-[¹⁸ F]fluoro-pyridin-4-yl)-9 <i>H</i> -pyrrolo[2,3- <i>b</i> :4,5- <i>c'</i>]dipyridine [¹⁸ F]MNI-960; 11-(2-[¹⁸ F]fluoranylpyridin-4-yl)-4,8,10-triazatricyclo[7.4.0.0 ^{2,7}]trideca-1(9),2(7), 3,5,10,12-hexaene; 2-(2-([¹⁸ F]fluoro-4-pyridinyl)-9 <i>H</i> -pyrrolo(2,3- <i>b</i> :4,5- <i>c'</i>)dipyridine; CAS RN: 2173353-61-0
[¹⁸ F]PI-2620	Figure 7f	pyridinyl-butadienyl-benzothiazole
PBB		2-[(1 <i>E</i> ,3 <i>E</i>)-4-[6-(methylamino)pyridin-3-yl]buta-1,3-dienyl]-1,3-benzothiazol-6-ol CAS RN: 1565796-97-5
PBB3		2-[(1 <i>E</i> ,3 <i>E</i>)-4-[6-[¹¹ C]methylamino)pyridin-3-yl]buta-1,3-dienyl]-1,3-benzothiazol-6-ol; CAS RN: 1565797-40-1
[¹¹ C]PBB3	Figure 6a	2-((1 <i>E</i> ,3 <i>E</i>)-4-(2-[¹⁸ F]fluoro)-6-(methylamino)pyridin-3-yl)buta-1,3-dien-1-yl)benzo[<i>d</i>]thiazol-6-ol
[¹⁸ F]PBB3	Figure 6b	6-OH-BTA-1; Pittsburgh Compound B
PIB		2-[4-(methylamino)phenyl]-6-benzothiazolol CAS RN: 566169-93-5
[¹¹ C]PIB	Figure 1f	[<i>N</i> -methyl- ¹¹ C]-6-OH-BTA-1, CAS RN: 566170-04-5
PM-PBB3		APN-1607; 1-fluoro-3-((2-((1 <i>E</i> ,3 <i>E</i>)-4-(6-(methylamino)pyridin-3-yl)buta-1,3-dien-1-yl)benzo[<i>d</i>]thiazol-6-yl)oxy)propan-2-ol [¹⁸ F]APN-1607; [¹⁸ F]MNI-958; 1-[¹⁸ F]fluoro-3-((2-((1 <i>E</i> ,3 <i>E</i>)-4-(6-(methylamino)pyridin-3-yl)buta-1,3-dien-1-yl)benzo[<i>d</i>]thiazol-6-yl)oxy)propan-2-ol, CAS RN 1565797-57-0
[¹⁸ F]PM-PBB3	Figure 6c	Ro963; 2-(4-methoxyphenyl)imidazo[1,2- <i>a</i>]pyridin-7-amine
RO-6924963		[¹¹ C]R0963; 2-(4-(¹¹ C)methoxy)phenyl)imidazo[1,2- <i>a</i>]pyridin-7-amine
[¹¹ C]RO-6931643	Figure 7e	Ro643; <i>N</i> -methyl-2-(<i>m</i> -tolyl)imidazo[1,2- <i>a</i>]pyrimidin-7-amine
[¹¹ C]RO-6931643	Figure 7c	[¹¹ C]R0643; <i>N</i> -[¹¹ C]methyl-2-(<i>m</i> -tolyl)imidazo[1,2- <i>a</i>]pyrimidin-7-amine
RO-6958948		RO-948; 2-(6-fluoro-pyridin-3-yl)-9 <i>H</i> -pyrrolo[2,3- <i>b</i> :4,5- <i>c'</i>]dipyridine
[¹⁸ F]RO-6958948	Figure 7d	[¹⁸ F]R0948; 2-(6-([¹⁸ F]fluoro-)pyridin-3-yl)-9 <i>H</i> -pyrrolo[2,3- <i>b</i> :4,5- <i>c'</i>]dipyridine
[¹⁸ F]S16	Figure 3i	(<i>S</i>)-1-(4-(6-(dimethylamino)quinoxalin-2-yl)phenoxy)-3-fluoropropan-2-ol
T807		flortaucipir; LY 3191748; AV-1451
[¹⁸ F]T807	Figure 5a	[¹⁸ F]flortaucipir; [¹⁸ F]LY 3191748; [¹⁸ F]AV-1451
T808		AV-680; 2-[4-(2-Fluoroethyl)-1-piperidinyl]pyrimido[1,2- <i>a</i>]benzimidazole CAS RN: 1320211-61-7

[¹⁸ F]T808 Tauvid	Figure 5b Figure 5a	[¹⁸ F]AV-680; 2-[4-(2-[¹⁸ F]Fluoroethyl)-1-piperidinyl]pyrimido[1,2-a]benzimidazole 18F-AV-1451, 18F-T807, Flortaucipir F-18 4-[6-(2-fluoroethoxy)-2-quinolinyl]aniline
THK-523	Figure 2d	2-(4-Aminophenyl)-6-(2-(fluoroethoxy))quinoline; CAS RN: 1573029-17-0
[¹⁸ F]THK-523	Figure 2f	4-[6-(2-[¹⁸ F]fluoroethoxy)-2-quinolinyl]aniline 2-(4-Aminophenyl)-6-(2-([¹⁸ F]fluoroethoxy))quinoline
THK-951		2-[(N-Methyl-4-amino)phenyl]quinolin-7-ol
[¹¹ C]THK-951	Figure 3a	2-(4-([¹¹ C]methyl)-amino)phenyl]quinolin-7-ol
THK-5105		1-((2-(4-(dimethylamino)phenyl)quinolin-6-yl)oxy)-3-fluoropropan-2-ol
[¹⁸ F]THK-5105	Figure 3b	1-((2-(4-(dimethylamino)phenyl)quinolin-6-yl)oxy)-3-[¹⁸ F]fluoropropan-2-ol
[¹⁸ F]THK-5116	Figure 3c	1-((2-(4-aminophenyl)quinolin-6-yl)oxy)-3-[¹⁸ F]fluoropropan-2-ol
THK-5117		1-fluoro-3-[2-[4-(methylamino)phenyl]quinolin-6-yl]oxypropan-2-ol CAS RN: 1374107-54-6
[¹⁸ F]THK-5117	Figure 3d	1-[¹⁸ F]fluoro-3-[2-[4-(methylamino)phenyl]quinolin-6-yl]oxypropan-2-ol
THK-5317		6-((3-fluoro-2-hydroxy)propoxy)-2-(4-methylaminophenyl)quinoline
[¹⁸ F]THK-5317	Figure 3f	6-((3-[¹⁸ F]fluoro-2-hydroxy)propoxy)-2-(4-methylaminophenyl)quinoline
THK-5351		GE-216; (2R)-1-fluoro-3-[2-[6-(methylamino)pyridin-3-yl]quinolin-6-yl]oxypropan-2-ol CAS RN: 2101218-44-2
[¹¹ C]THK-5351	Figure 3h	(2R)-1-fluoro-3-[2-[6-([¹¹ C]methylamino)pyridin-3-yl]quinolin-6-yl]oxypropan-2-ol
[¹⁸ F]THK-5351	Figure 3g	[¹⁸ F]GE-216; (2R)-1-[¹⁸ F]fluoro-3-[2-[6-(methylamino)pyridin-3-yl]quinolin-6-yl]oxypropan-2-ol

References

- Kowall, N.W.; Kosik, K.S. Axonal disruption and aberrant localization of tau protein characterize the neuropil pathology of Alzheimer's disease. *Ann. Neurol.* **1987**, *22*, 639–643. [[CrossRef](#)] [[PubMed](#)]
- Dickson, D.W.; Kouri, N.; Murray, M.E.; Josephs, K.A. Neuropathology of frontotemporal lobar degeneration-tau (FTLD-tau). *J. Mol. Neurosci.* **2011**, *45*, 384–389.
- Villemagne, V.L.; Furumoto, S.; Fodero-Tavoletti, M.; Harada, R.; Mulligan, R.S.; Kudo, Y.; Masters, C.L.; Yanai, K.; Rowe, C.C.; Okamura, N. The challenges of tau imaging. *Future Neurol.* **2012**, *7*, 409–421. [[CrossRef](#)]
- Villemagne, V.L.; Doré, V.; Burnham, S.C.; Masters, C.L.; Rowe, C.C. Imaging tau and amyloid- β proteinopathies in Alzheimer disease and other conditions. *Nat. Rev. Neurol.* **2018**, *14*, 225–236. [[CrossRef](#)] [[PubMed](#)]
- Goedert, M.; Spillantini, M.G. A century of Alzheimer's disease. *Science* **2006**, *314*, 777–781. [[CrossRef](#)]
- Perl, D.P. Neuropathology of Alzheimer's disease. *Mt. Sinai J. Med.* **2010**, *77*, 32–42. [[CrossRef](#)]
- Mohorko, N.; Bresjanac, M. Tau protein and human tauopathies: An overview. *Slov. Med. J.* **2008**, *77*.
- Goedert, M.; Spillantini, M.; Cairns, N.; Crowther, R. Tau proteins of Alzheimer paired helical filaments: Abnormal phosphorylation of all six brain isoforms. *Neuron* **1992**, *8*, 159–168. [[CrossRef](#)]
- Crowther, R. Straight and paired helical filaments in Alzheimer disease have a common structural unit. *Proc. Natl. Acad. Sci. USA* **1991**, *88*, 2288–2292. [[CrossRef](#)]
- Delacourte, A. Tauopathies: Recent insights into old diseases. *Folia Neuropathol.* **2005**, *43*, 244–257.
- Braak, H.; Braak, E. Neuropathological staging of Alzheimer-related changes. *Acta Neuropathol.* **1991**, *82*, 239–259. [[CrossRef](#)] [[PubMed](#)]
- Serrano-Pozo, A.; Frosch, M.P.; Masliah, E.; Hyman, B.T. Neuropathological alterations in Alzheimer disease. *Cold Spring Harb. Perspect. Med.* **2011**, *1*, a006189. [[CrossRef](#)] [[PubMed](#)]
- Bobinski, M.; Wegiel, J.; Wisniewski, H.M.; Tarnawski, M.; Bobinski, M.; Reisberg, B.; De Leon, M.J.; Miller, D.C. Neurofibrillary pathology—Correlation with hippocampal formation atrophy in Alzheimer disease. *Neurobiol. Aging* **1996**, *17*, 909–919. [[PubMed](#)]
- Harrison, T.M.; La Joie, R.; Maass, A.; Baker, S.L.; Bs, K.S.; Fenton, L.; Bs, T.J.M.; Edwards, L.; Pham, J.; Miller, B.L.; et al. Longitudinal tau accumulation and atrophy in aging and Alzheimer disease. *Ann. Neurol.* **2019**, *85*, 229–240. [[CrossRef](#)] [[PubMed](#)]
- Arriagada, P.V.; Growdon, J.H.; Hedley-Whyte, E.T.; Hyman, B.T. Neurofibrillary tangles but not senile plaques parallel duration and severity of Alzheimer's disease. *Neurology* **1992**, *42*, 631–639. [[CrossRef](#)]
- Delaere, P.; Duyckaerts, C.; Brion, J.P.; Poulain, V.; Hauw, J.-J. Tau, paired helical filaments and amyloid in the neocortex: A morphometric study of 15 cases with graded intellectual status in aging and senile dementia of Alzheimer type. *Acta Neuropathol.* **1989**, *77*, 645–653. [[CrossRef](#)]
- Delaere, P.; Duyckaerts, C.; Masters, C.; Beyreuther, K.; Piette, F.; Hauw, J. Large amounts of neocortical β A4 deposits without neuritic plaques nor tangles in a psychometrically assessed, non-demented person. *Neurosci. Lett.* **1990**, *116*, 87–93. [[CrossRef](#)] [[PubMed](#)]
- Rowe, C.C.; Ackerman, U.; Browne, W.; Mulligan, R.; Pike, K.L.; O'Keefe, G.; Tochon-Danguy, H.; Chan, G.; Berlangieri, S.U.; Jones, G.; et al. Imaging of amyloid β in Alzheimer's disease with ¹⁸F-BAY94-9172, a novel PET tracer: Proof of mechanism. *Lancet Neurol.* **2008**, *7*, 129–135. [[CrossRef](#)]

19. Katzman, R.; Terry, R.; DeTeresa, R.; Brown, T.; Davies, P.; Fuld, P.; Renbing, X.; Peck, A. Clinical, pathological, and neurochemical changes in dementia: A subgroup with preserved mental status and numerous neocortical plaques. *Ann. Neurol.* **1988**, *23*, 138–144. [[CrossRef](#)]
20. Shoghi-Jadid, K.; Small, G.W.; Agdeppa, E.D.; Kepe, V.; Ercoli, L.M.; Siddarth, P.; Read, S.; Satyamurthy, N.; Petric, A.; Huang, S.C.; et al. Localization of neurofibrillary tangles and beta-amyloid plaques in the brains of living patients with Alzheimer disease. *Am. J. Geriatr. Psychiatry* **2002**, *10*, 24–35. [[CrossRef](#)]
21. Leuzy, A.; Chiotis, K.; Lemoine, L.; Gillberg, P.-G.; Almkvist, O.; Rodriguez-Vieitez, E.; Nordberg, A. Tau PET imaging in neurodegenerative tauopathies—Still a challenge. *Mol. Psychiatry* **2019**, *24*, 1112–1134. [[CrossRef](#)] [[PubMed](#)]
22. Ossenkoppele, R.; van der Kant, R.; Hansson, O. Tau biomarkers in Alzheimer’s disease: Towards implementation in clinical practice and trials. *Lancet Neurol.* **2022**, *21*, 726–734. [[CrossRef](#)]
23. Maschio, C.; Ni, R. Amyloid and Tau Positron Emission Tomography Imaging in Alzheimer’s Disease and Other Tauopathies. *Front. Aging Neurosci.* **2022**, *14*, 838034. [[CrossRef](#)]
24. Kallinen, A.; Kassiou, M. Tracer development for PET imaging of proteinopathies. *Nucl. Med. Biol.* **2022**, *114–115*, 115–127. [[CrossRef](#)]
25. Jie, C.; Treyer, V.; Schibli, R.; Mu, L. Tauvid™: The First FDA-Approved PET Tracer for Imaging Tau Pathology in Alzheimer’s Disease. *Pharmaceuticals* **2021**, *14*, 110. [[CrossRef](#)] [[PubMed](#)]
26. Cumming, P.; Burgher, B.; Patkar, O.; Breakspear, M.; Vasdev, N.; Thomas, P.; Liu, G.-J.; Banati, R. Sifting through the surfeit of neuroinflammation tracers. *J. Cereb. Blood Flow Metab.* **2018**, *38*, 204–224. [[CrossRef](#)] [[PubMed](#)]
27. Weingarten, M.D.; Lockwood, A.H.; Hwo, S.-Y.; Kirschner, M.W. A protein factor essential for microtubule assembly. *Proc. Natl. Acad. Sci. USA* **1975**, *72*, 1858–1862. [[CrossRef](#)] [[PubMed](#)]
28. Cleveland, D.W.; Hwo, S.-Y.; Kirschner, M.W. Purification of tau, a microtubule-associated protein that induces assembly of microtubules from purified tubulin. *J. Mol. Biol.* **1977**, *116*, 207–225. [[CrossRef](#)]
29. LoPresti, P.; Szuchet, S.; Papasozomenos, S.C.; Zinkowski, R.P.; Binder, L.I. Functional implications for the microtubule-associated protein tau: Localization in oligodendrocytes. *Proc. Natl. Acad. Sci. USA* **1995**, *92*, 10369–10373. [[CrossRef](#)]
30. Ittner, A.; Ittner, L.M. Dendritic Tau in Alzheimer’s Disease. *Neuron* **2018**, *99*, 13–27. [[CrossRef](#)]
31. Neve, R.L.; Harris, P.; Kosik, K.S.; Kurnit, D.M.; Donlon, T.A. Identification of cDNA clones for the human microtubule-associated protein tau and chromosomal localization of the genes for tau and microtubule-associated protein 2. *Mol. Brain Res.* **1986**, *1*, 271–280. [[CrossRef](#)] [[PubMed](#)]
32. Andreadis, A. Misregulation of tau alternative splicing in neurodegeneration and dementia. *Altern. Splicing Dis.* **2006**, *44*, 89–107.
33. Lee, G.; Cowan, N.; Kirschner, M. The primary structure and heterogeneity of tau protein from mouse brain. *Science* **1988**, *239*, 285–288. [[CrossRef](#)] [[PubMed](#)]
34. Wang, Y.; Mandelkow, E. Tau in physiology and pathology. *Nat. Rev. Neurosci.* **2016**, *17*, 22. [[CrossRef](#)]
35. Schweers, O.; Schönbrunn-Hanebeck, E.; Marx, A.; Mandelkow, E. Structural studies of tau protein and Alzheimer paired helical filaments show no evidence for beta-structure. *J. Biol. Chem.* **1994**, *269*, 24290–24297. [[CrossRef](#)]
36. Majounie, E.; Cross, W.; Newsway, V.; Dillman, A.; Vandrovcova, J.; Morris, C.M.; Nalls, M.A.; Ferrucci, L.; Owen, M.J.; O’Donovan, M.C.; et al. Variation in tau isoform expression in different brain regions and disease states. *Neurobiol. Aging* **2013**, *34*, 1922.e7–1922.e12. [[CrossRef](#)]
37. Goedert, M.; Jakes, R. Expression of separate isoforms of human tau protein: Correlation with the tau pattern in brain and effects on tubulin polymerization. *EMBO J.* **1990**, *9*, 4225–4230. [[CrossRef](#)]
38. Spillantini, M.G.; Murrell, J.R.; Goedert, M.; Farlow, M.R.; Klug, A.; Ghetti, B. Mutation in the tau gene in familial multiple system tauopathy with presenile dementia. *Proc. Natl. Acad. Sci. USA* **1998**, *95*, 7737–7741. [[CrossRef](#)]
39. Ackmann, M.; Wiech, H.; Mandelkow, E. Nonsaturable binding indicates clustering of tau on the microtubule surface in a paired helical filament-like conformation. *J. Biol. Chem.* **2000**, *275*, 30335–30343. [[CrossRef](#)]
40. Jeganathan, S.; von Bergen, M.; Brutlach, H.; Steinhoff, H.-J.; Mandelkow, E. Global hairpin folding of tau in solution. *Biochemistry* **2006**, *45*, 2283–2293. [[CrossRef](#)]
41. Berriman, J.; Serpell, L.C.; Oberg, K.A.; Fink, A.L.; Goedert, M.; Crowther, R.A. Tau filaments from human brain and from in vitro assembly of recombinant protein show cross- β structure. *Proc. Natl. Acad. Sci. USA* **2003**, *100*, 9034–9038. [[CrossRef](#)]
42. Lim, S.; Haque, M.M.; Kim, D.; Kim, D.J.; Kim, Y.K. Cell-based Models To Investigate Tau Aggregation. *Comput. Struct. Biotechnol. J.* **2014**, *12*, 7–13. [[CrossRef](#)] [[PubMed](#)]
43. Arendt, T.; Stieler, J.; Strijkstra, A.M.; Hut, R.A.; Rüdiger, J.; Van Der Zee, E.A.; Harkany, T.; Holzer, M.; Härtig, W. Reversible paired helical filament-like phosphorylation of tau is an adaptive process associated with neuronal plasticity in hibernating animals. *J. Neurosci.* **2003**, *23*, 6972–6981. [[CrossRef](#)] [[PubMed](#)]
44. Gong, C.-X.; Iqbal, K. Hyperphosphorylation of microtubule-associated protein tau: A promising therapeutic target for Alzheimer disease. *Curr. Med. Chem.* **2008**, *15*, 2321–2328.
45. Hanger, D.P.; Anderton, B.H.; Noble, W. Tau phosphorylation: The therapeutic challenge for neurodegenerative disease. *Trends Mol. Med.* **2009**, *15*, 112–119. [[CrossRef](#)] [[PubMed](#)]
46. Shah, M.; Catafau, A.M. Molecular imaging insights into neurodegeneration: Focus on tau PET radiotracers. *J. Nucl. Med.* **2014**, *55*, 871–874. [[CrossRef](#)] [[PubMed](#)]

47. Villemagne, V.L.; Furumoto, S.; Fodero-Tavoletti, M.T.; Mulligan, R.S.; Hodges, J.; Harada, R.; Yates, P.; Piguet, O.; Pejoska, S.; Doré, V.; et al. In vivo evaluation of a novel tau imaging tracer for Alzheimer's disease. *Eur. J. Nucl. Med. Mol. Imaging* **2014**, *41*, 816–826. [[CrossRef](#)]
48. Barrio, J.R.; Huang, S.C.; Cole, G.M.; Satyamurthy, N.M.; Petric, A.; Phelps, M.E.; Small, G.W. PET imaging of tangles and plaques in Alzheimer disease with a highly hydrophobic probe. *J. Label. Compd. Radiopharm.* **1999**, *42*, S194–S195.
49. Noda, A.; Murakami, Y.; Nishiyama, S.; Fukumoto, D.; Miyoshi, S.; Tsukada, H.; Nishimura, S. Amyloid imaging in aged and young macaques with [¹¹C]PIB and [¹⁸F]FDDNP. *Synapse* **2008**, *62*, 472–475. [[CrossRef](#)]
50. Agdeppa, E.D.; Kepe, V.; Satyamurthy, N.; Liu, J.; Huang, S.-C.; Small, G.W.; Cole, G.M.; Barrio, J.R. In vitro detection of (S)-naproxen and ibuprofen binding to plaques in the Alzheimer's brain using the positron emission tomography molecular imaging probe 2-(1-{6-[(2-{¹⁸F}fluoroethyl)(methyl) amino]-2-naphthyl} ethylidene) malononitrile. *Neuroscience* **2003**, *117*, 723–730. [[PubMed](#)]
51. Landau, M.; Sawaya, M.; Faull, K.F.; Laganowsky, A.; Jiang, L.; Sievers, S.A.; Liu, J.; Barrio, J.R.; Eisenberg, D. Towards a pharmacophore for amyloid. *PLoS Biol.* **2011**, *9*, e1001080. [[CrossRef](#)]
52. Agdeppa, E.D.; Kepe, V.; Liu, J.; Flores-Torres, S.; Satyamurthy, N.; Petric, A.; Cole, G.M.; Small, G.W.; Huang, S.C.; Barrio, J.R. Binding characteristics of radiofluorinated 6-dialkylamino-2-naphthylethylidene derivatives as positron emission tomography imaging probes for β -amyloid plaques in Alzheimer's disease. *J. Neurosci.* **2001**, *21*, RC189. [[CrossRef](#)] [[PubMed](#)]
53. Harada, R.; Okamura, N.; Furumoto, S.; Tago, T.; Maruyama, M.; Higuchi, M.; Yoshikawa, T.; Arai, H.; Iwata, R.; Kudo, Y.; et al. Comparison of the binding characteristics of [¹⁸F]THK-523 and other amyloid imaging tracers to Alzheimer's disease pathology. *Eur. J. Nucl. Med. Mol. Imaging* **2013**, *40*, 125–132. [[CrossRef](#)] [[PubMed](#)]
54. Smid, L.M.; Vovko, T.D.; Popovic, M.; Petrič, A.; Kepe, V.; Barrio, J.R.; Vidmar, G.; Bresjanac, M. The 2,6-disubstituted naphthalene derivative FDDNP labeling reliably predicts Congo red birefringence of protein deposits in brain sections of selected human neurodegenerative diseases. *Brain Pathol.* **2006**, *16*, 124–130. [[CrossRef](#)] [[PubMed](#)]
55. Suemoto, T.; Okamura, N.; Shiomitsu, T.; Suzuki, M.; Shimadzu, H.; Akatsu, H.; Yamamoto, T.; Kudo, Y.; Sawada, T. In vivo labeling of amyloid with BF-108. *Neurosci. Res.* **2004**, *48*, 65–74. [[CrossRef](#)]
56. Thompson, P.W.; Ye, L.; Morgenstern, J.L.; Sue, L.; Beach, T.G.; Judd, D.J.; Shipley, N.J.; Libri, V.; Lockhart, A. Interaction of the amyloid imaging tracer FDDNP with hallmark Alzheimer's disease pathologies. *J. Neurochem.* **2009**, *109*, 623–630. [[CrossRef](#)]
57. Cole, G.B.; Satyamurthy, N.; Liu, J.; Wong, K.-P.; Small, G.W.; Huang, S.-C.; Košmrlj, J.; Barrio, J.R.; Petrič, A. The Value of In Vitro Binding as Predictor of In Vivo Results: A Case for [¹⁸F]FDDNP PET. *Mol. Imaging Biol.* **2019**, *21*, 25–34. [[CrossRef](#)]
58. Murugan, N.A.; Nordberg, A.; Ågren, H. Different Positron Emission Tomography Tau Tracers Bind to Multiple Binding Sites on the Tau Fibril: Insight from Computational Modeling. *ACS Chem. Neurosci.* **2018**, *9*, 1757–1767.
59. Small, G.W.; Kepe, V.; Ercoli, L.M.; Siddarth, P.; Bookheimer, S.Y.; Miller, K.J.; Lavretsky, H.; Burggren, A.C.; Cole, G.M.; Vinters, H.V.; et al. PET of brain amyloid and tau in mild cognitive impairment. *N. Engl. J. Med.* **2006**, *355*, 2652–2663. [[CrossRef](#)]
60. Tauber, C.; Beaufils, E.; Hommet, C.; Ribeiro, M.J.; Vercoullie, J.; Vierron, E.; Mondon, K.; Cottier, J.P.; Gissot, V.; Guilloteau, D.; et al. Brain [¹⁸F]FDDNP binding and glucose metabolism in advanced elderly healthy subjects and Alzheimer's disease patients. *J. Alzheimer's Dis.* **2013**, *36*, 311–320.
61. Tolboom, N.; van der Flier, W.M.; Yaqub, M.; Boellaard, R.; Verwey, N.A.; Blankenstein, M.A.; Windhorst, A.D.; Scheltens, P.; Lammertsma, A.A.; van Berckel, B.N. Relationship of cerebrospinal fluid markers to ¹¹C-PiB and ¹⁸F-FDDNP binding. *J. Nucl. Med.* **2009**, *50*, 1464–1470. [[CrossRef](#)] [[PubMed](#)]
62. Shin, J.; Lee, S.-Y.; Kim, S.-H.; Kim, Y.-B.; Cho, S.-J. Multitracer PET imaging of amyloid plaques and neurofibrillary tangles in Alzheimer's disease. *Neuroimage* **2008**, *43*, 236–244. [[CrossRef](#)]
63. Okamura, N.; Furumoto, S.; Fodero-Tavoletti, M.T.; Mulligan, R.S.; Harada, R.; Yates, P.; Pejoska, S.; Kudo, Y.; Masters, C.L.; Yanai, K.; et al. Non-invasive assessment of Alzheimer's disease neurofibrillary pathology using ¹⁸F-THK5105 PET. *Brain* **2014**, *137*, 1762–1771. [[CrossRef](#)] [[PubMed](#)]
64. Harada, R.; Okamura, N.; Furumoto, S.; Furukawa, K.; Ishiki, A.; Tomita, N.; Hiraoka, K.; Watanuki, S.; Shidahara, M.; Miyake, M.; et al. [¹⁸F]THK-5117 PET for assessing neurofibrillary pathology in Alzheimer's disease. *Eur. J. Nucl. Med. Mol. Imaging* **2015**, *42*, 1052–1061. [[CrossRef](#)] [[PubMed](#)]
65. Fu, L.; Zhou, K.; Zhang, X.; Zhang, J.; Cui, M.; Xu, B.; Tian, J. In vivo imaging of neurofibrillary tau PET radioligand ¹⁸F-S16 in comparison with ¹⁸F-THK5317 in Alzheimer's disease. *J. Nucl. Med.* **2020**, *61*, 1545.
66. Chanisa, C.; Monchaya, N.; Anchisa, K.; Chetsadaporn, P.; Attapon, J. Analysis of amyloid and tau deposition in Alzheimer's disease using ¹¹C-Pittsburgh compound B and ¹⁸F-THK 5351 positron emission tomography imaging. *World J. Nucl. Med.* **2020**, *20*, 61–72. [[CrossRef](#)]
67. Ezura, M.; Kikuchi, A.; Okamura, N.; Ishiki, A.; Hasegawa, T.; Harada, R.; Watanuki, S.; Funaki, Y.; Hiraoka, K.; Baba, T.; et al. ¹⁸F-THK5351 Positron Emission Tomography Imaging in Neurodegenerative Tauopathies. *Front. Aging Neurosci.* **2021**, *13*, 761010. [[CrossRef](#)]
68. Chen, J.; Li, Y.; Pirraglia, E.; Okamura, N.; Rusinek, H.; De Leon, M.J. Quantitative evaluation of tau PET tracers ¹⁸F-THK5351 and ¹⁸F-AV-1451 in Alzheimer's disease with standardized uptake value peak-alignment (SUVP) normalization. *Eur. J. Nucl. Med. Mol. Imaging* **2018**, *45*, 1596–1604. [[CrossRef](#)]

69. Kang, J.M.; Lee, S.Y.; Seo, S.; Jeong, H.J.; Woo, S.H.; Lee, H.; Lee, Y.B.; Yeon, B.K.; Shin, D.H.; Park, K.H.; et al. Tau positron emission tomography using [¹⁸F]THK5351 and cerebral glucose hypometabolism in Alzheimer's disease. *Neurobiol. Aging* **2017**, *59*, 210–219. [[CrossRef](#)]
70. Leuzy, A.; Pascoal, T.A.; Strandberg, O.; Insel, P.; Smith, R.; Mattsson-Carlgrén, N.; Benedet, A.L.; Cho, H.; Lyoo, C.H.; La Joie, R.; et al. A multicenter comparison of [¹⁸F]flortaucipir, [¹⁸F]RO948, and [¹⁸F]MK6240 tau PET tracers to detect a common target ROI for differential diagnosis. *Eur. J. Nucl. Med. Mol. Imaging* **2021**, *48*, 2295–2305. [[CrossRef](#)]
71. Li, C.-H.; Chen, T.-F.; Chiu, M.-J.; Yen, R.-F.; Shih, M.-C.; Lin, C.-H. Integrated ¹⁸F-T807 Tau PET, Structural MRI, and Plasma Tau in Tauopathy Neurodegenerative Disorders. *Front. Aging Neurosci.* **2021**, *13*, 133. [[CrossRef](#)] [[PubMed](#)]
72. Wolters, E.E.; Ossenkoppele, R.; Verfaillie, S.C.J.; Coomans, E.M.; Timmers, T.; Visser, D.; Tuncel, H.; Golla, S.S.V.; Windhorst, A.D.; Boellaard, R.; et al. Regional [¹⁸F]flortaucipir PET is more closely associated with disease severity than CSF p-tau in Alzheimer's disease. *Eur. J. Nucl. Med. Mol. Imaging* **2020**, *47*, 2866–2878. [[CrossRef](#)] [[PubMed](#)]
73. Ossenkoppele, R.; Rabinovici, G.D.; Smith, R.; Cho, H.; Schöll, M.; Strandberg, O.; Palmqvist, S.; Mattsson, N.; Janelidze, S.; Santillo, A.; et al. Discriminative accuracy of [¹⁸F]flortaucipir positron emission tomography for Alzheimer disease vs other neurodegenerative disorders. *JAMA* **2018**, *320*, 1151–1162. [[CrossRef](#)] [[PubMed](#)]
74. Pontecorvo, M.J.; Devous Sr, M.D.; Navitsky, M.; Lu, M.; Salloway, S.; Schaerf, F.W.; Jennings, D.; Arora, A.K.; McGeehan, A.; Lim, N.C.; et al. Relationships between flortaucipir PET tau binding and amyloid burden, clinical diagnosis, age and cognition. *Brain* **2017**, *140*, 748–763. [[CrossRef](#)]
75. Cho, H.; Choi, J.Y.; Hwang, M.S.; Lee, J.H.; Kim, Y.J.; Lee, H.M.; Lyoo, C.H.; Ryu, Y.H.; Lee, M.S. Tau PET in Alzheimer disease and mild cognitive impairment. *Neurology* **2016**, *87*, 375–383. [[CrossRef](#)]
76. Kitamura, S.; Shimada, H.; Niwa, F.; Endo, H.; Shinotoh, H.; Takahata, K.; Higuchi, M. Tau-induced focal neurotoxicity and network disruption related to apathy in Alzheimer's disease. *J. Neurol. Neurosurg. Psychiatry* **2018**, *89*, 1208–1214. [[CrossRef](#)]
77. Shimada, H.; Kitamura, S.; Shinotoh, H.; Endo, H.; Niwa, F.; Hirano, S.; Kimura, Y.; Zhang, M.R.; Kuwabara, S.; Suhara, T.; et al. Association between Aβ and tau accumulations and their influence on clinical features in aging and Alzheimer's disease spectrum brains: A [¹¹C]PBB3-PET study. *Alzheimer's Dement.* **2017**, *6*, 11–20. [[CrossRef](#)]
78. Hsu, J.-L.; Lin, K.-J.; Hsiao, I.-T.; Huang, K.-L.; Liu, C.-H.; Wu, H.-C.; Weng, Y.-C.; Huang, C.-Y.; Chang, C.-C.; Yen, T.-C.; et al. The Imaging Features and Clinical Associations of a Novel Tau PET Tracer—¹⁸F-APN1607 in Alzheimer Disease. *Clin. Nucl. Med.* **2020**, *45*, 747–756. [[CrossRef](#)]
79. Lu, J.; Bao, W.; Li, M.; Li, L.; Zhang, Z.; Alberts, I.; Brendel, M.; Cumming, P.; Lu, H.; Xiao, Z.; et al. Associations of [¹⁸F]-APN-1607 Tau PET Binding in the Brain of Alzheimer's Disease Patients with Cognition and Glucose Metabolism. *Front. Neurosci.* **2020**, *14*, 604. [[CrossRef](#)]
80. Therriault, J.; Pascoal, T.A.; Lussier, F.Z.; Tissot, C.; Chamoun, M.; Bezgin, G.; Servaes, S.; Benedet, A.L.; Ashton, N.J.; Karikari, T.K.; et al. Biomarker modeling of Alzheimer's disease using PET-based Braak staging. *Nat. Aging* **2022**, *2*, 526–535. [[CrossRef](#)]
81. Ashton, N.J.; Pascoal, T.A.; Karikari, T.K.; Benedet, A.L.; Lantero-Rodriguez, J.; Brinkmalm, G.; Snellman, A.; Schöll, M.; Troakes, C.; Hye, A.; et al. Plasma p-tau231: A new biomarker for incipient Alzheimer's disease pathology. *Acta Neuropathol.* **2021**, *141*, 709–724. [[CrossRef](#)] [[PubMed](#)]
82. Therriault, J.; Pascoal, T.A.; Savard, M.; Benedet, A.L.; Chamoun, M.; Tissot, C.; Lussier, F.; Kang, M.S.; Thomas, E.; Terada, T.; et al. Topographic distribution of Amyloid-β, Tau, and Atrophy in patients with behavioral/dysexecutive Alzheimer disease. *Neurology* **2021**, *96*, e81–e92. [[CrossRef](#)] [[PubMed](#)]
83. Therriault, J.; Pascoal, T.A.; Benedet, A.L.; Tissot, C.; Savard, M.; Chamoun, M.; Lussier, F.; Kang, M.S.; Berzgin, G.; Wang, T.; et al. Frequency of biologically defined Alzheimer disease in relation to age, sex, APOE ε4, and cognitive impairment. *Neurology* **2021**, *96*, e975–e985. [[CrossRef](#)] [[PubMed](#)]
84. Tissot, C.; Therriault, J.; Pascoal, T.A.; Chamoun, M.; Lussier, F.Z.; Savard, M.; Mathotaarachchi, S.S.; Benedet, A.L.; Thomas, E.M.; Parsons, M.; et al. Association between regional tau pathology and neuropsychiatric symptoms in aging and dementia due to Alzheimer's disease. *Alzheimer's Dement.* **2021**, *7*, e12154. [[CrossRef](#)]
85. Pascoal, T.A.; Therriault, J.; Benedet, A.L.; Savard, M.; Lussier, F.Z.; Chamoun, M.; Tissot, C.; Qureshi, M.N.I.; Kang, M.S.; Mathotaarachchi, S.; et al. ¹⁸F-MK-6240 PET for early and late detection of neurofibrillary tangles. *Brain* **2020**, *143*, 2818–2830. [[CrossRef](#)] [[PubMed](#)]
86. Barthélemy, N.R.; Toth, B.; Manser, P.T.; Sanabria-Bohórquez, S.; Teng, E.; Keeley, M.; Bateman, R.J.; Weimer, R.M.; Wildsmith, K.R. Site-Specific Cerebrospinal Fluid Tau Hyperphosphorylation in Response to Alzheimer's Disease Brain Pathology: Not All Tau Phospho-Sites are Hyperphosphorylated. *J. Alzheimer's Dis.* **2022**, *85*, 415–429. [[CrossRef](#)]
87. Leuzy, A.; Smith, R.; Cullen, N.C.; Strandberg, O.; Vogel, J.W.; Binette, A.P.; Borroni, E.; Janelidze, S.; Ohlsson, T.; Jögi, J.; et al. Biomarker-based prediction of longitudinal tau positron emission tomography in Alzheimer disease. *JAMA Neurol.* **2022**, *79*, 149–158. [[CrossRef](#)] [[PubMed](#)]
88. Leuzy, A.; Smith, R.; Ossenkoppele, R.; Santillo, A.; Borroni, E.; Klein, G.; Ohlsson, T.; Jögi, J.; Palmqvist, S.; Mattsson-Carlgrén, N.; et al. Diagnostic performance of RO948 F 18 tau positron emission tomography in the differentiation of Alzheimer disease from other neurodegenerative disorders. *JAMA Neurol.* **2020**, *77*, 955–965. [[CrossRef](#)]
89. Wong, D.F.; Comley, R.A.; Kuwabara, H.; Rosenberg, P.B.; Resnick, S.M.; Ostrowitzki, S.; Vozzi, C.; Boess, F.; Oh, E.; Lyketsos, C.G.; et al. Characterization of 3 novel tau radiopharmaceuticals, ¹¹C-RO-963, ¹¹C-RO-643, and ¹⁸F-RO-948, in healthy controls and in Alzheimer subjects. *J. Nucl. Med.* **2018**, *59*, 1869–1876. [[CrossRef](#)]

90. Schmidt, M.E.; Janssens, L.; Moechars, D.; Rombouts, F.J.R.; Timmers, M.; Barret, O.; Constantinescu, C.C.; Madonia, J.; Russell, D.S.; Sandiego, C.M.; et al. Clinical evaluation of [¹⁸F]NJ-64326067, a novel candidate PET tracer for the detection of tau pathology in Alzheimer's disease. *Eur. J. Nucl. Med. Mol. Imaging* **2020**, *47*, 3176–3185. [[CrossRef](#)]
91. Bun, S.; Moriguchi, S.; Tezuka, T.; Sato, Y.; Takahata, K.; Seki, M.; Nakajima, S.; Yamamoto, Y.; Sano, Y.; Suzuki, N.; et al. Findings of ¹⁸F-PI-2620 tau PET imaging in patients with Alzheimer's disease and healthy controls in relation to the plasma P-tau181 levels in a Japanese sample. *Neuropsychopharmacol. Rep.* **2022**, *42*, 437–448. [[CrossRef](#)] [[PubMed](#)]
92. Jantarato, A.; Vachatanont, S.; Boonkawin, N.; Yaset, S.; Kunawudhi, A.; Promteangtrong, C.; Assanasen, J.; Mahanonda, N.; Chotipanich, C. The Evaluation of Tau Deposition with [¹⁸F]PI-2620 by Using a Semiquantitative Method in Cognitively Normal Subjects and Patients with Mild Cognitive Impairment and Alzheimer's Disease. *Mol. Imaging* **2021**, *2021*, 6640054. [[CrossRef](#)] [[PubMed](#)]
93. Mueller, A.; Bullich, S.; Barret, O.; Madonia, J.; Berndt, M.; Papin, C.; Perrotin, A.; Koglin, N.; Kroth, H.; Pfeifer, A.; et al. Tau PET imaging with ¹⁸F-PI-2620 in patients with Alzheimer disease and healthy controls: A first-in-humans study. *J. Nucl. Med.* **2020**, *61*, 911–919. [[CrossRef](#)] [[PubMed](#)]
94. Fu, L.; Zhang, J.; Zhou, K.; Zhang, X.; Xie, H.; Zhu, M.; Cui, M.; Wang, R. In vivo imaging of tau deposition in Alzheimer's disease using both [¹⁸F]-THK5317 and [¹⁸F]-S16: A pilot human study. *Front. Aging Neurosci.* **2022**, *14*, 994750. [[CrossRef](#)] [[PubMed](#)]
95. Wang, Y.; Cai, L.; Zhou, K.; Cui, M.; Yao, S. Biodistribution and dosimetry evaluation for a novel tau tracer [¹⁸F]-S16 in healthy volunteers and its application in assessment of tau pathology in Alzheimer's disease. *Front. Bioeng. Biotechnol.* **2022**, *9*, 1515. [[CrossRef](#)] [[PubMed](#)]
96. Tolboom, N.; Yaqub, M.; van der Flier, W.M.; Boellaard, R.; Luurtsema, G.; Windhorst, A.D.; Barkhof, F.; Scheltens, P.; Lammertsma, A.A.; van Berckel, B.N. Detection of Alzheimer pathology in vivo using both ¹¹C-PIB and ¹⁸F-FDDNP PET. *J. Nucl. Med.* **2009**, *50*, 191–197. [[CrossRef](#)]
97. Small, G.W.; Siddarth, P.; Burggren, A.C.; Kepe, V.; Ercoli, L.M.; Miller, K.J.; Lavretsky, H.; Thompson, P.; Cole, G.M.; Huang, S.C.; et al. Influence of cognitive status, age, and APOE-4 genetic risk on brain FDDNP positron-emission tomography imaging in persons without dementia. *Arch. Gen. Psychiatry* **2009**, *66*, 81–87. [[CrossRef](#)]
98. Tolboom, N.; Koedam, E.L.; Schott, J.M.; Yaqub, M.; Blankenstein, M.A.; Barkhof, F.; Pijnenburg, Y.A.; Lammertsma, A.A.; Scheltens, P.; van Berckel, B.N. Dementia mimicking Alzheimer's disease Owing to a tau mutation: CSF and PET findings. *Alzheimer Dis. Assoc. Disord.* **2010**, *24*, 303–307. [[CrossRef](#)]
99. Okamura, N.; Suemoto, T.; Furumoto, S.; Suzuki, M.; Shimadzu, H.; Akatsu, H.; Yamamoto, T.; Fujiwara, H.; Nemoto, M.; Maruyama, M.; et al. Quinoline and benzimidazole derivatives: Candidate probes for in vivo imaging of tau pathology in Alzheimer's disease. *J. Neurosci.* **2005**, *25*, 10857–10862. [[CrossRef](#)] [[PubMed](#)]
100. Fodero-Tavoletti, M.T.; Okamura, N.; Furumoto, S.; Mulligan, R.S.; Connor, A.R.; McLean, C.A.; Cao, D.; Rigopoulos, A.; Cartwright, G.A.; O'Keefe, G.; et al. ¹⁸F-THK523: A novel in vivo tau imaging ligand for Alzheimer's disease. *Brain* **2011**, *134*, 1089–1100. [[CrossRef](#)] [[PubMed](#)]
101. Bouras, C.; Hof, P.R.; Giannakopoulos, P.; Michel, J.-P.; Morrison, J.H. Regional distribution of neurofibrillary tangles and senile plaques in the cerebral cortex of elderly patients: A quantitative evaluation of a one-year autopsy population from a geriatric hospital. *Cereb. Cortex* **1994**, *4*, 138–150. [[CrossRef](#)] [[PubMed](#)]
102. Tago, T.; Furumoto, S.; Okamura, N.; Harada, R.; Ishikawa, Y.; Arai, H.; Yanai, K.; Iwata, R.; Kudo, Y. Synthesis and preliminary evaluation of 2-arylhydroxyquinoline derivatives for tau imaging. *J. Label. Compd. Radiopharm.* **2014**, *57*, 18–24. [[CrossRef](#)]
103. Cai, L.; Qu, B.; Hurtle, B.T.; Dadiboyena, S.; Diaz-Arrastia, R.; Pike, V.W. Candidate PET radioligand development for neurofibrillary tangles: Two distinct radioligand binding sites identified in postmortem Alzheimer's disease brain. *ACS Chem. Neurosci.* **2016**, *7*, 897–911. [[CrossRef](#)] [[PubMed](#)]
104. Murugan, N.A.; Chiotis, K.; Rodriguez-Vieitez, E.; Lemoine, L.; Ågren, H.; Nordberg, A. Cross-interaction of tau PET tracers with monoamine oxidase B: Evidence from in silico modelling and in vivo imaging. *Eur. J. Nucl. Med. Mol. Imaging* **2019**, *46*, 1369–1382. [[CrossRef](#)] [[PubMed](#)]
105. Okamura, N.; Furumoto, S.; Harada, R.; Tago, T.; Yoshikawa, T.; Fodero-Tavoletti, M.; Mulligan, R.S.; Villemagne, V.L.; Akatsu, H.; Yamamoto, T.; et al. Novel ¹⁸F-labeled arylquinoline derivatives for noninvasive imaging of tau pathology in Alzheimer disease. *J. Nucl. Med.* **2013**, *54*, 1420–1427. [[CrossRef](#)]
106. Fodero-Tavoletti, M.T.; Furumoto, S.; Taylor, L.; McLean, C.A.; Mulligan, R.S.; Birchall, I.; Harada, R.; Masters, C.L.; Yanai, K.; Kudo, Y.; et al. Assessing THK523 selectivity for tau deposits in Alzheimer's disease and non-Alzheimer's disease tauopathies. *Alzheimer's Res. Ther.* **2014**, *6*, 11. [[CrossRef](#)] [[PubMed](#)]
107. Mukaetova-Ladinska, E.; Harrington, C.; Roth, M.; Wischik, C. Biochemical and anatomical redistribution of tau protein in Alzheimer's disease. *Am. J. Pathol.* **1993**, *143*, 565.
108. Tago, T.; Furumoto, S.; Okamura, N.; Harada, R.; Adachi, H.; Ishikawa, Y.; Yanai, K.; Iwata, R.; Kudo, Y. Preclinical evaluation of [¹⁸F]THK-5105 enantiomers: Effects of chirality on its effectiveness as a tau imaging radiotracer. *Mol. Imaging Biol.* **2016**, *18*, 258–266. [[CrossRef](#)]
109. Lemoine, L.; Saint-Aubert, L.; Marutle, A.; Antoni, G.; Eriksson, J.P.; Ghetti, B.; Okamura, N.; Nennesmo, I.; Gillberg, P.-G.; Nordberg, A. Visualization of regional tau deposits using ³H-THK5117 in Alzheimer brain tissue. *Acta Neuropathol. Commun.* **2015**, *3*, 40. [[CrossRef](#)]

110. Lemoine, L.; Saint-Aubert, L.; Nennesmo, I.; Gillberg, P.-G.; Nordberg, A. Cortical laminar tau deposits and activated astrocytes in Alzheimer's disease visualised by ^3H -THK5117 and ^3H -deprenyl autoradiography. *Sci. Rep.* **2017**, *7*, srep45496. [[CrossRef](#)]
111. Kolb, H.C.; Andrés, J.I. Tau Positron Emission Tomography Imaging. *Cold Spring Harb. Perspect. Biol.* **2017**, *9*, a023721. [[CrossRef](#)] [[PubMed](#)]
112. Ishiki, A.; Harada, R.; Kai, H.; Sato, N.; Totsune, T.; Tomita, N.; Watanuki, S.; Hiraoka, K.; Ishikawa, Y.; Funaki, Y.; et al. Neuroimaging-pathological correlations of [^{18}F]THK5351 PET in progressive supranuclear palsy. *Acta Neuropathol. Commun.* **2018**, *6*, 53. [[CrossRef](#)] [[PubMed](#)]
113. Ishiki, A.; Okamura, N.; Furukawa, K.; Furumoto, S.; Harada, R.; Tomita, N.; Hiraoka, K.; Watanuki, S.; Ishikawa, Y.; Tago, T.; et al. Longitudinal assessment of tau pathology in patients with Alzheimer's disease using [^{18}F] THK-5117 positron emission tomography. *PLoS ONE* **2015**, *10*, e0140311. [[CrossRef](#)]
114. Jonasson, M.; Wall, A.; Chiotis, K.; Saint-Aubert, L.; Wilking, H.; Spryca, M.; Borg, B.; Thibblin, A.; Eriksson, J.; Eriksson, J.; et al. Tracer kinetic analysis of (S)- ^{18}F -THK5117 as a PET tracer for assessing tau pathology. *J. Nucl. Med.* **2016**, *57*, 574–581. [[CrossRef](#)]
115. Chiotis, K.; Saint-Aubert, L.; Savitcheva, I.; Jelic, V.; Andersen, P.; Jonasson, M.; Eriksson, J.; Lubberink, M.; Almkvist, O.; Wall, A.; et al. Imaging in-vivo tau pathology in Alzheimer's disease with THK5317 PET in a multimodal paradigm. *Eur. J. Nucl. Med. Mol. Imaging* **2016**, *43*, 1686–1699. [[CrossRef](#)]
116. Harada, R.; Okamura, N.; Furumoto, S.; Furukawa, K.; Ishiki, A.; Tomita, N.; Tago, T.; Hiraoka, K.; Watanuki, S.; Shidahara, M.; et al. ^{18}F -THK5351: A novel PET radiotracer for imaging neurofibrillary pathology in Alzheimer disease. *J. Nucl. Med.* **2016**, *57*, 208–214. [[CrossRef](#)] [[PubMed](#)]
117. Tago, T.; Toyohara, J.; Harada, R.; Furumoto, S.; Okamura, N.; Kudo, Y.; Takahashi-Fujigasaki, J.; Murayama, S.; Ishii, K. Characterization of the binding of tau imaging ligands to melanin-containing cells: Putative off-target-binding site. *Ann. Nucl. Med.* **2019**, *33*, 375–382. [[CrossRef](#)]
118. Villemagne, V.L.; Fodero-Tavoletti, M.T.; Masters, C.L.; Rowe, C.C. Tau imaging: Early progress and future directions. *Lancet Neurol.* **2015**, *14*, 114–124. [[CrossRef](#)]
119. Lockhart, S.N.; Baker, S.L.; Okamura, N.; Furukawa, K.; Ishiki, A.; Furumoto, S.; Tashiro, M.; Yanai, K.; Arai, H.; Kudo, Y.; et al. Dynamic PET measures of tau accumulation in cognitively normal older adults and Alzheimer's disease patients measured using [^{18}F] THK-5351. *PLoS ONE* **2016**, *11*, e0158460. [[CrossRef](#)]
120. Sone, D.; Imabayashi, E.; Maikusa, N.; Okamura, N.; Furumoto, S.; Kudo, Y.; Ogawa, M.; Takano, H.; Yokoi, Y.; Sakata, M.; et al. Regional tau deposition and subregion atrophy of medial temporal structures in early Alzheimer's disease: A combined positron emission tomography/magnetic resonance imaging study. *Alzheimer's Dement. Diagn. Assess. Dis. Monit.* **2017**, *9*, 35–40. [[CrossRef](#)]
121. Betthausen, T.J.; Lao, P.J.; Murali, D.; Barnhart, T.E.; Furumoto, S.; Okamura, N.; Stone, C.K.; Johnson, S.C.; Christian, B.T. In vivo comparison of tau radioligands ^{18}F -THK-5351 and ^{18}F -THK-5317. *J. Nucl. Med.* **2017**, *58*, 996–1002. [[CrossRef](#)] [[PubMed](#)]
122. Chiotis, K.; Stenkrona, P.; Almkvist, O.; Stepanov, V.; Ferreira, D.; Arakawa, R.; Takano, A.; Westman, E.; Varrone, A.; Okamura, N.; et al. Dual tracer tau PET imaging reveals different molecular targets for ^{11}C -THK5351 and ^{11}C -PBB3 in the Alzheimer brain. *Eur. J. Nucl. Med. Mol. Imaging* **2018**, *45*, 1605–1617. [[CrossRef](#)]
123. Oh, M.; Oh, S.J.; Lee, S.J.; Oh, J.S.; Roh, J.H.; Chung, S.J.; Lee, J.-H.; Lee, C.S.; Kim, J.S. Clinical Evaluation of ^{18}F -PI-2620 as a Potent PET Radiotracer Imaging Tau Protein in Alzheimer Disease and Other Neurodegenerative Diseases Compared with ^{18}F -THK-5351. *Clin. Nucl. Med.* **2020**, *45*, 841–847. [[CrossRef](#)]
124. Jang, Y.K.; Lyoo, C.H.; Park, S.; Oh, S.J.; Cho, H.; Oh, M.; Ryu, Y.H.; Choi, J.Y.; Rabinovici, G.D.; Kim, H.J.; et al. Head to head comparison of [^{18}F]AV-1451 and [^{18}F] THK5351 for tau imaging in Alzheimer's disease and frontotemporal dementia. *Eur. J. Nucl. Med. Mol. Imaging* **2018**, *45*, 432–442. [[CrossRef](#)]
125. Lemoine, L.; Gillberg, P.-G.; Svedberg, M.; Stepanov, V.; Jia, Z.; Huang, J.; Nag, S.; Tian, H.; Ghetti, B.; Okamura, N.; et al. Comparative binding properties of the tau PET tracers THK5117, THK5351, PBB3, and T807 in postmortem Alzheimer brains. *Alzheimer's Res. Ther.* **2017**, *9*, 96. [[CrossRef](#)] [[PubMed](#)]
126. Ng, K.P.; Therriault, J.; Kang, M.S.; Struyfs, H.; Pascoal, T.A.; Mathotaarachchi, S.; Shin, M.; Benedet, A.L.; Massarweh, G.; Soucy, J.-P.; et al. Rasagiline, a monoamine oxidase B inhibitor, reduces in vivo [^{18}F]THK5351 uptake in progressive supranuclear palsy. *NeuroImage Clin.* **2019**, *24*, 102091. [[CrossRef](#)]
127. Lemoine, L.; Leuzy, A.; Chiotis, K.; Rodriguez-Vieitez, E.; Nordberg, A. Tau positron emission tomography imaging in tauopathies: The added hurdle of off-target binding. *Alzheimer's Dement. Diagn. Assess. Dis. Monit.* **2018**, *10*, 232–236. [[CrossRef](#)] [[PubMed](#)]
128. Harada, R.; Ishiki, A.; Kai, H.; Sato, N.; Furukawa, K.; Furumoto, S.; Tago, T.; Tomita, N.; Watanuki, S.; Hiraoka, K.; et al. Correlations of ^{18}F -THK5351 PET with postmortem burden of tau and astrogliosis in Alzheimer disease. *J. Nucl. Med.* **2018**, *59*, 671–674. [[CrossRef](#)]
129. Pascoal, T.A.; Shin, M.; Kang, M.S.; Chamoun, M.; Chartrand, D.; Mathotaarachchi, S.; Bennacef, I.; Therriault, J.; Ng, K.P.; Hopewell, R.; et al. In vivo quantification of neurofibrillary tangles with [^{18}F]MK-6240. *Alzheimer's Res. Ther.* **2018**, *10*, 74. [[CrossRef](#)]
130. Zhou, K.; Yang, F.; Li, Y.; Chen, Y.; Zhang, X.; Zhang, J.; Wang, J.; Dai, J.; Cai, L.; Cui, M. Synthesis and evaluation of fluorine-18 labeled 2-phenylquinoxaline derivatives as potential tau imaging agents. *Mol. Pharm.* **2021**, *18*, 1176–1195. [[CrossRef](#)]

131. Rojo, L.E.; Alzate-Morales, J.; Saavedra, I.N.; Davies, P.; Maccioni, R.B. Selective interaction of lansoprazole and astemizole with tau polymers: Potential new clinical use in diagnosis of Alzheimer's disease. *J. Alzheimer's Dis.* **2010**, *19*, 573–589. [[CrossRef](#)] [[PubMed](#)]
132. Fawaz, M.V.; Brooks, A.F.; Rodnick, M.E.; Carpenter, G.M.; Shao, X.; Desmond, T.J.; Sherman, P.; Quesada, C.A.; Hockley, B.G.; Kilbourn, M.R.; et al. High affinity radiopharmaceuticals based upon lansoprazole for PET imaging of aggregated tau in Alzheimer's disease and progressive supranuclear palsy: Synthesis, preclinical evaluation, and lead selection. *ACS Chem. Neurosci.* **2014**, *5*, 718–730. [[CrossRef](#)]
133. Riss, P.J.; Brichard, L.; Ferrari, V.; Williamson, D.J.; Fryer, T.D.; Hong, Y.T.; Baron, J.-C.; Aigbirhio, F.I. Radiosynthesis and characterization of astemizole derivatives as lead compounds toward PET imaging of τ -pathology. *MedChemComm* **2013**, *4*, 852–855. [[CrossRef](#)]
134. Kramer, V.; Brooks, A.F.; Haeger, A.; Kuljis, R.O.; Rafique, W.; Koeppe, R.A.; Raffel, D.M.; Frey, K.A.; Amaral, H.; Scott, P.J.H.; et al. Evaluation of [^{18}F]-N-Methyl lansoprazole as a Tau PET Imaging Agent in First-in-Human Studies. *ACS Chem. Neurosci.* **2020**, *11*, 427–435. [[CrossRef](#)]
135. Shao, X.; Carpenter, G.M.; Desmond, T.J.; Sherman, P.; Quesada, C.A.; Fawaz, M.; Brooks, A.F.; Kilbourn, M.R.; Albin, R.L.; Frey, K.A.; et al. Evaluation of [^{11}C]N-methyl lansoprazole as a radiopharmaceutical for PET imaging of tau neurofibrillary tangles. *ACS Med. Chem. Lett.* **2012**, *3*, 936–941. [[CrossRef](#)]
136. Rafique, W.; Kramer, V.; Pardo, T.; Smits, R.; Spilhaug, M.M.; Hoeppe, A.; Savio, E.; Engler, H.; Kuljis, R.; Amaral, H.; et al. Image-guided development of heterocyclic sulfoxides as ligands for tau neurofibrillary tangles: From first-in-man to second-generation ligands. *ACS Omega* **2018**, *3*, 7567–7579. [[CrossRef](#)] [[PubMed](#)]
137. Betthausen, T.J. 1cii—AD molecular: Imaging tau aggregates with positron emissions tomography. In *Progress in Molecular Biology and Translational Science*; Becker, J.T., Cohen, A.D., Eds.; Academic Press: Cambridge, MA, USA, 2019; Volume 165, pp. 107–138.
138. Xia, C.-F.; Arteaga, J.; Chen, G.; Gangadharmath, U.; Gomez, L.F.; Kasi, D.; Lam, C.; Liang, Q.; Liu, C.; Mocharla, V.P.; et al. [^{18}F]T807, a novel tau positron emission tomography imaging agent for Alzheimer's disease. *Alzheimer's Dement.* **2013**, *9*, 666–676. [[CrossRef](#)]
139. Zhang, W.; Arteaga, J.; Cashion, D.K.; Chen, G.; Gangadharmath, U.; Gomez, L.F.; Kasi, D.; Lam, C.; Liang, Q.; Liu, C.; et al. A highly selective and specific PET tracer for imaging of tau pathologies. *J. Alzheimer's Dis.* **2012**, *31*, 601–612. [[CrossRef](#)]
140. Chien, D.T.; Bahri, S.; Szardenings, A.K.; Walsh, J.C.; Mu, F.; Su, M.-Y.; Shankle, W.R.; Elizarov, A.; Kolb, H.C. Early Clinical PET Imaging Results with the Novel PHF-Tau Radioligand [F-18]-T807. *J. Alzheimer's Dis.* **2013**, *34*, 457–468. [[CrossRef](#)]
141. Marquié, M.; Normandin, M.D.; Vanderburg, C.R.; Costantino, I.M.; Bien, E.A.; Rycyna, L.G.; Klunk, W.E.; Mathis, C.A.; Ikonovic, M.D.; Debnath, M.L.; et al. Validating novel tau positron emission tomography tracer [F-18]-AV-1451 (T807) on postmortem brain tissue. *Ann. Neurol.* **2015**, *78*, 787–800. [[CrossRef](#)]
142. Chhatwal, J.P.; Schultz, A.P.; Marshall, G.A.; Boot, B.; Gomez-Isla, T.; Dumurgier, J.; LaPoint, M.; Scherzer, C.; Roe, A.D.; Hyman, B.T.; et al. Temporal T807 binding correlates with CSF tau and phospho-tau in normal elderly. *Neurology* **2016**, *87*, 920–926. [[CrossRef](#)]
143. Lowe, V.J.; Curran, G.; Fang, P.; Liesinger, A.M.; Josephs, K.A.; Parisi, J.E.; Kantarci, K.; Boeve, B.F.; Pandey, M.K.; Bruinsma, T.; et al. An autoradiographic evaluation of AV-1451 Tau PET in dementia. *Acta Neuropathol. Commun.* **2016**, *4*, 58. [[CrossRef](#)] [[PubMed](#)]
144. Smith, R.; Puschmann, A.; Schöll, M.; Ohlsson, T.; van Swieten, J.; Honer, M.; Englund, E.; Hansson, O. ^{18}F -AV-1451 tau PET imaging correlates strongly with tau neuropathology in MAPT mutation carriers. *Brain* **2016**, *139*, 2372–2379. [[CrossRef](#)] [[PubMed](#)]
145. Gordon, B.A.; Friedrichsen, K.; Brier, M.; Blazey, T.; Su, Y.; Christensen, J.; Aldea, P.; McConathy, J.; Holtzman, D.M.; Cairns, N.J.; et al. The relationship between cerebrospinal fluid markers of Alzheimer pathology and positron emission tomography tau imaging. *Brain* **2016**, *139*, 2249–2260. [[CrossRef](#)] [[PubMed](#)]
146. Mattsson, N.; Schöll, M.; Strandberg, O.; Smith, R.; Palmqvist, S.; Insel, P.S.; Hägerström, D.; Ohlsson, T.; Zetterberg, H.; Jögi, J.; et al. ^{18}F -AV-1451 and CSF T-tau and P-tau as biomarkers in Alzheimer's disease. *EMBO Mol. Med.* **2017**, *9*, 1212–1223. [[CrossRef](#)]
147. Vermeiren, C.; Motte, P.; Viot, D.; Mairet-Coello, G.; Courade, J.P.; Citron, M.; Mercier, J.; Hannestad, J.; Gillard, M. The tau positron-emission tomography tracer AV-1451 binds with similar affinities to tau fibrils and monoamine oxidases. *Mov. Disord.* **2018**, *33*, 273–281. [[CrossRef](#)]
148. Hansen, A.K.; Brooks, D.J.; Borghammer, P. MAO-B inhibitors do not block in vivo flortaucipir (^{18}F -AV-1451) binding. *Mol. Imaging Biol.* **2018**, *20*, 356–360. [[CrossRef](#)]
149. Chien, D.T.; Szardenings, A.K.; Bahri, S.; Walsh, J.C.; Mu, F.; Xia, C.; Shankle, W.R.; Lerner, A.J.; Su, M.-Y.; Elizarov, A.; et al. Early clinical PET imaging results with the novel PHF-tau radioligand [F18]-T808. *J. Alzheimer's Dis.* **2014**, *38*, 171–184. [[CrossRef](#)]
150. Mattsson, N.; Insel, P.S.; Donohue, M.; Jögi, J.; Ossenkoppele, R.; Olsson, T.; Schöll, M.; Smith, R.; Hansson, O. Predicting diagnosis and cognition with ^{18}F -AV-1451 tau PET and structural MRI in Alzheimer's disease. *Alzheimer's Dement.* **2019**, *15*, 570–580. [[CrossRef](#)]
151. Brier, M.R.; Gordon, B.; Friedrichsen, K.; McCarthy, J.; Stern, A.; Christensen, J.; Owen, C.; Aldea, P.; Su, Y.; Hassenstab, J.; et al. Tau and A β imaging, CSF measures, and cognition in Alzheimer's disease. *Sci. Transl. Med.* **2016**, *8*, 338ra66. [[CrossRef](#)]
152. Johnson, K.A.; Schultz, A.; Betensky, R.A.; Becker, J.A.; Sepulcre, J.; Rentz, D.; Mormino, E.; Chhatwal, J.; Amariglio, R.; Papp, K.; et al. Tau positron emission tomographic imaging in aging and early Alzheimer disease. *Ann. Neurol.* **2016**, *79*, 110–119. [[CrossRef](#)]

153. Schöll, M.; Lockhart, S.N.; Schonhaut, D.R.; O'Neil, J.P.; Janabi, M.; Ossenkoppele, R.; Baker, S.L.; Vogel, J.W.; Faria, J.; Schwimmer, H.D.; et al. PET Imaging of Tau Deposition in the Aging Human Brain. *Neuron* **2016**, *89*, 971–982. [[CrossRef](#)] [[PubMed](#)]
154. Schwarz, A.J.; Yu, P.; Miller, B.B.; Shcherbinin, S.; Dickson, J.; Navitsky, M.; Joshi, A.D.; Devous Sr, M.D.; Mintun, M.S. Regional profiles of the candidate tau PET ligand ¹⁸F-AV-1451 recapitulate key features of Braak histopathological stages. *Brain* **2016**, *139*, 1539–1550. [[CrossRef](#)]
155. Devous Sr, M.D.; Joshi, A.D.; Navitsky, M.; Southekal, S.; Pontecorvo, M.J.; Shen, H.; Lu, M.; Shankle, W.R.; Seibyl, J.P.; Marek, K.; et al. Test–retest reproducibility for the tau PET imaging agent Flortaucipir F18. *J. Nucl. Med.* **2018**, *59*, 937–943. [[CrossRef](#)]
156. Soleimani-Meigooni, D.N.; Iaccarino, L.; La Joie, R.; Baker, S.; Bourakova, V.; Boxer, A.L.; Edwards, L.; Eser, R.; Gorno-Tempini, M.-L.; Jagust, W.J.; et al. ¹⁸F-flortaucipir PET to autopsy comparisons in Alzheimer's disease and other neurodegenerative diseases. *Brain* **2020**, *143*, 3477–3494. [[CrossRef](#)] [[PubMed](#)]
157. Schöll, M.; Ossenkoppele, R.; Strandberg, O.; Palmqvist, S.; Jögi, J.; Ohlsson, T.; Smith, R.; Hansson, O. The Swedish BioFINDER Study. Distinct ¹⁸F-AV-1451 tau PET retention patterns in early- and late-onset Alzheimer's disease. *Brain* **2017**, *140*, 2286–2294. [[CrossRef](#)] [[PubMed](#)]
158. Wood, H. Alzheimer disease: [¹¹C]PBB3—A new PET ligand that identifies tau pathology in the brains of patients with AD. *Nat. Rev. Neurol.* **2013**, *9*, 599. [[CrossRef](#)] [[PubMed](#)]
159. Maruyama, M.; Shimada, H.; Suhara, T.; Shinotoh, H.; Ji, B.; Maeda, J.; Zhang, M.R.; Trojanowski, J.Q.; Lee, V.M.; Ono, M.; et al. Imaging of tau pathology in a tauopathy mouse model and in Alzheimer patients compared to normal controls. *Neuron* **2013**, *79*, 1094–1108. [[CrossRef](#)]
160. Ni, R.; Ji, B.; Ono, M.; Sahara, N.; Zhang, M.-R.; Aoki, I.; Nordberg, A.; Suhara, T.; Higuchi, M. Comparative In Vitro and In Vivo Quantifications of Pathologic Tau Deposits and Their Association with Neurodegeneration in Tauopathy Mouse Models. *J. Nucl. Med.* **2018**, *59*, 960–966. [[CrossRef](#)]
161. Okamura, N.; Harada, R.; Furumoto, S.; Arai, H.; Yanai, K.; Kudo, Y. Tau PET imaging in Alzheimer's disease. *Curr. Neurol. Neurosci. Rep.* **2014**, *14*, 500. [[CrossRef](#)]
162. Ono, M.; Sahara, N.; Kumata, K.; Ji, B.; Ni, R.; Koga, S.; Dickson, D.W.; Trojanowski, J.Q.; Lee, V.M.-Y.; Yoshida, M.; et al. Distinct binding of PET ligands PBB3 and AV-1451 to tau fibril strains in neurodegenerative tauopathies. *Brain* **2017**, *140*, 764–780. [[CrossRef](#)] [[PubMed](#)]
163. Declercq, L.; Celen, S.; Lecina, J.; Ahamed, M.; Tousseyn, T.; Moechars, D.; Alcazar, J.; Ariza, M.; Fierens, K.; Bottelbergs, A.; et al. Comparison of New Tau PET-Tracer Candidates with [¹⁸F]T808 and [¹⁸F]T807. *Mol. Imaging* **2016**, *15*, 1536012115624920. [[CrossRef](#)] [[PubMed](#)]
164. Koga, S.; Ono, M.; Sahara, N.; Higuchi, M.; Dickson, D.W. Fluorescence and autoradiographic evaluation of tau PET ligand PBB3 to α -synuclein pathology. *Mov. Disord.* **2017**, *32*, 884–892. [[CrossRef](#)] [[PubMed](#)]
165. Kimura, Y.; Ichise, M.; Ito, H.; Shimada, H.; Ikoma, Y.; Seki, C.; Takano, H.; Kitamura, S.; Shinotoh, H.; Kawamura, K.; et al. PET quantification of tau pathology in human brain with ¹¹C-PBB3. *J. Nucl. Med.* **2015**, *56*, 1359–1365. [[CrossRef](#)] [[PubMed](#)]
166. Liu, F.-T.; Li, X.-Y.; Lu, J.-Y.; Wu, P.; Li, L.; Liang, X.-N.; Ju, Z.-Z.; Jiao, F.-Y.; Chen, M.-J.; Ge, J.-J.; et al. ¹⁸F-Florzolotau Tau Positron Emission Tomography Imaging in Patients with Multiple System Atrophy–Parkinsonian Subtype. *Mov. Disord.* **2022**, *37*, 1915–1923. [[CrossRef](#)]
167. Hashimoto, H.; Kawamura, K.; Igarashi, N.; Takei, M.; Fujishiro, T.; Aihara, Y.; Shiomi, S.; Muto, M.; Ito, T.; Furutsuka, K.; et al. Radiosynthesis, photoisomerization, biodistribution, and metabolite analysis of ¹¹C-PBB3 as a clinically useful PET probe for imaging of tau pathology. *J. Nucl. Med.* **2014**, *55*, 1532–1538. [[CrossRef](#)]
168. Weng, C.-C.; Hsiao, I.-T.; Yang, Q.-F.; Yao, C.-H.; Tai, C.-Y.; Wu, M.-F.; Yen, T.-C.; Jang, M.-K.; Lin, K.-J. Characterization of ¹⁸F-PM-PBB3 (¹⁸F-APN-1607) Uptake in the rTg4510 Mouse Model of Tauopathy. *Molecules* **2020**, *25*, 1750. [[CrossRef](#)]
169. Kawamura, K.; Hashimoto, H.; Furutsuka, K.; Ohkubo, T.; Fujishiro, T.; Togashi, T.; Arashi, D.; Sakai, T.; Muto, M.; Ogawa, M.; et al. Radiosynthesis and quality control testing of the tau imaging positron emission tomography tracer [¹⁸F]PM-PBB3 for clinical applications. *J. Label. Compd. Radiopharm.* **2021**, *64*, 109–119. [[CrossRef](#)]
170. Tagai, K.; Ono, M.; Kubota, M.; Kitamura, S.; Takahata, K.; Seki, C.; Takado, Y.; Shinotoh, H.; Sano, Y.; Yamamoto, Y.; et al. High-contrast in vivo imaging of tau pathologies in Alzheimer's and non-Alzheimer's disease tauopathies. *Neuron* **2021**, *109*, 42–58. [[CrossRef](#)]
171. Shimada, H.; Kitamura, S.; Ono, M.; Kimura, Y.; Ichise, M.; Takahata, K.; Moriguchi, S.; Kubota, M.; Ishii, T.; Takado, Y.; et al. [IC-P-198]: First-in-Human Pet Study with ¹⁸F-AM-PBB3 and ¹⁸F-PM-PBB3. *Alzheimer's Dement.* **2017**, *13*, P146.
172. Walji, A.M.; Hostetler, E.D.; Selnick, H.; Zeng, Z.; Miller, P.; Bennacef, I.; Salinas, C.; Connolly, B.; Gantert, L.; Holahan, M.; et al. Discovery of 6-(Fluoro-¹⁸F)-3-(1H-pyrrolo[2,3-c]pyridin-1-yl)isoquinolin-5-amine ([¹⁸F]-MK-6240): A Positron Emission Tomography (PET) Imaging Agent for Quantification of Neurofibrillary Tangles (NFTs). *J. Med. Chem.* **2016**, *59*, 4778–4789. [[CrossRef](#)] [[PubMed](#)]
173. Hostetler, E.D.; Walji, A.M.; Zeng, Z.; Miller, P.; Bennacef, I.; Salinas, C.; Connolly, B.; Gantert, L.; Haley, H.; Holahan, M.; et al. Preclinical Characterization of ¹⁸F-MK-6240, a Promising PET Tracer for In Vivo Quantification of Human Neurofibrillary Tangles. *J. Nucl. Med.* **2016**, *57*, 1599–1606. [[CrossRef](#)] [[PubMed](#)]
174. Malarte, M.L.; Nordberg, A.; Lemoine, L. Characterization of MK6240, a tau PET tracer, in autopsy brain tissue from Alzheimer's disease cases. *Eur. J. Nucl. Med. Mol. Imaging* **2021**, *48*, 1093–1102. [[CrossRef](#)] [[PubMed](#)]

175. Agüero, C.; Dhaynaut, M.; Normandin, M.D.; Amaral, A.C.; Guehl, N.J.; Neelamegam, R.; Marquie, M.; Johnson, K.A.; El Fakhri, G.; Frosch, M.P.; et al. Autoradiography validation of novel tau PET tracer [F-18]-MK-6240 on human postmortem brain tissue. *Acta Neuropathol. Commun.* **2019**, *7*, 37. [[CrossRef](#)]
176. Koole, M.; Lohith, T.G.; Valentine, J.L.; Bennacef, I.; Declercq, R.; Reynders, T.; Riffel, K.; Celen, S.; Serdons, K.; Bormans, G.; et al. Preclinical Safety Evaluation and Human Dosimetry of [¹⁸F]MK-6240, a Novel PET Tracer for Imaging Neurofibrillary Tangles. *Mol. Imaging Biol.* **2020**, *22*, 173–180. [[CrossRef](#)]
177. Betthausen, T.J.; Cody, K.A.; Zammit, M.D.; Murali, D.; Converse, A.K.; Barnhart, T.E.; Stone, C.K.; Rowley, H.A.; Johnson, S.C.; Christian, B.T. In Vivo Characterization and Quantification of Neurofibrillary Tau PET Radioligand ¹⁸F-MK-6240 in Humans from Alzheimer Disease Dementia to Young Controls. *J. Nucl. Med.* **2019**, *60*, 93–99. [[CrossRef](#)]
178. Lohith, T.G.; Bennacef, I.; Vandenberghe, R.; Vandembulcke, M.; Salinas, C.A.; Declercq, R.; Reynders, T.; Telan-Choing, N.F.; Riffel, K.; Celen, S.; et al. Brain Imaging of Alzheimer Dementia Patients and Elderly Controls with ¹⁸F-MK-6240, a PET Tracer Targeting Neurofibrillary Tangles. *J. Nucl. Med.* **2019**, *60*, 107–114. [[CrossRef](#)]
179. Salinas, C.; Lohith, T.G.; Purohit, A.; Struyk, A.; Sur, C.; Bennacef, I.; Beaver, J.; Martarello, L. Test-retest characteristic of [¹⁸F]MK-6240 quantitative outcomes in cognitively normal adults and subjects with Alzheimer’s disease. *J. Cereb. Blood Flow Metab.* **2020**, *40*, 2179–2187. [[CrossRef](#)]
180. Gogola, A.; Minhas, D.S.; Villemagne, V.L.; Cohen, A.D.; Mountz, J.M.; Pascoal, T.A.; Laymon, C.M.; Mason, N.S.; Ikonovic, M.D.; Mathis, C.A.; et al. Direct comparison of the tau PET tracers [¹⁸F]flortaucipir and [¹⁸F]MK-6240 in human subjects. *J. Nucl. Med.* **2021**, *63*, 108–116. [[CrossRef](#)]
181. Sanabria-Bohórquez, S.; Marik, J.; Ogasawara, A.; Tinianow, J.N.; Gill, H.S.; Barret, O.; Tamagnan, G.; Alagille, D.; Ayalon, G.; Manser, P.; et al. [¹⁸F]GTP1 (Genentech Tau Probe 1), a radioligand for detecting neurofibrillary tangle tau pathology in Alzheimer’s disease. *Eur. J. Nucl. Med. Mol. Imaging* **2019**, *46*, 2077–2089. [[CrossRef](#)]
182. Marik, J.T.J.; Ogasawara, A. [¹⁸F]GTP1—A tau specific tracer for imaging tau-pathology in AD. In Proceedings of the Human Amyloid Imaging Conference, Miami Beach, FL, USA, 13–15 January 2016.
183. Teng, E.; Ward, M.; Manser, P.T.; Sanabria-Bohórquez, S.; Ray, R.D.; Wildsmith, K.R.; Baker, S.; Kerchner, G.A.; Weimer, R.M. Cross-sectional associations between [¹⁸F]GTP1 tau PET and cognition in Alzheimer’s disease. *Neurobiol. Aging* **2019**, *81*, 138–145. [[CrossRef](#)] [[PubMed](#)]
184. Bohórquez, S.S.; Barret, O.; Tamagnan, G.; Alagille, D.; Marik, J.; Ayalon, G.; Bengtsson, T.; de Crespigny, A.; Jennings, D.; Seibyl, J.P.; et al. P4-351: Evaluation of TAU Burden in a Cross-Sectional Cohort of Alzheimer’s Disease Subjects Using [¹⁸F] GTP1 (Genetech tau probe 1). *Alzheimer’s Dement.* **2016**, *12*, P1172. [[CrossRef](#)]
185. Honer, M.; Gobbi, L.; Knust, H.; Kuwabara, H.; Muri, D.; Koerner, M.; Valentine, H.; Dannals, R.F.; Wong, D.F.; Borroni, E. Preclinical evaluation of ¹⁸F-RO6958948, ¹¹C-RO6931643, and ¹¹C-RO6924963 as novel PET radiotracers for imaging tau aggregates in Alzheimer disease. *J. Nucl. Med.* **2018**, *59*, 675–681. [[CrossRef](#)] [[PubMed](#)]
186. Kuwabara, H.; Comley, R.A.; Borroni, E.; Honer, M.; Kitzmiller, K.; Roberts, J.; Gapasin, L.; Mathur, A.; Klein, G.; Wong, D.F. Evaluation of ¹⁸F-RO-948 PET for quantitative assessment of tau accumulation in the human brain. *J. Nucl. Med.* **2018**, *59*, 1877–1884. [[CrossRef](#)]
187. Rombouts, F.J.; Andrés, J.I.; Ariza, M.; Alonso, J.M.; Austin, N.; Bottelbergs, A.; Chen, L.; Chupakhin, V.; Cleiren, E.; Fierens, K.; et al. Discovery of N-(Pyridin-4-yl)-1,5-naphthyridin-2-amines as Potential Tau Pathology PET Tracers for Alzheimer’s Disease. *J. Med. Chem.* **2017**, *60*, 1272–1291. [[CrossRef](#)]
188. Declercq, L.; Rombouts, F.; Koole, M.; Fierens, K.; Mariën, J.; Langlois, X.; Andrés, J.I.; Schmidt, M.; Macdonald, G.; Moechars, D.; et al. Preclinical Evaluation of ¹⁸F-JNJ64349311, a Novel PET Tracer for Tau Imaging. *J. Nucl. Med.* **2017**, *58*, 975–981. [[CrossRef](#)]
189. Rombouts, F.J.R.; Declercq, L.; Andrés, J.I.; Bottelbergs, A.; Chen, L.; Iturrino, L.; Leenaerts, J.E.; Mariën, J.; Song, F.; Wintmolders, C.; et al. Discovery of N-(4-[¹⁸F]Fluoro-5-methylpyridin-2-yl)isoquinolin-6-amine (JNJ-64326067), a New Promising Tau Positron Emission Tomography Imaging Tracer. *J. Med. Chem.* **2019**, *62*, 2974–2987. [[CrossRef](#)]
190. Baker, S.L.; Provost, K.; Thomas, W.P.; Whitman, A.J.; Janabi, M.; Schmidt, M.E.; Timmers, M.; Kolb, H.C.; Rabinovici, G.D.; Jagust, W.J. Evaluation of ¹⁸F-JNJ-067 as a tau tracer. *Alzheimer’s Dement.* **2020**, *16*, e040651. [[CrossRef](#)]
191. Kroth, H.; Oden, F.; Molette, J.; Schieferstein, H.; Capotosti, F.; Mueller, A.; Berndt, M.; Schmitt-Willich, H.; Darmency, V.; Gabellieri, E.; et al. Discovery and preclinical characterization of [¹⁸F]PI-2620, a next-generation tau PET tracer for the assessment of tau pathology in Alzheimer’s disease and other tauopathies. *Eur. J. Nucl. Med. Mol. Imaging* **2019**, *46*, 2178–2189. [[CrossRef](#)]
192. Mueller, A.; Kroth, H.; Berndt, M.; Capotosti, F.; Molette, J.; Schieferstein, H.; Oden, F.; Juergens, T.; Darmency, V.; Schmitt-Willich, H.; et al. Characterization of the novel PET Tracer PI-2620 for the assessment of Tau pathology in Alzheimer’s disease and other tauopathies. *J. Nucl. Med.* **2017**, *58*, 847.
193. Bullich, S.; Barret, O.; Constantinescu, C.; Sandiego, C.; Mueller, A.; Berndt, M.; Papin, C.; Perrotin, A.; Koglin, N.; Kroth, H.; et al. Evaluation of Dosimetry, Quantitative Methods, and Test–Retest Variability of ¹⁸F-PI-2620 PET for the Assessment of Tau Deposits in the Human Brain. *J. Nucl. Med.* **2020**, *61*, 920–927. [[CrossRef](#)] [[PubMed](#)]
194. Brendel, M.; Barthel, H.; van Eimeren, T.; Marek, K.; Beyer, L.; Song, M.; Sauerbeck, J.; Barbe, M.; Schroeter, M.; Russell, D.; et al. ¹⁸F-PI2620 Tau-PET in Progressive Supranuclear Palsy-A multi-center evaluation. *J. Nucl. Med.* **2019**, *60* (Suppl. S1), 54.

195. Stephens, A.; Seibyl, J.; Mueller, A.; Barret, O.; Berndt, M.; Madonia, J.; Kroth, H.; Bullich, S.; Pfeifer, A.; Muhs, A.; et al. IC-P-220: Clinical Update: ^{18}F -PI-2620, a Next Generation Tau PET Agent Evaluated in Subjects with Alzheimer's Disease and Progressive Supranuclear Palsy. *Alzheimer's Dement.* **2018**, *14*, P179. [[CrossRef](#)]
196. Villemagne, V.; Dore, V.; Mulligan, R.; Lamb, F.; Bourgeat, P.; Salvado, O.; Masters, C.; Rowe, C. Evaluation of ^{18}F -PI-2620, a second-generation selective tau tracer for the assessment of Alzheimer's and non-Alzheimer's tauopathies. *J. Nucl. Med.* **2018**, *59* (Suppl. S1), 410.
197. Barret, O.; Seibyl, J.; Stephens, A.; Madonia, J.; Alagille, D.; Mueller, A.; Bendt, M.; Kroth, H.; Muhs, A.; Pfeifer, A.; et al. Initial clinical PET studies with the novel tau agent ^{18}F PI-2620 in Alzheimer's disease and controls. *J. Nucl. Med.* **2017**, *58* (Suppl. S1), 630.
198. Brendel, M.; Palleis, C.; Prix, C.; Finze, A.; Boetzel, K.; Danek, A.; Höllerhage, M.; Beyer, L.; Sauerbeck, J.; Rauchmann, B.; et al. ^{18}F -PI-2620 tau-PET in corticobasal syndrome (ActiGliA cohort). *Alzheimer's Dement.* **2020**, *16*, e041469. [[CrossRef](#)]
199. Chotipanich, C.; Nivorn, M.; Kunawudhi, A.; Promteangtrong, C.; Boonkawin, N.; Jantarato, A. Evaluation of Imaging Windows for Tau PET Imaging Using ^{18}F -PI2620 in Cognitively Normal Individuals, Mild Cognitive Impairment, and Alzheimer's Disease Patients. *Mol. Imaging* **2020**, *19*, 1536012120947582. [[CrossRef](#)]
200. Mormino, E.C.; Toueg, T.N.; Azevedo, C.; Castillo, J.B.; Guo, W.; Nadiadwala, A.; Corso, N.K.; Hall, J.N.; Fan, A.; Trelle, A.N.; et al. Tau PET imaging with ^{18}F -PI-2620 in aging and neurodegenerative diseases. *Eur. J. Nucl. Med. Mol. Imaging* **2020**, *48*, 2233–2244. [[CrossRef](#)] [[PubMed](#)]
201. Kaide, S.; Ono, M.; Watanabe, H.; Kitada, A.; Yoshimura, M.; Shimizu, Y.; Saji, H. Structure–Activity Relationships of Radioiodinated Benzoimidazopyridine Derivatives for Detection of Tau Pathology. *ACS Med. Chem. Lett.* **2018**, *9*, 478–483. [[CrossRef](#)] [[PubMed](#)]
202. Watanabe, H.; Tatsumi, H.; Kaide, S.; Shimizu, Y.; Iikuni, S.; Ono, M. Structure-Activity Relationships of Radioiodinated 6,5,6-Tricyclic Compounds for the Development of Tau Imaging Probes. *ACS Med. Chem. Lett.* **2020**, *11*, 120–126. [[CrossRef](#)]
203. Watanabe, H.; Tarumizu, Y.; Kaide, S.; Shimizu, Y.; Iikuni, S.; Nakamoto, Y.; Ono, M. Structure–Activity and Brain Kinetics Relationships of ^{18}F -Labeled Benzimidazopyridine Derivatives as Tau PET Tracers. *ACS Med. Chem. Lett.* **2021**, *12*, 262–266. [[CrossRef](#)] [[PubMed](#)]
204. Carter, S.F.; Schöll, M.; Almkvist, O.; Wall, A.; Engler, H.; Långström, B.; Nordberg, A. Evidence for astrocytosis in prodromal Alzheimer disease provided by ^{11}C -deuterium-L-deprenyl: A multitracer PET paradigm combining ^{11}C -Pittsburgh compound B and ^{18}F -FDG. *J. Nucl. Med.* **2012**, *53*, 37–46. [[CrossRef](#)] [[PubMed](#)]
205. Ono, M.; Watanabe, H.; Kitada, A.; Matsumura, K.; Ihara, M.; Saji, H. Highly selective tau-SPECT imaging probes for detection of neurofibrillary tangles in Alzheimer's disease. *Sci. Rep.* **2016**, *6*, srep34197. [[CrossRef](#)] [[PubMed](#)]
206. Kaide, S.; Watanabe, H.; Shimizu, Y.; Tatsumi, H.; Iikuni, S.; Nakamoto, Y.; Togashi, K.; Ihara, M.; Saji, H.; Ono, M. ^{18}F -labeled benzimidazopyridine derivatives for PET imaging of tau pathology in Alzheimer's disease. *Bioorganic Med. Chem.* **2019**, *27*, 3587–3594. [[CrossRef](#)]
207. Krause-Sorio, B.; Siddarth, P.; Laird, K.T.; Ercoli, L.; Narr, K.; Barrio, J.R.; Small, G.; Lavretsky, H. [^{18}F]FDDNP PET binding predicts change in executive function in a pilot clinical trial of geriatric depression. *Int. Psychogeriatr.* **2021**, *33*, 149–156. [[CrossRef](#)]
208. Wright, J.P.; Goodman, J.R.; Lin, Y.G.; Lieberman, B.P.; Clemens, J.; Gomez, L.F.; Liang, Q.; Hoye, A.T.; Pontecorvo, M.J.; Conway, K.A. Monoamine oxidase binding not expected to significantly affect [^{18}F]flortaucipir PET interpretation. *Eur. J. Nucl. Med. Mol. Imaging* **2022**, *49*, 3797–3808. [[CrossRef](#)]
209. Nakamura, S.; Kawamata, T.; Akiguchi, I.; Kameyama, M.; Nakamura, N.; Kimura, H. Expression of monoamine oxidase B activity in astrocytes of senile plaques. *Acta Neuropathol.* **1990**, *80*, 419–425. [[CrossRef](#)]
210. Ng, K.P.; Pascoal, T.A.; Mathotaarachchi, S.; Therriault, J.; Kang, M.S.; Shin, M.; Guiot, M.C.; Guo, Q.; Harada, R.; Comley, R.A.; et al. Monoamine oxidase B inhibitor, selegiline, reduces ^{18}F -THK5351 uptake in the human brain. *Alzheimer's Res. Ther.* **2017**, *9*, 25. [[CrossRef](#)] [[PubMed](#)]

Disclaimer/Publisher's Note: The statements, opinions and data contained in all publications are solely those of the individual author(s) and contributor(s) and not of MDPI and/or the editor(s). MDPI and/or the editor(s) disclaim responsibility for any injury to people or property resulting from any ideas, methods, instructions or products referred to in the content.